Plasma Vertical Position Control in the COMPASS-D Tokamak

Parag Vyas

Department of Engineering Science
University of Oxford
Oxford OX1 3PJ

This thesis is submitted to the University of Oxford in partial fulfilment of the requirements for the degree of Doctor of Philosophy.

Parag Vyas,
The Queen's College, Oxford,
Trinity Term 1996

Abstract

The plasma vertical position system on the COMPASS–D tokamak is studied in this thesis. An analogue P+D controller is used to regulate the plasma vertical position which is open loop unstable. Measurements from inside the vessel are used for the derivative component of the control signal and external measurements for the proportional component.

Two main sources of disturbances are observed on COMPASS–D. One source is 600Hz noise from thyristor power supplies which cause large oscillations at the control amplifier output. Another source is impulse–like disturbances due to ELMs (Edge Localized Modes) and this can occasionally lead to loss of control when the control amplifier saturates.

Models of the plasma open loop dynamics were obtained using the process of system identification. Experimental data is used to fit the coefficients of a mathematical model. The frequency response of the model is strongly dependent on the shape of the plasma. The effect of shielding by the vessel wall on external measurements when compared with internal measurements is also observed. The models were used to predict values of gain margins and phase crossover frequencies which were found to be in good agreement with measured values.

The harsh reactor conditions on the proposed ITER tokamak preclude the use of internal measurements. On COMPASS–D the stability margins of the loop decrease when using only external flux loops. High order controllers were designed to stabilize the system using only external measurements and to reduce the effect of 600Hz noise on the control amplifier voltage. The controllers were tested on COMPASS–D and demonstrated the improved performance of high order controllers over the simple P+D controller.

ELMs cause impulse–like disturbances on the plasma position. The optimal controller minimizing the peak of the impulse response can be calculated analytically for COMPASS–D. A multiobjective controller which combines a small peak impulse response with robust stability and noise attenuation can be obtained using a numerical search.

Acknowledgements

I have benefited from the help of many people whilst working on this thesis. To those who have assisted me it is a pleasure to acknowledge your help. If I have forgotten to mention you please do not be offended.

The work at Culham was coordinated by Dr William Morris and I thank him for his support and guidance. I also wish to thank my academic supervisors at Oxford; Dr Denis Mustafa for initiating the project and for his advice, and Dr Basil Kouvaritakis for his invaluable help and assistance during the latter part of this work.

Recognition is due to the control group at Oxford. Thanks are due in particular to Jesse Gossner for guidance on the use of his CaSC toolbox, Gwo–Jeng Ju for his help and encouragement, and Luigi Scibile for his help in the field of tokamak position control.

Tokamak physics is a difficult subject and many people have helped my limited understanding. I have received much guidance on my work from Mr Tom Todd and Dr Mike Walsh. Assistance on magnetic diagnostics has been received from Dr Martin Valovič and help in using the PACE computer program from Dr Peter Knight, and the DFIT program from Dr Lynton Appel.

Computer support has been prompt and effective due to the efforts of Miss Sue Manhood and Mr Nick Benterman. To them and the rest of the COMPASS–D team please accept my appreciation.

Working at Culham was a pleasure, due in part to many a lengthy discussion over coffee or lunch. Thanks to Ash, Celso, George, Julio, Neil, Paul, Paul, Rob and many others.

This project was financially supported by the UK Engineering and Physical Sciences Research Council, the UK Department of Trade and Industry, and EURATOM and this is gratefully acknowledged.

Not least a thank you is due to my parents and Seema and Sheetal for their patience and understanding.

to my mother and father

for their care and support

Contents

1 Introduction 14

1.1 Objectives 14
1.2 Thesis outline 15
1.3 Review of earlier work 18
1.4 Summary 20

2 Position and Shape Control 22

2.1 Overview 22
2.2 COMPASS-D 28
2.3 Plasma shape and position control 29
2.4 Plasma vertical position 33
2.5 COMPASS-D vertical position control loop 37
2.6 Position sensors 38
2.7 Actuator 41
2.8 Controller 44
2.9 Plasma operation 46
2.10 Discussion 50

3 System Identification 53

3.1 Introduction 53
3.2 System identification method 58
3.3 Model structure 61
3.4 Signal analysis 67
3.5 Prefiltering of data 71
3.6 Model order 75
3.7 Experimental results 78
3.8 Summary 83

4 Linear Control 85

4.1 P+D performance 85
4.2 Controller objectives 88
4.3 H_∞ problem structure 89
4.4 H_∞ results 100
4.5 SGPC 104
4.6 Conclusions 117

5 Peak Impulse Response 119

5.1 Introduction 119
5.2 Optimal solution 119
5.3 Multiobjective controller 129
5.4 Discussion 134

6 Conclusions 135

7 References 138

Figures

Figure 2.1 Toroidal and poloidal magnetic confinement fields. (Diagram provided by Public Relations Dept., UKAEA Fusion.) 23

Figure 2.2 Plasma shapes: a) circle, b) up–down symmetric D, c) SND, d) SNT 25

Figure 2.3 Destabilizing forces acting on plasma. 27

Figure 2.4 COMPASS–D. (Reproduced from [Booth86].) 29

Figure 2.5 COMPASS–D poloidal field system. *S* – shaping coils for typical SND plasma, B_z – vertical field coils, B_R – radial field. 31

Figure 2.6 Shaping field from shaping ('*S*') coils for positive plasma current (i.e. plasma current flows into page). 32

Figure 2.7 Field from B_{zf} coils. 32

Figure 2.8 Magnetic field from B_R coils. 33

Figure 2.9 B_R' field plot from poloidal field coils for typical SND plasma (Shot no. 17190, I_p=171kA). 34

Figure 2.10 Equilibrium solutions of current density profile for SND plasma, I_p=171kA. 36

Figure 2.11 Vertical position control loop. 38

Figure 2.12 Step responses. 40

Figure 2.13 Position from LCFS reconstruction and calibrated FL and IPR signals. 40

Figure 2.14 Measured and predicted (R_c=11.45mΩ and L_c=94.79μH) frequency response of control coil. 43

Figure 2.15 Block diagram of vertical control loop with P+D controller. 46

Figure 2.16 Vertical position control signals for typical shot with P+D controller. 48

Figure 2.17 Detail of typical shot showing dominant 600Hz signal. 48

Figure 2.18 600Hz component and harmonics in amplifier voltage. 51

Figure 2.19 Amplitude spectra of IPR and FL velocity signals with low frequency amplitude normalized. 51

Figure 2.20 L–mode, ELM–free H–mode and ELMy H–mode operation. 52

Figure 2.21 Large separated ELMs. 52

Figure 3.1 Random binary sequence reference position signal and amplifier current and FL position response. 55

Figure 3.2 Bode plot of plasma response. 57

Figure 3.3 Nyquist plot with 95% confidence bounds. 66

Figure 3.4 FIR model coefficients. 66

Figure 3.5 Size of 95% confidence ellipse against frequency. 67

Figure 3.6 Frequency spectra of reference and input/output data shot no. 14703. 68

Figure 3.7 Detail of spectra for shot no. 14703. 70

Figure 3.8 Effect of increasing no. of samples on estimates (a_1, a_2 and a_3) and ±3 standard deviations. 71

Figure 3.9 Autocorrelation of residuals for FL model. 73

Figure 3.10 Autocorrelation of residuals for IPR model. 73

Figure 3.11 Effect of high pass prefilter on model frequency response. 75

Figure 3.12 Residual cost for different model orders. 76

Figure 3.13 Effect of model order on Bode plots. 77

Figure 3.14 Comparison of FL and IPR frequency response. The IPR gain is normalized to the FL gain to allow comparison of the model roll off. 77

Figure 3.15 Open loop instability growth rate for SND and SNT plasma. 79

Figure 3.16 Bode plot of SND configuration plasma at different I_s/I_p. 79

Figure 3.17 Effect of toroidal field on frequency response. 81

Figure 3.18 ELMy to ELM free H–mode plasma. 82

Figure 3.19 Frequency responses of ELMy and ELM free periods. 82

Figure 4.1 Nyquist diagram of FL/IPR loop ($L_{FL/IPR}$) and FL only loop (L_{FL}). 86

Figure 4.2 Bode plot of P+D controller and 600Hz notch filter. 86

Figure 4.3 Nyquist plot of P+D FL only loop at different I_s/I_p. 87

Figure 4.4 $\mathbf{H}_\infty$ Block diagram. 91

Figure 4.5 Weights for $\mathbf{H}_\infty$ controller. 91

Figure 4.6 Bode plot of $\mathbf{H}_\infty$ and P+D controller. 94

Figure 4.7 Weighted closed loop transfer functions. 94

Figure 4.8 Bode plot of loop gain with $\mathbf{H}_\infty$ controller ($L_{H\infty}$). Loop gains determined from gain margin measurements are marked with crosses. 97

Figure 4.9 Nyquist plot of $L_{H\infty}$ using ARX and FIR models with 95% confidence bounds. 97

Figure 4.10 Shot using $\mathbf{H}_\infty$ controller ($K_{H\infty}$). 98

Figure 4.11 Comparison of amplifier frequency spectra. 98

Figure 4.12 Effect of decreasing loop gain. 99

Figure 4.13 Effect of increasing loop gain. 99

Figure 4.14 Vertical position signals for shot with poor stability margin. 101

Figure 4.15 Nyquist plot of shot with poor stability margin. The nominal loop gain is plotted along with the effect of including a 50μs pure time delay. 102

Figure 4.16 Bode plot of closed loop gain showing resonant peaks. 102

Figure 4.17 Drift in FL position as I_s/I_p increases. 104

Figure 4.18 Scheme for designing SGPC controller. 107

Figure 4.19 Nyquist plot of loop gain with SGPC controller with *Q* optimization (K_{SGPC}). For comparison the loop gain with the **H**∞ controller ($K_{H\infty}$) and the SGPC controller without *Q* optimization. 115

Figure 4.20 Result of using CaSC controller (K_{SGPC}). 115

Figure 5.1 Closed loop response of optimal and suboptimal peak response controllers for COMPASS–D type plants. 121

Figure 5.2 Suboptimal peak against order. 127

Figure 5.3 Optimal peak response. 127

Figure 5.4 Optimal peak impulse response with $\mathbf{H}_\infty$ constraints. 133

Figure 5.5 Impulse response of $\mathbf{H}_\infty$ controller (γ=0.12) and *Q* optimized controller (n_Q=20). 133

Tables

Table 2.1 Comparison of COMPASS–D, JET and ITER. 28

Table 3.1 Discrete time model coefficients and estimated variances for an SND plasma, I_p=143kA, B_T=1.2T, κ=1.6 and FL position output signal (Shot no. 18001). 56

Table 3.2 List of shots with RBS excitation. 80

Table 4.1 Coefficients of $\mathbf{H}_\infty$ controller transfer function. 96

Table 4.2 Coefficients of CaSC controller transfer function. 117

Abbreviations and Acronyms

ARX: AutoRegressive with eXternal input (Section 3.3)

COMPASS–D: COMPact ASSembly D–shaped vacuum vessel (Section 2.2)

CaSC: Cautious Stable Predictive Control (Section 4.5)

DFIT: computer program for plasma last closed flux surface reconstruction (Section 2.6)

DFT: Discrete Fourier Transform (Section 2.7)

DSP: Digital Signal Processor (Section 2.8)

ELM: Edge Localized Mode (Section 2.9)

ETFE: Empirical Transfer Function Estimate (Section 2.7)

FIR: Finite Impulse Response (Section 3.3)

FL: Flux Loop (Section 2.6)

GPC: Generalized Predictive Control (Section 4.5)

H–mode: plasma regime with High energy confinement time (Section 2.9)

IPR: Internal Partial Rogowskii (Section 2.6)

ITER: International Thermonuclear Experimental Reactor (Section 2.1)

JET: Joint European Torus (Section 2.1)

L–mode: plasma regime with Low energy confinement time (Section 2.9)

LP: Linear Programming (Section 5.2)

MBPC: Model Based Predictive Control (Section 4.5)

MHD: Magnetohydrodynamics (Section 2.9)

PACE: computer program for simulating plasma position (Section 3.7)

PEM: Predictor-Error Methods (Section 3.2)

SGPC: Stable Generalized Predictive Control (Section 4.5)

SND: Single–Null Diverted plasma shape (Section 2.1)

SNT: Single–Null diverted high Triangularity plasma shape (Section 2.1)

1 Introduction

Tokamaks are plasma confinement devices with the potential to form the basis of nuclear fusion power plants. A tokamak fusion reactor would require the plasma to be kept at a temperature of more than 10^8 °C and for a current of order 10MA to flow through the plasma. Plasma instabilities are often observed, including instability of the plasma vertical position. The consequences of loss of control in a fusion reactor would be severe, leading to forces possibly of the order of meganewtons exerted on the machine structure, and high temperature and current loads.

There are a large number of tokamak experiments in many different countries. At present the largest is the JET machine at Culham, UK. A new much larger tokamak, ITER, is at the design stage and should establish the physics necessary for a tokamak based power plant. The COMPASS–D tokamak is also at Culham, and one of the main aims of the machine is the study of instabilities which occur in JET and ITER type devices. This thesis examines the control of the plasma vertical position in the COMPASS–D tokamak.

1.1 Objectives

The thesis examines the operation of the plasma vertical position control loop on the COMPASS-D tokamak. The aim is to improve the performance of the loop and to assess implications for larger devices such as ITER and JET from experimental evidence. The thesis objectives are therefore firstly to characterize the noise and disturbances observed in operation on COMPASS–D. Secondly to develop open loop models of the plasma vertical position system and compare predicted open loop performance with experimental results. The final aim is to design advanced controllers to improve the performance of the system and to demonstrate their use on COMPASS–D.

1.2 Thesis outline

The objectives of this project are described in this chapter, along with a review of previous work relevant to this thesis. An introduction to the contents of the rest of this thesis is provided in this section.

Chapter 2 contains a brief overview of tokamak principles and the physics involved in the plasma vertical position response. Many tokamaks operate with circular shaped plasmas which are vertically open loop stable. Vertically elongated plasmas can improve the efficiency of tokamaks but also cause the plasma vertical position to become unstable. Increasing the plasma elongation (ratio of plasma height to width) increases the instability growth rate and closed loop stability becomes more difficult to achieve. Loss of control in a large tokamak results in large forces and high heat and current loads on the machine structure. It is therefore important to study the control of vertical position in tokamaks in order to minimize the possibility of loss of control.

The COMPASS–D tokamak is also briefly described in Chapter 2. One of the main objectives of the COMPASS–D programme at Culham is the study of tokamak plasma instabilities and development of techniques to prevent loss of control in larger devices. COMPASS–D has the same geometry and shape as JET and ITER except it is much smaller. Its small size makes it suitable for study and demonstration of experimental ideas because of the ease and flexibility of operations and the significantly reduced consequences of loss of control.

The vertical position control loop on COMPASS–D is described in detail. It is based on an analogue P+D control scheme. Measurements of plasma velocity from magnetic pickup coils inside the vessel are used for the derivative part of the control signal. The proportional component is obtained by integrating the velocity signals from coils placed outside the vessel. The resulting P+D control system can be tuned to provide an adequate degree of stability.

In all experiments the control signal is dominated by a 600Hz component (and higher harmonics) due to interference from 12 phase thyristor rectifiers used in radial position, shape, and plasma current control loops. It is also noted that the internal velocity measurements have a much larger high frequency (above 3kHz) noise component than the external measurements. Other disturbances are frequently

observed. In particular step changes in plasma position and control currents arise when the plasma changes from a low energy confinement time mode to a high confinement time mode. Impulse–like disturbances are also observed and are caused by Edge Localized Modes (ELMs). They can cause large perturbations in the plasma position and control signals. High frequency ELMs tend to have small amplitudes. However low frequency ELMs tend to have large amplitudes which can cause the control amplifiers to saturate, occasionally leading to loss of control of the plasma vertical position.

Mathematical models of the open loop plasma vertical position response to currents in control coils are derived in Chapter 3. System identification is used to obtain a model of the plasma response directly from experimental data. This is done by perturbing the plasma vertical position using a random binary sequence reference signal and then fitting the parameters of a mathematical model to the resulting experimental data. The input signal is the current in the position control coil and the output signal is either a measurement internal to the vessel wall or an external measurement. The experiments were conducted in closed loop but the identified model is of the open loop vertical position system. A simple model structure is chosen with a small number of parameters which are calculated using a least squares fit.

The models are of the form of transfer functions and contain a single unstable pole. The instability growth rate increases if the shaping field is increased. This is consistent with physical models. The bandwidth of the frequency response increases and the DC gain decreases with increasing shape. The phase lead of the model also decreases with shape. The effect of the shielding from the vessel wall is observed when comparing models from external and internal coils. The amplitude response of the external model has a faster roll–off and there is less phase lead than in the internal coil model.

Chapter 4 examines the performance of the P+D control system and more complicated controllers. The use of internal measurements in the COMPASS–D P+D control loop results in a large stability margin, i.e. relatively large changes in the frequency response can occur without the system becoming unstable. However only external measurements will be available on ITER because of the harsh reactor conditions. The vessel wall shielding will reduce the stability margins and limit the operating regimes

of the machine. The 600Hz noise on COMPASS–D could be reduced by introducing a notch filter into the plant, but this would lead to more phase lag below 600Hz and would reduce the stability margins.

High order controllers designed using modern control theory are developed in Chapter 4 and were tested on COMPASS–D. The controllers were implemented on a Digital Signal Processor. Two types of controller are developed, one designed in the continuous time domain using $\mathbf{H}_\infty$ control theory, and another designed in discrete time using the SGPC (Stable Generalized Predictive Control) technique. The $\mathbf{H}_\infty$ controller is designed by specifying maximum bounds on the maximum magnitudes of various closed loop frequency responses, and the optimal controller maximizing a measure of stability margin is calculated. The bounds are used to constrain the closed loop gain at 600Hz to attenuate the 600Hz noise. Another bound is used to ensure that the steady state error between reference position signal and measured closed loop response is small.

A second SGPC controller is designed in two stages by separating the performance and the robust stability criteria. Initially a controller minimizing a time domain cost function is calculated. The cost is the weighted sum of the squares of the closed loop position error and control signal changes to a step input over a finite receding horizon. The robust stability margin is defined in the frequency domain in a manner similar to that used in the $\mathbf{H}_\infty$ controller. The controller is structured in a way such that changing the robust stability margin does not affect the performance cost. The aim of the second stage is to maximize the robust stability margin of the system. Note that for this controller a 600Hz notch filter is introduced into the controller and a large 600Hz penalty is used in the stability margin constraint.

Experimental results show that both high order controllers stabilize the plasma with only external measurements and reduce the effects of 600Hz noise on the control signal. Neither of these attributes are possible with a simple P+D controller. Stability margins are assessed experimentally by deliberately changing the loop gain until loss of control occurs. Predictions of closed loop stability margins and experimentally determined values are found to be in good agreement.

Large ELMs causing impulse–like responses can lead to loss of control on COMPASS–D. Controllers designed to minimize the peak response to impulses are

analyzed in Chapter 5. The first part of the chapter investigates the use of methods aimed at minimizing the peak closed loop response of an arbitrary plant to an arbitrary input. The optimal controller is obtained by solving a linear programming (LP) problem with an infinite number of constraints. For impulse inputs and the COMPASS–D plant the LP problem can be reduced to an analytical solution. The peak of the optimal closed loop response is largely dependent on the instability growth rate. Plants with larger growth rates have a larger optimal peak response. The optimal controller is of infinite order, but suboptimal, finite order controllers can be calculated. Higher order controllers have a smaller peak response. The resulting optimal or suboptimal controllers exhibit poor behaviour in terms of stability margins and noise amplification. A controller designed to address the stability and noise problem as well as minimizing the peak impulse response is obtained using numerical convex optimization techniques. The problem combines constraints used in the design of the $\mathbf{H}_\infty$ controller with the objective of minimizing the peak of the impulse response. Allowing for higher order controllers improves the peak impulse response performance. The results are useful in finding the limits of performance. However the controllers are of high order and are difficult to calculate and so these were considered impractical for use on COMPASS–D.

1.3 Review of earlier work

Early tokamaks used a copper shell for passive damping of the plasma radial and vertical position. Changes in plasma position induce eddy currents in the shell which act to oppose the motion. This scheme is effective if the discharge time is shorter than the eddy current diffusion time. The TO–1 tokamak used control coils in series with negative impedance circuits instead of a copper liner [Artemenkov72]. The results showed that the plasma radial displacement in the presence of disturbances is reduced. Reducing the net resistance of the coil and circuit lengthens the time for which the plasma position can be maintained but it cannot be held indefinitely. Experiments on the Cleo–Tokamak [Hugill74] used separate position sensors and actuators in independent radial and vertical position control loops. A bandwidth limited proportional controller was able to reduce plasma displacements and also stabilize an open loop vertically unstable plasma.

System identification was used to model the plasma radial position response in the HT–1 tokamak [Yoshioka82]. The model was used to calculate the loop frequency response and to tune the gains of a P+I radial position controller in order to improve a stability margin.

The effect of changing the gain of a proportional controller on a vertically unstable plasma in TNT–A was studied and compared with theoretical predictions [Nagayama84]. The range of stabilizing gains for different shaping fields and the closed loop response were in good agreement with theoretical models which included the effect of toroidal gaps in the vessel structure. A similar study was conducted on the JFT–2M tokamak with a P+D controller [Mori87].

A detailed study of vertical position P+D control is presented in [Lazarus90]. A low order linear model was developed which predicts a strong correlation between the instability growth rate and the shaping field. The effect of the position of actuator coils and the relationship between closed loop stability and performance and the proportional and derivative gains were also examined. Experimental results from the DIII–D tokamak and comparison with the model is presented in [Lister90]. A closed loop model was obtained directly from experimental data using system identification. The effect of changing the controller gains, the shaping fields and the effect of different actuator coils was in broad agreement with the model.

The effect of placing radial and vertical position sensor coils inside and outside the tokamak vessel is studied in [Wootton90]. A model and analytical expressions for step response overshoot and steady state errors were derived. The performance of the system is improved if the sensor coils are placed inside the vessel.

Attempts have been made to assess the performance of more complex controllers using simulations. A study of linear quadratic (LQ) optimal control of the plasma vertical position is presented in [Moriyama85]. It is suggested that extra phase lead in the control system can improve the performance of the loop. The effect of pure time delays in power supplies was also studied and shown to adversely effect performance. Many studies have analyzed multivariable LQ control for other plasma parameters such as the radial position, plasma current and density [Gran79], [Ogata79] and [Kessel90].

Robust stability has been addressed with the design of $\mathbf{H}_\infty$ controllers for vertical position control in [Al–Husari91] and [Portone94]. Model reduction of high order models was used before designing optimal controllers and testing with simulations. Techniques for identifying plasma models from input/output data which provide deterministic uncertainty bounds were applied to tokamak simulations in [Rubin93].

Simulations using self–tuning control to stabilize the vertical position in a time varying plasma model were examined in [Zheng93]. The plasma model parameters were identified at every sample interval using the recursive least squares (RLS) algorithm. Pole placement and generalized predictive control (GPC) synthesis algorithms were tested in simulations with step responses. The autotuning and adaptive tuning properties of both controllers were demonstrated.

Much of the design of high order controllers has been based on complicated physical models. The models are useful but it is not clear how accurately the models reflect actual tokamak plasma behaviour. Most of the work has addressed the issue of stability. Less work is available examining the consequences of noise and disturbances observed in tokamaks. The high order controllers are tested using computer simulations, often with ideal feedback measurements which are unaffected by noise. The previous theoretical work identifies the benefits available from high order controllers but highlights the need for experimental tests and analysis of vertical position control. In particular there is a need for models based on experimental behaviour and a need for characterizing important sources of noise and disturbances. This would allow controller objectives to be identified which more usefully address tokamak position control issues. There is also a need to test any complicated control system to ensure that theoretical advantages offered by complicated controllers occur in practice.

1.4 Summary

Vertically elongated plasma are often used in tokamaks because they offer confinement efficiency advantages. The disadvantage is that such plasmas are vertically unstable and that the consequences of disruptions in JET and ITER scale machines are serious. Vertical position control is suitable for study on COMPASS–D because of its advantages of small scale and similar geometry to larger machines.

Previous work on tokamak plasma vertical position control has highlighted the need for experimental analysis and modelling of the system and experimental tests of high order controllers. The aims of this thesis is to model and assess the vertical position control system on COMPASS–D. This involves deriving models which reflect experimental behaviour of the vertical position system and characterizing noise and disturbances. Appropriate controller objectives are also formulated and suitable controller designs are tested in experimental conditions on COMPASS–D.

2 Position and Shape Control

This chapter provides a description of the poloidal field system for position and shape control on COMPASS–D. The plasma vertical position is unstable and a simple model of the response is examined. The details of the vertical position control loop are provided, and experimental results of typical operation and disturbances are presented.

2.1 Overview

Tokamaks are machines which confine a plasma inside a toroidal vessel using magnetic fields. These machines have been developed with the aim of forming devices capable of sustained thermonuclear fusion and generating electricity. Fusion power plants offer the prospect of a substantial and practically inexhaustible supply of energy with acceptable environmental, health and safety risks.

The most likely fuel for a fusion power plant is a mixture of deuterium and tritium (isotopes of hydrogen). For fusion to occur the plasma must be heated to an ion temperature (T_i) of over 10keV (equivalent to 10^8 °C) at high density (n_i). The energy confinement time (τ_E) is the time constant at which energy stored in the plasma would decay without heating. It is defined as the ratio of stored energy to power. The value of the product $n_i\tau_E$ required for a reactor is $n_i\tau_E$>1.5 to $3\times10^{20}m^{-3}s$ [Wesson87, Section 1.1].

The high temperature of the plasma means that it cannot be confined by a material wall. Instead the tokamak uses magnetic fields to confine the plasma inside a toroidal vessel. Tokamaks have proved to be the most successful devices in confining plasmas at parameters near that required for fusion.

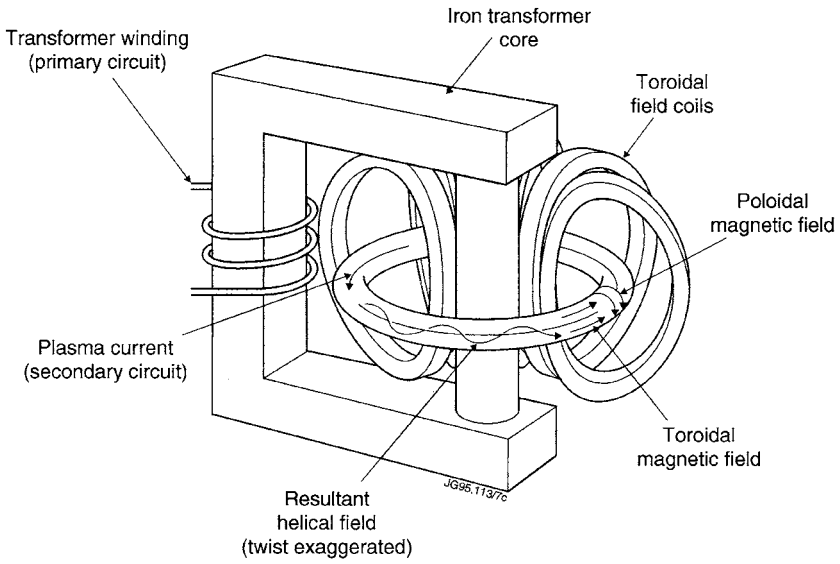


Figure 2.1 Toroidal and poloidal magnetic confinement fields. (Diagram provided by Public Relations Dept., UKAEA Fusion.)

The first tokamaks were built in Russia in the mid-50's and confined plasmas with the fusion triple product ($n_i\tau_E T_i$) of at least six orders of magnitude less than that required for a reactor. At present the largest tokamak in the world is JET (Joint European Torus) located at Culham. It has achieved conditions with the fusion triple product close to that required for sustained fusion reactions. A design for a new tokamak, ITER (International Thermonuclear Experimental Reactor) is being jointly developed by the EU, USA, Japan and Russia. It is intended to establish the physics necessary to design a tokamak based Demonstration Power-Plant (DEMO). If ITER is built it could be operating from about 2008 to 2020. The COMPASS–D (COMPact ASSembly, D–shaped vacuum vessel) tokamak is a small machine located at Culham. One of its aims is the study of instabilities which occur in JET and ITER type devices. Details of its construction are provided in [Hayward89].

Figure 2.1 illustrates the principle of operation of a tokamak. The major component of the confining magnetic field is toroidal and this is provided by the current in poloidal

coils surrounding the vessel (marked ‘Toroidal field coils’). A poloidal field component is also required to balance the plasma pressure by magnetic forces. The poloidal field is generated by a current flowing through the plasma which is induced by transformer action. The combination of poloidal and toroidal field components generates a resultant helical magnetic field. The surfaces covered by the helical field lines are known as magnetic flux surfaces. The poloidal magnetic flux linked by a toroidal contour on a flux surface is constant irrespective of the path taken by the contour. Similarly the toroidal magnetic flux through a poloidal contour on a flux surface is also constant.

Additional contributions to the poloidal field are generated by toroidal coils which are used to control the plasma position and shape (not shown in Fig. 2.1). Shown in Fig. 2.2 are the flux surfaces obtained for four different plasma shapes on COMPASS–D. Different shaping fields were used to generate the different shapes. A useful parameter characterizing the shape of a plasma is the elongation (κ) which is the ratio of the plasma half-height (b) to the plasma half-width (a). The triangularity (δ) is a measure of how much the plasma resembles a ‘D–shape’. The plasma position is usually specified by the location of the current centroid with z_p the position above the midplane, and R_p the radial position from the centre line of the tokamak. The circular plasma (Fig. 2.2a) is the simplest shape to create and is generated on COMPASS–D when no shaping field is applied. The second shape is an up–down symmetric D–shape similar to early JET plasmas. The two shapes in (Fig. 2.2c and d) are distinguished by their X–point. The X–point forms a natural diverter which would allow power and impurities to be drawn away from the main body of the plasma in a reactor. Fig. 2.2c is a single–null diverted (SND) plasma similar to the present JET configuration, and is the expected ITER shape. Figure 2.2d shows a high triangularity single–null diverted plasma (SNT) and is studied on COMPASS-D because of its potentially improved confinement properties.

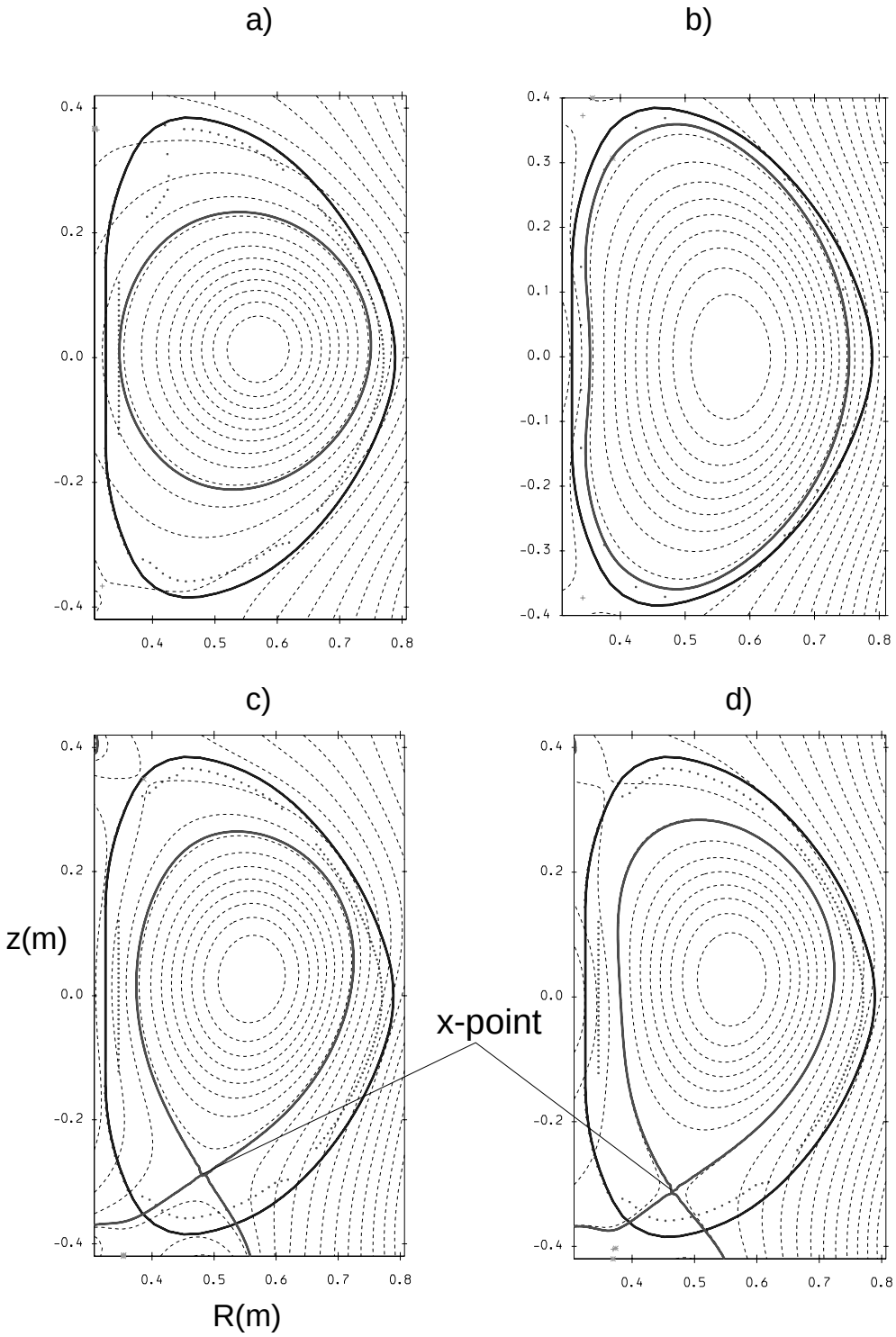


Figure 2.2 Plasma shapes: a) circle, b) up–down symmetric D, c) SND, d) SNT

The magnitude of the toroidal confinement field is often limited due to technological considerations and is an important factor in the financial cost of a tokamak. A measure of the efficiency of the confinement magnetic field is termed the toroidal beta (β) and is defined as the average ratio of plasma pressure to magnetic field pressure. The plasma pressure can be increased by heating the plasma, usually with either high power microwaves or high energy atoms injected into the plasma. It has been observed experimentally that β is limited to a maximum value β_{max} beyond which confinement deteriorates [Lazarus91],

$$\beta_{max} = g_T \frac{I_p}{aB_T} \qquad \textbf{(2.1)}$$

Here I_p is the plasma current in MA, β_{max} is in %, B_T is the toroidal field in tesla, a is the plasma half width in metres, and g_T is the 'Troyon factor' and is usually between 3 and 4 for most tokamaks. The 'safety factor' (q_a) is a measure of the helicity of the field lines and at the edge of the plasma is often approximated

$$q_a = \frac{2\pi abB_T}{\mu_0 R_p I_p} \qquad \textbf{(2.2)}$$

The parameter R_p is the radial position of the plasma measured from the centre line of the torus (in metres) and b is the plasma half height (in metres).
Magnetohydrodynamic (MHD) helical mode instabilities [Wesson87] can occur if q_a falls below 2. Rearranging (2.2) to obtain I_p in terms of q_a and substituting into (2.1) gives

$$\beta_{max} = g_T \frac{2\pi b}{\mu_0 R_p q_a}.$$

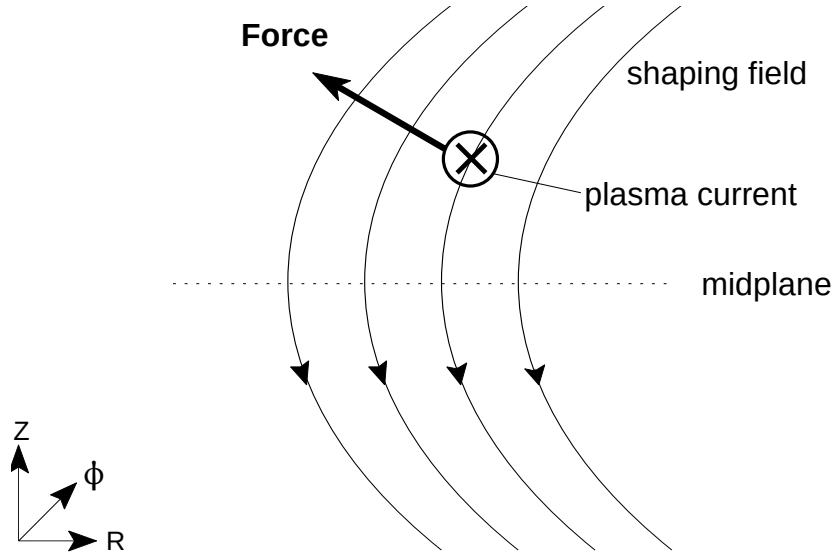


Figure 2.3 Destabilizing forces acting on plasma.

For a given safety factor, β_{max} can be increased by increasing the height of the plasma (and therefore the elongation if the plasma width is limited). Elongated plasmas are produced by applying a quadrupole component to the poloidal field. Unfortunately this causes the plasma vertical position to be unstable as is illustrated in Fig. 2.3. The field lines are curved in a manner representing the quadrupole field required for elongated plasmas. The vertical equilibrium position is at the midplane marked on the diagram. If the position is perturbed upwards then there is a vertical component of the force pushing the plasma away from the equilibrium. As the plasma moves, currents are induced in the tokamak vessel wall and surrounding structures which act to oppose the motion. This passive damping reduces the instability growth rate, but active feedback is required for a stable system.

Plasma instabilities can lead to disruptions, and these have been observed in all tokamaks, including JET and COMPASS-D. (There is an exception which is the START device at Culham which has a much lower aspect ratio (R_p/a).) Disruptions can be caused in different ways and involve a complicated sequence of events. Their main feature is always a sudden loss of plasma energy (this can occur in a few 10s of μs). For a major disruption this event is almost always irreversible and leads to a rapid decay of the plasma current and termination of the plasma discharge.

Increasing β beyond its limit can lead to disruptions. Other types of disruption can be caused by increasing the plasma density beyond its limit. The density limit depends linearly on the plasma current density. Another main cause of disruptions are helical MHD instabilities.

In addition to the rapid loss of energy and decay of the current, large perturbations in the plasma position can occur as a consequence of disruptions. Vertical displacements can be particularly damaging because plasma interactions with the vessel can lead to large electromagnetic forces being exerted. In a large tokamak such as JET, vertical displacements can generate forces of up to 7MN on the vessel wall [Noll89].

2.2 COMPASS-D

COMPASS-D (Fig. 2.4) is a small tokamak at Culham designed to study plasma confinement and instabilities. Different plasma shapes can be studied because different arrangements of shaping coils can be configured easily. Table 2.1 compares the geometry and other plasma parameters of COMPASS–D to JET and ITER. The operating conditions are well away from those required for fusion, but the geometry of the device and non-dimensionless quantities such as β_{max} and the aspect ratio (R_p/a) are similar to that of JET and ITER. COMPASS-D is relatively small and is suitable for studying plasma stability problems because the forces and currents are small and the configuration of control coils and sensor coils can be changed easily. A key advantage of COMPASS–D is that the stability results are broadly applicable to much larger

Table 2.1 Comparison of COMPASS–D, JET and ITER.

	COMPASS–D	JET	ITER
Major radius (R_p)	0.56m	2.96m	8.1m
Minor radius (a)	0.23m	1.25m	2.8m
Elongation (κ)	1.6	1.9	1.7
Plasma current (I_p)	400kA	7.0MA	21MA
Toroidal field (B_T)	1.9T	3.45T	5.7T
Electron temperature (T_e)	1keV	10keV	10keV

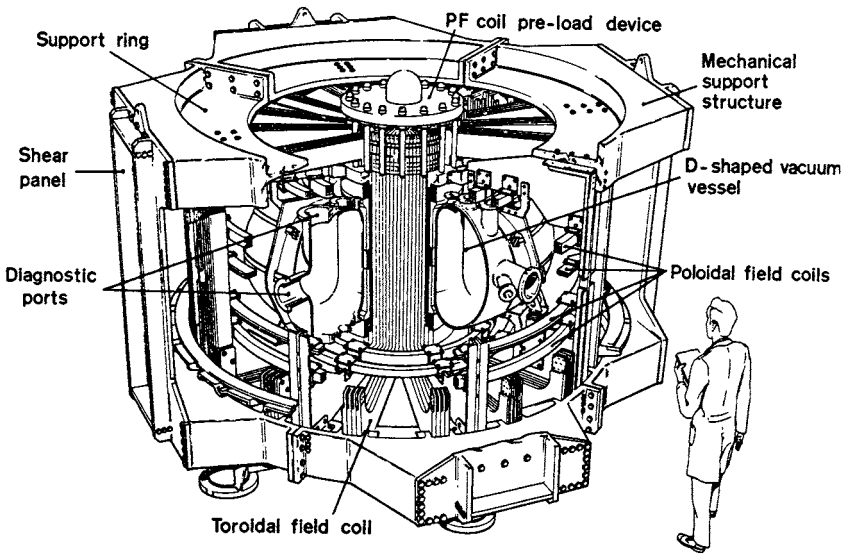


Figure 2.4 COMPASS–D. (Reproduced from [Booth86].)

tokamaks such as JET and ITER. Details of the position control system are provided below.

2.3 Plasma shape and position control

The plasma position and shape is determined by the poloidal field generated by toroidal coils surrounding the outside of the vessel. Fig. 2.5 shows the position of the coils on COMPASS–D. Three separate systems regulate the plasma shape, radial position and vertical position. The plasma shape is open loop controlled by driving a preprogrammed current (I_s) through shaping coils connected in series (marked '*S*' in Fig. 2.5). A thyristor power supply is used to drive the current with a simple P+I control loop used to ensure that the supplied current matches the preprogrammed value. The set of coils used for shaping can be changed between shots to generate different shapes. The main component of the shaping field is quadrupole to create vertically elongated plasmas (Fig. 2.6). Changing the ratio of I_s to plasma current changes the shape of the plasma, with lower values generally resulting in less elongated plasmas.

If currents flow in two parallel wires in opposite directions then a repulsion force is set up between the two wires pushing them away from each other. A similar effect is observed in tokamaks because the current in opposite sides of the torus flows in opposite directions. A large vertical field is required to provide an inward force balancing the outward 'hoop force' of the plasma current. The radial position is open loop stable but feedback is used to regulate the position. The coils marked 'B_z' generate a vertical field (Fig. 2.7) controlling the radial position (the $J \times B_z$ direction of the force acts radially). The B_{zs} set are driven by thyristor power supplies and the B_{zf} set are driven by a transistor amplifier which acts on a faster time scale but supplies less power. The current in these coils is driven in response to radial position measurements using a P+I controller.

The 'B_R' coils (Fig. 2.8) generate a radial field controlling the vertical position. The plasma vertical position is usually open loop unstable with relatively fast time scales. A P+D controller is used in a feedback loop with a transistor amplifier to drive the control coils. The shape and position loops are effectively decoupled from each other. The shaping field is preprogrammed and usually constant throughout a shot. The radial position is stable and with relatively slow dynamics and the vertical position is unstable on relatively fast timescales. The vertical and radial field coils are chosen to minimize coupling so the vertical stability problem can be considered independently of the other parameters.

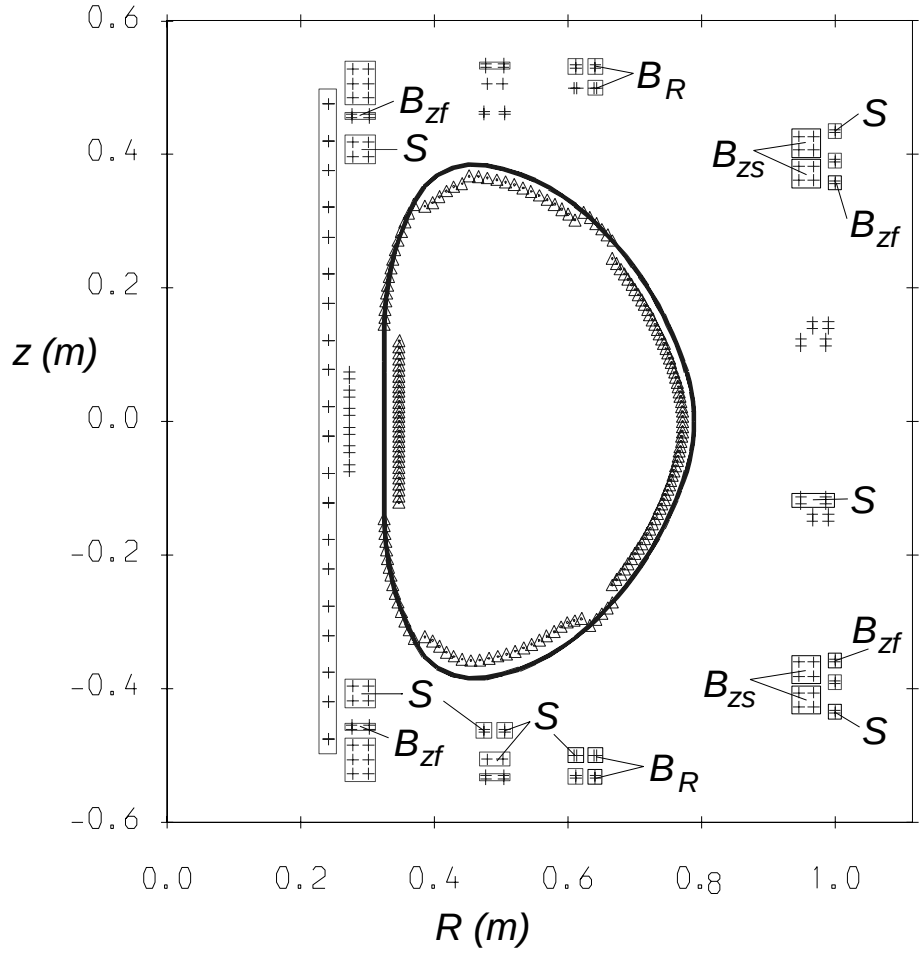


Figure 2.5 COMPASS–D poloidal field system. *S* – shaping coils for typical SND plasma, B_z – vertical field coils, B_R – radial field.

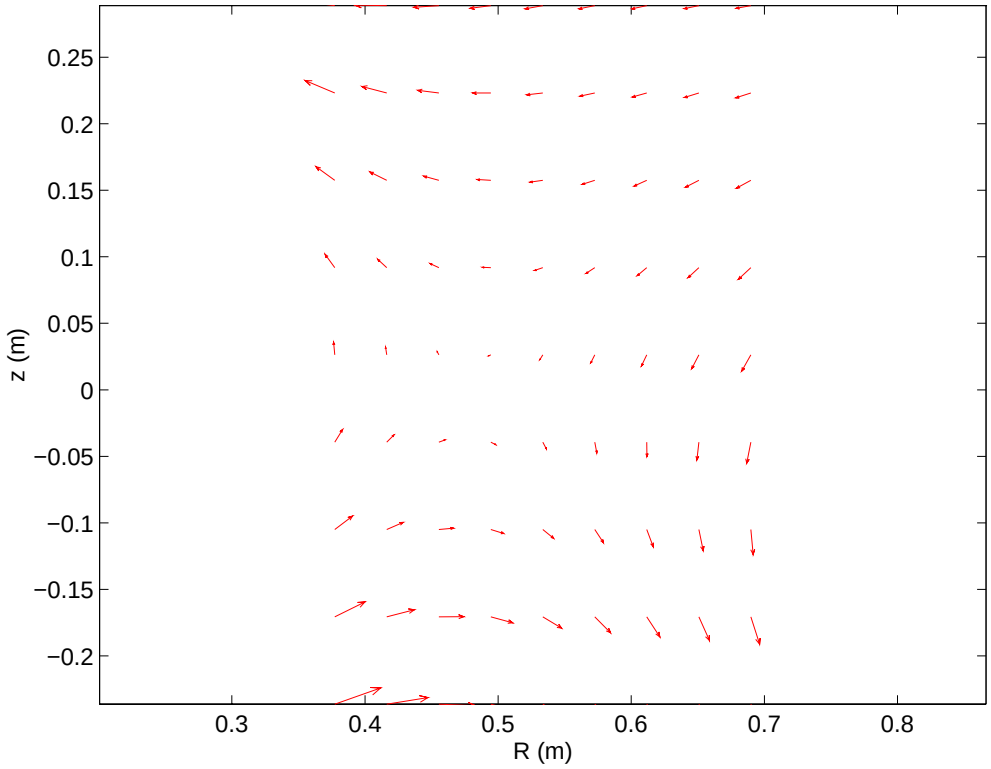


Figure 2.6 Shaping field from shaping ('*S*') coils for positive plasma current (i.e. plasma current flows into page).

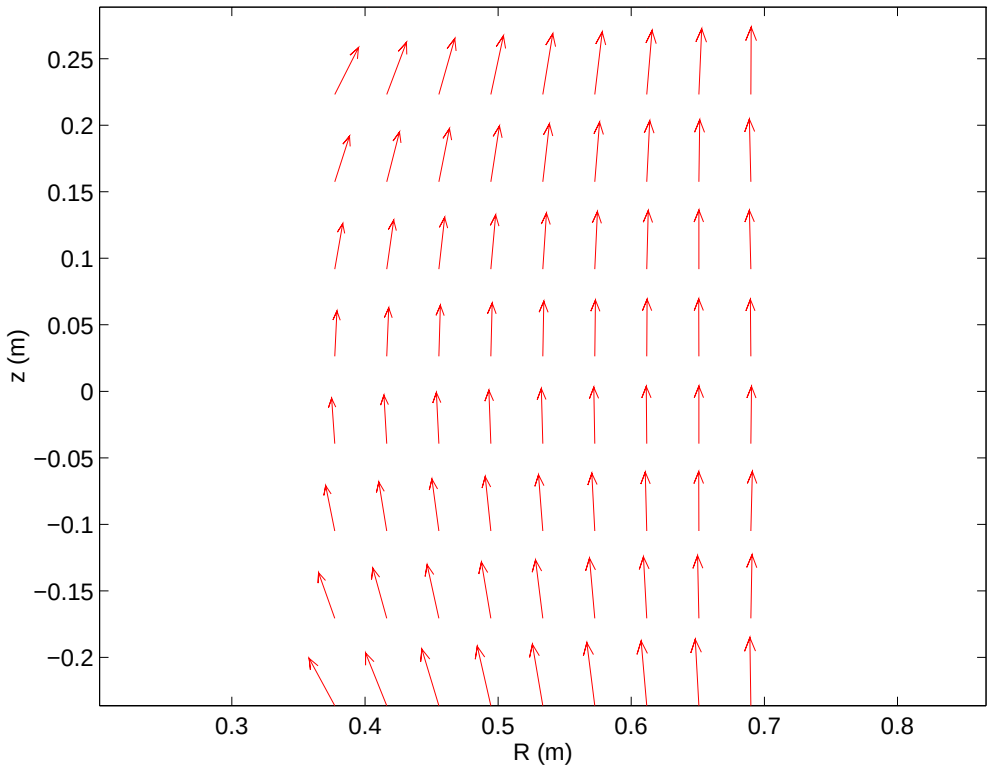


Figure 2.7 Field from B_{zf} coils.

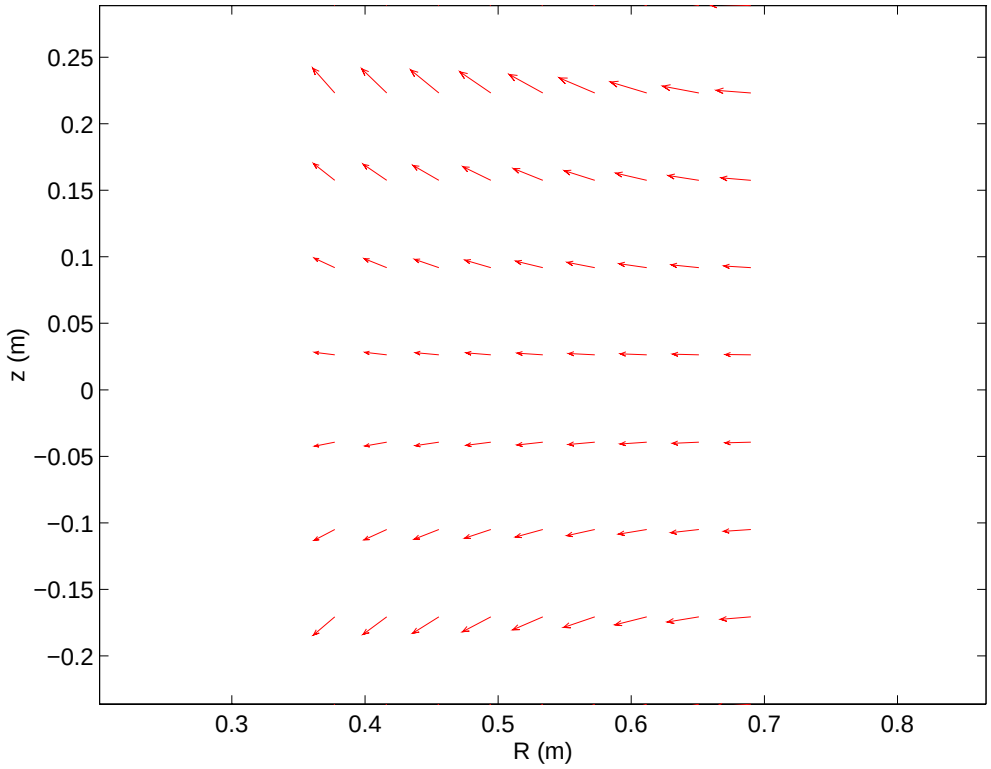


Figure 2.8 Magnetic field from B_R coils.

2.4 Plasma vertical position

The quadrupole shaping field used to generate vertically elongated plasma causes the vertical position instability. The instability growth rate depends on the ratio of the destabilizing force gradient due to the curvature of the field lines and the damping force gradient due to coupling to the vessel wall. Both these factors depend on the current profile and position of the plasma. A simple relationship can be obtained by considering a simple single current filament (with current I_p) model of the plasma [Lazarus90]. The net (vertical) force on the plasma at equilibrium is zero but if the position is perturbed, destabilizing forces in the $J \times B_R$ direction push the plasma away from equilibrium. The radial component of the equilibrium field is approximated using a first order Taylor series so that the 'destabilizing force' (F_d) is

$$F_d = -2\pi I_p R_p \frac{\partial B_R}{\partial z} z$$

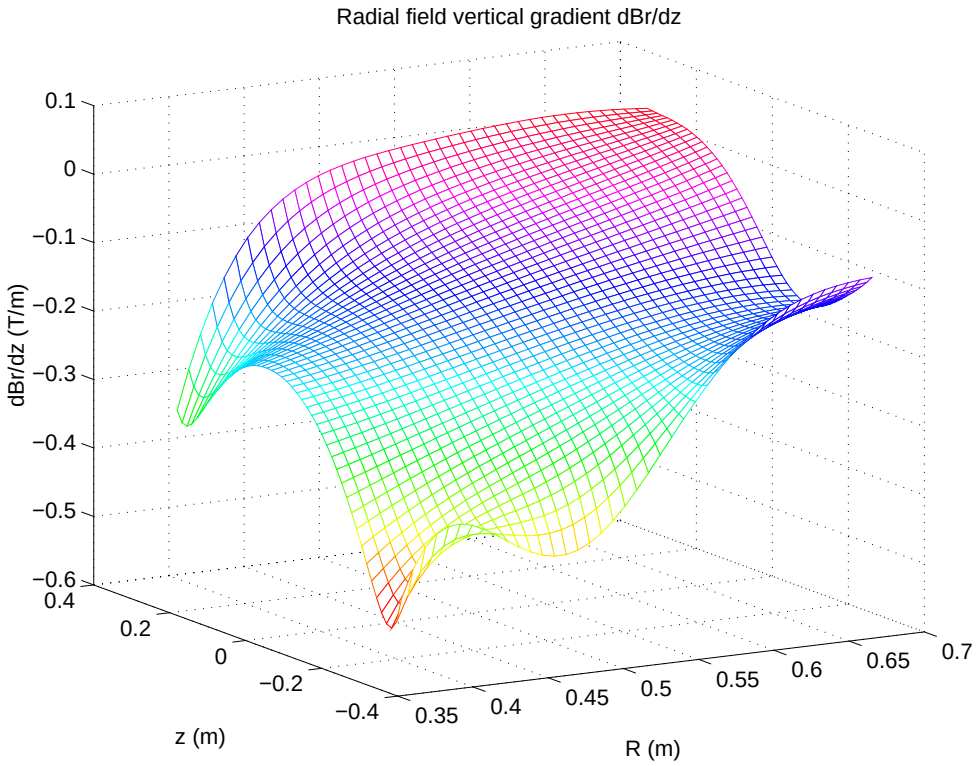


Figure 2.9 B_R' field plot from poloidal field coils for typical SND plasma (Shot no. 17190, I_p=171kA).

A positive direction of plasma current is assumed. As the plasma moves currents are induced in the vessel wall which act to oppose the motion of the plasma. This force (the 'stabilizing force' F_s) is

$$F_s = I_v \frac{\partial M_{vp}}{\partial z} I_p$$

where I_v is the current induced in the vessel wall and M_{vp} is the mutual inductance between the plasma and the vessel wall. The mass of the plasma is very small (of order of milligrammes) compared with the size of the forces (of order of newtons) acting on it, allowing the use of the force balance approximation (neglecting the high frequency poles)

$$0 = I_v M_{vp}' I_p - 2\pi R_p B_R' z I_p \qquad \textbf{(2.3)}$$

(prime denotes the derivative with respect to vertical position). The current induced in the vessel can be obtained from Kirchhoff's voltage law

$$L_v\dot{I}_v+R_vI_v+M_{vp}^{/}\dot{z}I_p=0 \qquad \textbf{(2.4)}$$

(dot denotes the derivative with respect to time). The plasma current is assumed constant $(\dot{I}_p=0)$ and R_v and L_v represent the vessel resistance and self–inductance respectively. Taking Laplace transforms and substituting (2.4) into (2.3) gives

$$s(M_{vp}^{/2}I_p+2\pi R_pB_R^{/}L_v)z+2\pi R_pB_R^{/}R_vz=0$$

(s is the Laplace transform variable). The equation has a root $s=\gamma$ at

$$\gamma=\frac{-2\pi R_pB_R^{/}R_v}{M_{vp}^{/2}I_p+2\pi R_pB_R^{/}L_v}$$

If B_R' is positive then the root is negative and the system is stable. For vertically elongated plasma (and positive I_p) B_R' must be negative, and if the magnitude of B_R' is small enough such that $|B_R^{/}|<(M_{vp}^{/})^2I_p/2\pi R_pL_v$, then the system is unstable with growth rate γ. Increasing the plasma elongation requires a more negative B_R' and the instability growth rate increases. As B_R' tends to $(M_{vp}^{/})^2I_p/2\pi R_pL_v$ then γ tends to infinity and the massless approximation breaks down. The instability time constant is often expressed as $\tau=\tau_vm_s$ where $\tau_v=L_v/R_v$ is the time constant of the vessel and m_s is the plasma 'stability margin'

$$m_s=\frac{M_{vp}^{/2}I_p}{-2\pi R_pB_r^{/}L_v}-1$$

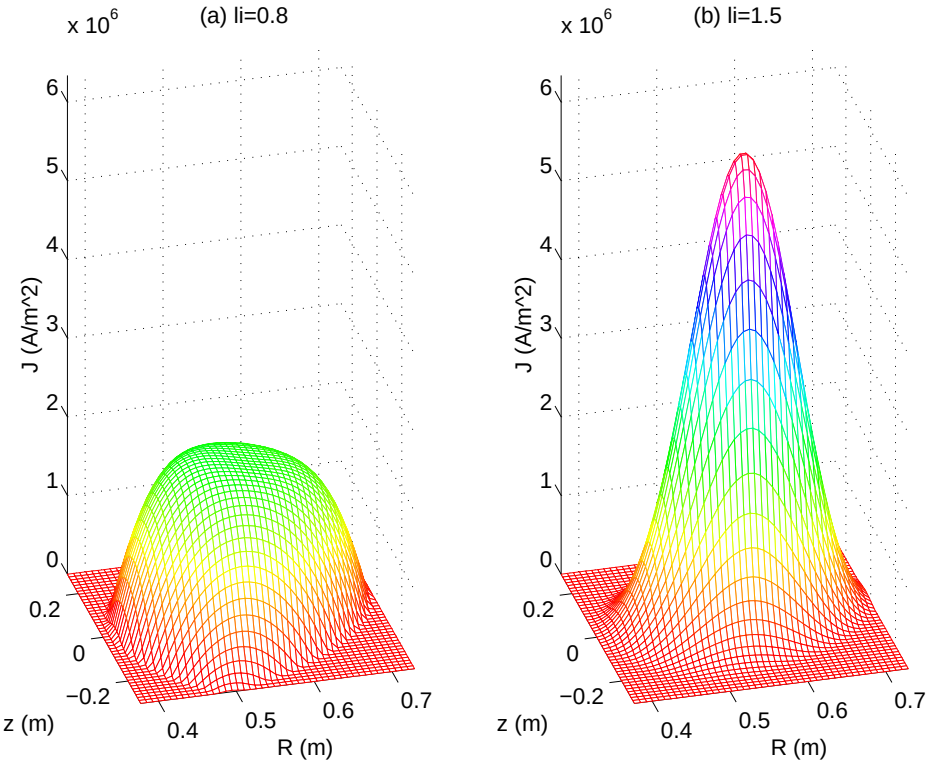


Figure 2.10 Equilibrium solutions of current density profile for SND plasma, I_p=171kA.

The radial field vertical gradient (B_R') is proportional to the shaping current I_s and is negative. Increasing the I_s/I_p ratio results in greater plasma elongation. This in turns causes higher instability growth rates.

The instability growth rate depends on plasma parameters including the radial and vertical position. Other factors such as current density and plasma pressure profiles are also important [Ward93]. Moving the plasma closer to the vessel wall generally increases the coupling to the wall and improves the stabilizing force F_s. However the radial field vertical gradient is more negative on the inner side and the bottom of the vessel (Fig. 2.9). Moving the plasma in these directions increases the destabilizing force. COMPASS–D plasmas typical operate at the same position and little change in stability is observed.

The plasma current density profile is also important in determining stability. Figure 2.10 shows two current density profiles characterized by the plasma internal inductance (l_i). The destabilizing force (F_d) acting on the plasma is determined from integrating $J \times B_R'$ over the plasma volume. Even if the shaping field remains constant

different current profiles will encounter different current weighted radial field gradients $B_R^{/}$. Broad profiles (Fig. 2.10a) have more current at positions close to the wall, increasing the coupling to the vessel. The stabilizing force (F_s) is generally larger and therefore the plasma should be less unstable. However the destabilizing force is also larger since the plasma occupies a greater part of the more negative regions of radial field vertical gradient. The current density profile is difficult to measure but is linked to the helicity of the field lines and the safety factor (2.2). The shape is not frequently changed on COMPASS–D but toroidal fields in the range 1.1T to 1.9T and plasma currents in the range 90kA to 320kA are often used. Low toroidal fields tend to lead to broader current density profiles. Other changes to the profile can occur when the plasma operates with parameters causing high energy confinement times (H–mode) compared with normal operation with low confinement times (L–mode).

For a typical SND plasma on COMPASS–D the destabilizing force (F_d) is the more dominant factor in determining if the plasma is more or less unstable. The vessel wall is relatively thin (3mm thick inconel) with time constant (τ_v) similar to the instability time constant $\tau \sim 0.5\text{ms}$.

2.5 COMPASS-D vertical position control loop

Figure 2.11 contains a schematic diagram of the vertical position control loop. A P+D controller is used to drive currents in coils generating a radial field and providing a vertical force on the plasma. The proportional signal is obtained from velocity sensors outside the vessel measuring magnetic flux. A separate velocity signal is obtained from sensors inside the vessel. The two signals are added to reference waveforms and then multiplied by the appropriate gain. The resulting two signals are then summed and transmitted via an analogue optical link to a high power transistor amplifier. The amplifier then drives the control coil currents. The details of the loop are presented below, along with results from a typical shot and some details of the disturbances observed on COMPASS–D.

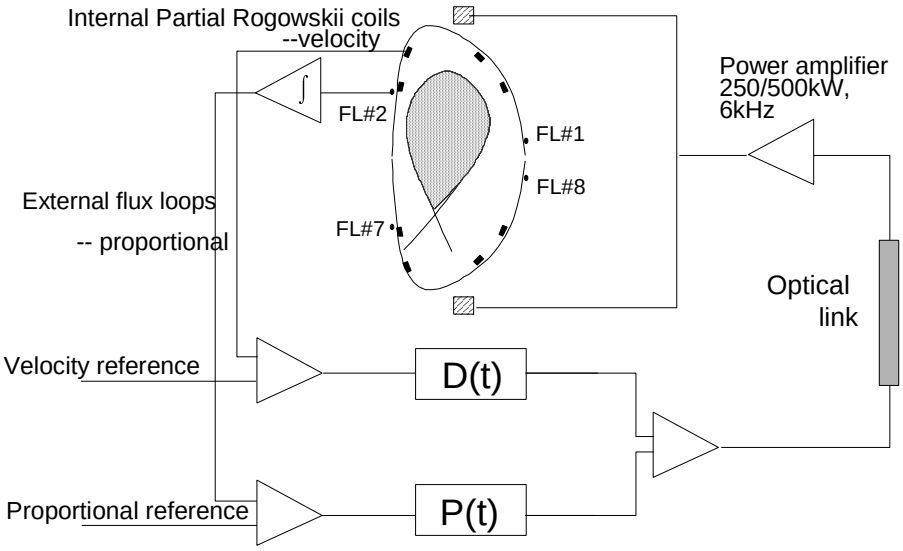


Figure 2.11 Vertical position control loop.

2.6 Position sensors

Two separate sensors are used to detect the vertical position and velocity of the plasma. The position signal is obtain by summing and then integrating the signals from four toroidally continuous flux loops (FL) outside the vessel. A flux loop is a toroidal coil measuring flux and eight are distributed poloidally around the vessel. The voltage induced in a flux loop is given by Faraday's law

$$V_{FL} = -2\pi \int_0^{R_{FL}} \frac{dB_z}{dt} R dR$$

The voltage is proportional to the time derivative of the vertical component of the magnetic flux linked by the loop. If the plasma moves upwards then the flux linked by FL#1 (Fig. 2.11) increases and that by FL#8 decreases. Subtracting the FL#8 voltage from the FL#1 voltage provides a signal closely proportional to the vertical velocity of the plasma. A similar signal can be obtained from two flux loops on the inboard side of the vessel and summing both inboard and outboard measurements reduces the sensitivity to radial position movements. This velocity signal is integrated to provide the position signal. The integrator has a gain

$$G_i = -2000$$

The FL position measurements are not sensitive to helical modes but are shielded by the vessel wall which acts as a low pass filter.

Higher bandwidth measurements of velocity are obtained from coils inside the vessel. Internal partial rogowskii (IPR) coils in COMPASS–D are short sections of tightly wound solenoids 30mm long, distributed along the inside of the vessel. They measure long wavelength components of the poloidal field because small wavelengths (below ~30mm) are cancelled out. This makes the IPR signals sensitive to gross plasma position changes but less so to small scale turbulence. Eight IPR coils at one toroidal location are summed giving a measurement of velocity. These measurements have a higher bandwidth than the FL velocity but are sensitive to helical modes and are more noisy.

The plot in Fig. 2.12 compares the position signals from the FL and IPR coils with a position obtained from last closed flux surface (LCFS) reconstructions. The shot is for a standard SND shape with plasma current I_p=143kA. The DFIT computer program (written by Dr. L.C. Appel, UKAEA Fusion, Culham, UK) reconstructs the plasma last closed flux surface from all the flux loop and partial rogowskii coils outside the vessel wall, along with measurements of poloidal field coil currents. It can be used to obtain the plasma current centroid position with respect to the midplane. In the plot the position is perturbed with steps on the reference signal. The polarity of the reference is inverted with respect to position because the FL position signal is added to it, rather than subtracted to form an error signal.

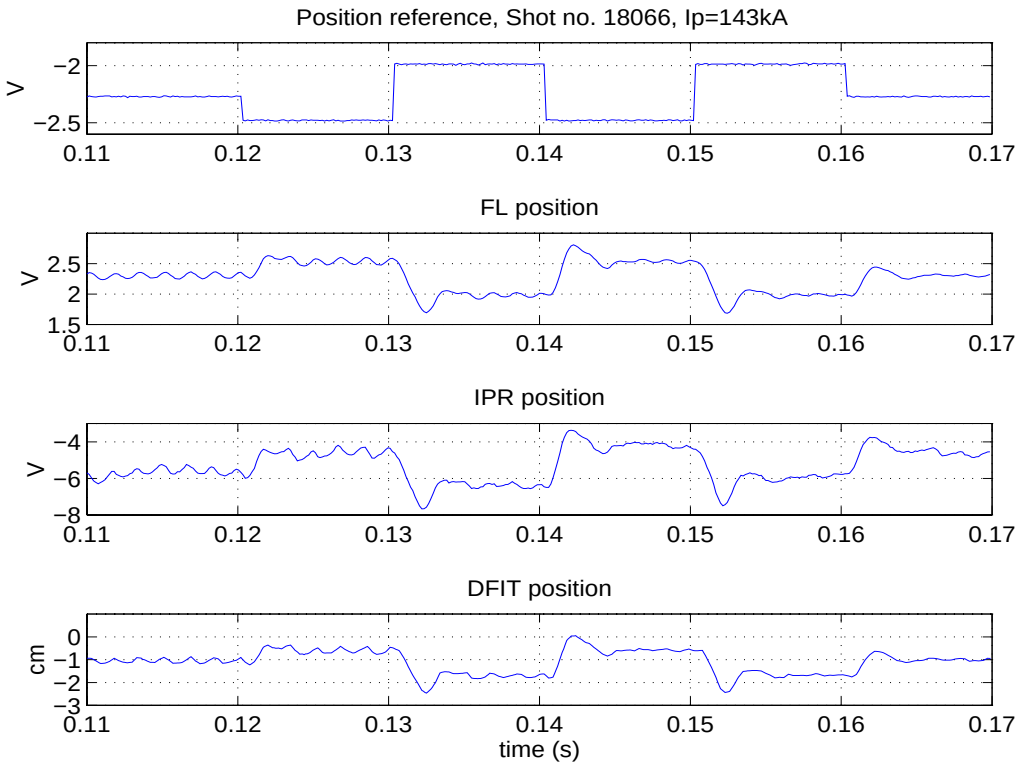


Figure 2.12 Step responses.

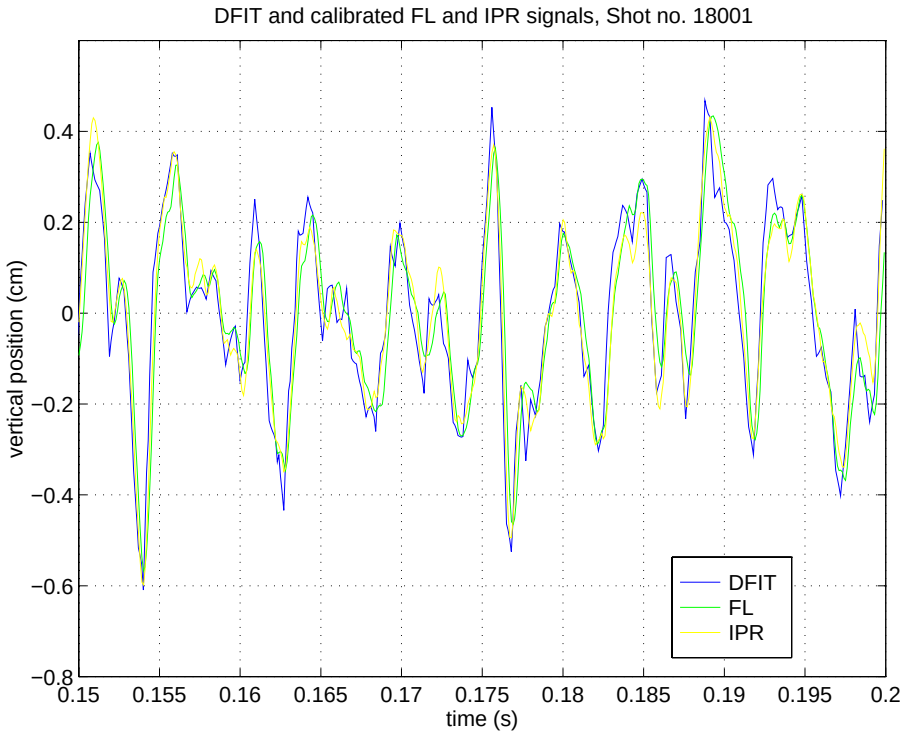


Figure 2.13 Position from LCFS reconstruction and calibrated FL and IPR signals.

Both the FL and IPR signals are proportional to the plasma current which is constant for most of a typical shot. In addition there is a steady state offset obtained from integration during the early startup phase of the shot, when the plasma shape changes from a circle. The current centroid is ~1cm below the midplane throughout the shot, but the FL and IPR position offsets (+2.3V and −6V respectively) have different polarities. Up–down symmetric plasmas have no offset but the SND shape often used in COMPASS–D introduces a DC offset into the position signals, affecting the FL and IPR signal differently. The FL and IPR signals closely match the DFIT signal, with all exhibiting a weakly damped response. It is possible to detect a small upward drift in the IPR signal throughout the plot. A +1cm change in DFIT position is approximately equivalent to +0.5V change in FL signal and a +2V change in IPR signal (for a 143kA plasma).

Figure 2.13 contains the DFIT and calibrated FL and IPR position for a shot with broadband position excitation up to 10kHz. The offset and linear drift are removed from each signal and a least squares fit used to find the calibration constants, giving

$$\Delta z_{DFIT} = 1.8 \times \Delta z_{FL}$$
$$\Delta z_{DFIT} = 0.47 \times \Delta z_{IPR}$$

where z_{DFIT} is the position of the current centroid in cm and z_{FL} and z_{IPR} are the FL and IPR position signals in volts. The plasma current is 142kA and the shape is the standard SND. The measured signals follow the DFIT position closely, indicating that a linear mapping from magnetic signals to position is a reasonable approximation for position regulation. It would be expected that shielding of the external signals by the vessel would attenuate the FL and DFIT high frequency components. The dominant frequency components of the position signals are below 1kHz and therefore the shielding effect is not clearly seen in the plot.

2.7 Actuator

The controller demand is output through an analogue optical link which electrically isolates the circuit and is resistant to electromagnetic interference. The link has a pure time delay of 13μs and a 3dB bandwidth of 10kHz. Frequency response measurements lead to the model

$$G_l(s) = e^{-s\tau_{ld}} \frac{1}{(\tau_l s + 1)^2}$$

where $\tau_{ld} = 13\mu s$ and the double pole is at $-1/\tau_l = 30000\pi$. Below 1kHz the link can be approximated as a pure time delay of 32μs because there is no significant change in the magnitude of G_l and there is an approximately linear phase lag.

A power amplifier consisting of a transistor amplifier (or two connected in series) drives the control coils. If two amplifiers are connected in series then the controller gains are halved to ensure that the loop gain remains constant. Each amplifier has a specification of ±50V and ±5kA and a 16kHz bandwidth. The output impedance is less than 1μH. The input electronics used typically consist of a current limiter protection circuit which introduces a pure time delay and a 6kHz low pass filter. The amplifier can be modelled as

$$G_a(s) = e^{-s\tau_{ad}} K_a \frac{p_a \bar{p}_a}{(s - p_a)(s - \bar{p}_a)}$$

Here $\tau_{ad} = 31\mu s$ and $p_a = -26657 + 26657j$ and overbar denotes complex conjugation. The gain $K_a = -57.6$ is the overall gain of the power amplifier gain (×6) and preamplifiers.

The control coils are made from copper and are connected in anti–parallel above and below the plasma. The self–inductance and resistance of the coils including leads was measured from a step response and are $L_c = 94.787\mu H$ and $R_c = 11.45m\Omega$ respectively. The transfer function from the voltage across the coils to the current through them is

$$G_c(s) = \frac{1}{L_c s + R_c}$$

For the test the coils were driven by the transistor amplifiers in open loop with no other part of the plant operating. The amplifier current and voltage step response were used to calculate the impedance.

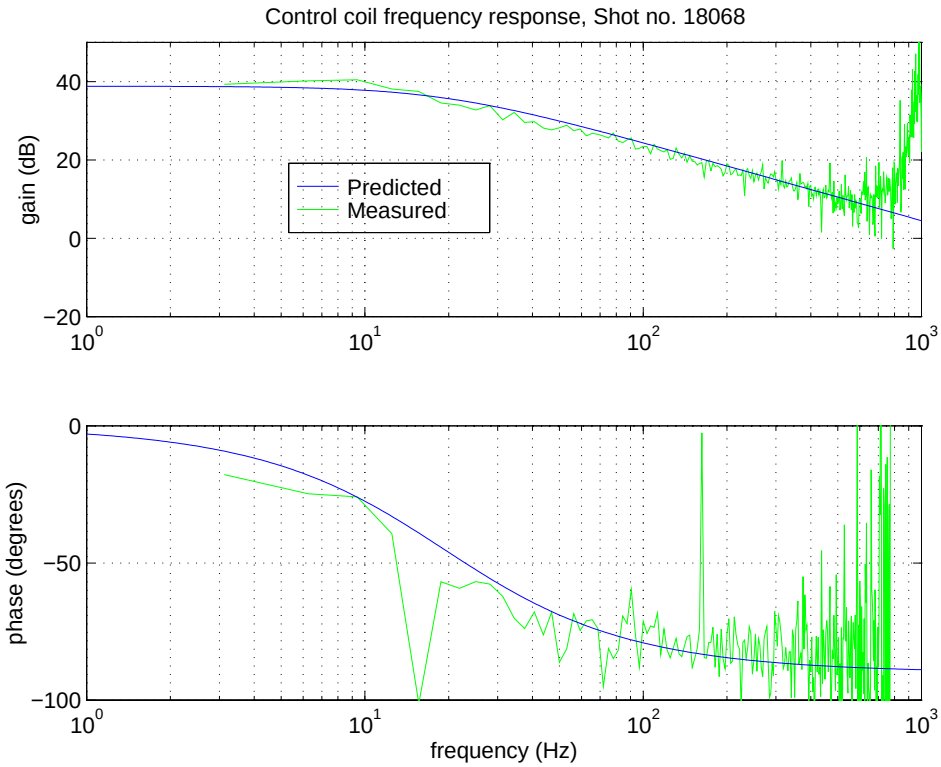


Figure 2.14 Measured and predicted (R_c=11.45mΩ and L_c=94.79μH) frequency response of control coil.

It is possible that skin effects can significantly change the impedance of the coils at high frequencies. For example in a plane conductor the current density decays to 1/e times the density at the surface at the skin depth δ, which depends on frequency [Ramo84, Section 3.17]. For copper the skin depth is

$$\delta = \frac{0.0660}{\sqrt{f}}$$

where δ is in metres and f is the signal frequency in Hz. If the dimensions of a conductor are relatively large then, at a high frequency, the current is restricted to flowing in a fraction of the cross–sectional area and the impedance of the conductor is increased. The effect of skin depth on vertical position control coils in the JT–60 Upgrade tokamak is considered in [Humphreys92]. The dimensions of the control coils on COMPASS–D are much smaller than JT–60 Upgrade but the bandwidth of the loop is larger. There are four windings each of rectangular shape (18mm×8mm) and with a hole of 4mm diameter in the centre. Two of the windings have a major

diameter of 924.5mm and the other two 1257.1mm [Valovič91]. For copper a skin depth of 4mm corresponds to a frequency of 272Hz, which is relatively low compared with the open loop instability growth rate of order 2500 rad/s or closed loop bandwidth of order 1kHz.

The frequency response was measured experimentally by driving the coils in open loop using the transistor amplifier. The input signal was a normally distributed random sequence with frequency 1kHz, and the input and output data was sampled at 10kHz. The Empirical Transfer Function Estimate (ETFE) defined in [Ljung87, Chapter 6] is a simple method of estimating the frequency response and was formed by dividing the Discrete Fourier Transform (DFT) of the coil current by the DFT of the voltage. The result (Fig. 2.14) should be an unbiassed estimate of the frequency response but may have relatively large variances compared with other frequency response estimation methods [Ljung87, Chapter 6]. However in this case the signal to noise ratio of the data is very large and the variance of the estimates expected to be small. The measured estimate is in reasonable agreement with the single pole model G_c and so the skin depth effect is negligible in this case.

2.8 Controller

An analogue P+D controller is used to control the plasma vertical position. The position and velocity signals are added to reference waveforms and then multiplied by P and D gains respectively. Multiplying waveform generators are used to provide the reference signals and also to multiply the error signals with a time varying gain. The gains are preprogrammed digitally and up to 8192 gains can be stored with the change interval either 10 or 100μs. Reference signals are generated by fixing the input at a constant voltage. The velocity reference is almost always set to zero and the proportional reference signal is usually constant for most of a plasma shot. The reference signals are added to the position and velocity signals using summers with gain

$$G_s(s) = -9.04.$$

The position error and velocity error are multiplied by gains K_p and K_d respectively and then the two signals are summed. The typical values of the gains are

$$K_p = 0.133 \text{ and } K_d = 0.150.$$

The multiplying waveform generators and summing circuits are high performance circuits with bandwidths exceeding 100kHz.

A digital signal processor is used in some experiments. The device is an AT&T DSP32C (50MHz, 32–bit floating point) which is capable of up to 25Mflops. Two ADC input channels and two DAC output channels are available with 16bit resolution and sampling frequency of up to 200kHz. The signal input and output buffers are Bessel filters with 50kHz bandwidth each introducing approximately a 3μs time delay. The ADC and DAC circuits each include a one sample data buffer which, with the DSP itself, introduces overall a 3 sample delay into the system. For a sampling rate of 20kHz this would amount to 150μs. However in typical use this delay is reduced by selecting a sampling frequency of 80kHz and processing the average of every four samples. The DSP system delay is only 37.5μs, along with the averaging which is equivalent to a simple FIR (finite impulse response) filter. The DSP is programmed in assembly language making use of filter implementation subroutines supplied with the system. The filter coefficients are obtained after converting the required controller transfer functions to direct form II second order sections [Oppenheim89, Section 6.9.3].

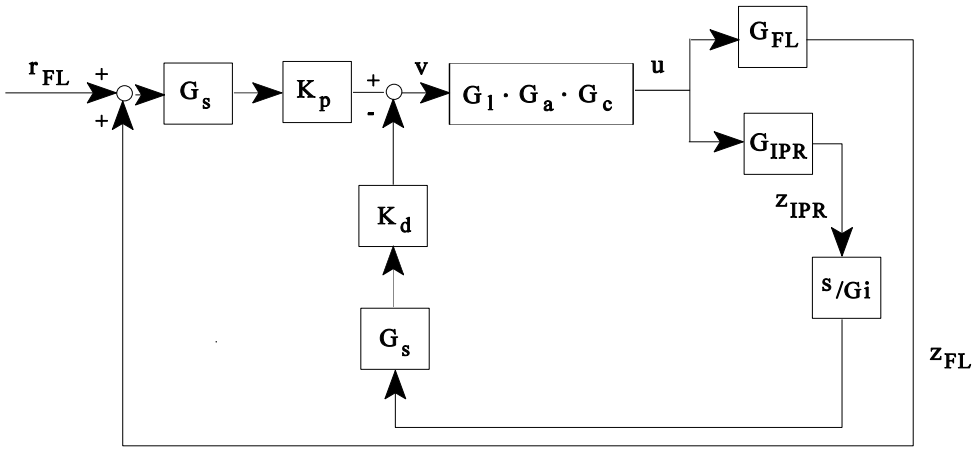


Figure 2.15 Block diagram of vertical control loop with P+D controller.

2.9 Plasma operation

A block diagram of the analogue P+D control loop is shown in Fig. 2.15. The transfer functions G_{FL} and G_{IPR} represent the response of the plasma position as measured by the FL and IPR coils (including integrators) to the control coil current (u). The position reference is r_{FL} and the control signal is v. The position and velocity signals are z_{FL} and $\dot{z}_{IPR}$ respectively. Plasma current and control loop signals for a typical SND shot are shown in Fig. 2.16. In the startup phase the plasma current is ramped up in the first 30ms, followed by a ramp in the shaping current to change the shape from a circle to the standard SND shape. The flattop period of the shot lasts for over 200ms and is the period of most interest for experiments. The plasma shape and current are held constant with the ratio I_s/I_p~5%. The end of the shot is marked by the current rampdown.

The plasma is stable before the shaping field is applied, and the controller proportional and derivative gains are ramped up with the shaping current to their flattop values. The gains are empirically chosen and give nearly damped step responses. The reference position waveform is also ramped to take account of the offset introduced in the signal. The two position measurements and amplifier output are shown in more detail in Fig. 2.17. All the signals have a large 600Hz component which is introduced into the system from 12 phase thyristor power supplies which drive the plasma current and vertical and shaping fields. The frequency spectrum of the amplifier voltage (Fig. 2.18) shows components exist at 600Hz and harmonics. The actual oscillation of the plasma position is estimated to be small (less than 1mm amplitude), but large voltage swings are present in the amplifier (amplitude ~20V) reducing the effective output headroom. The 600Hz signal is predominant only in SND and SNT plasmas. In circular and up–down symmetric elongated plasmas (as in Fig. 25a and b) the 600Hz component is much smaller (~5V amplitude amplifier oscillations). This may be an indication that the oscillations are caused by ripples in the shaping and vertical fields disturbing the plasma vertical position, rather than pickup of 600Hz noise from the position sensors.

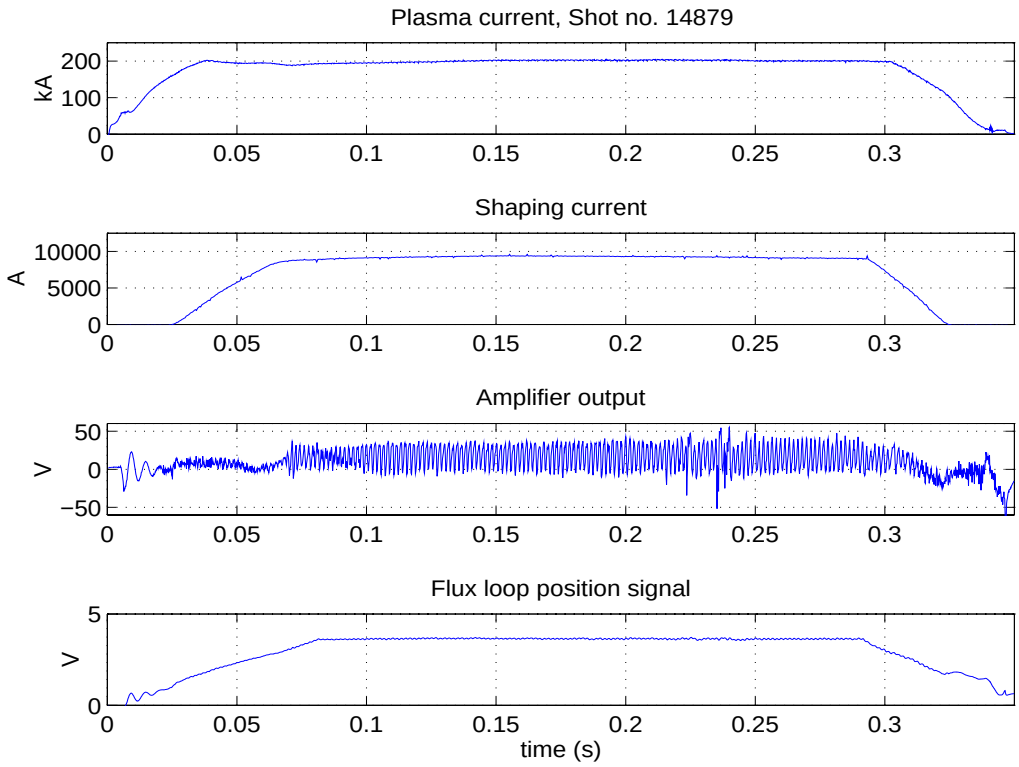


Figure 2.16 Vertical position control signals for typical shot with P+D controller.

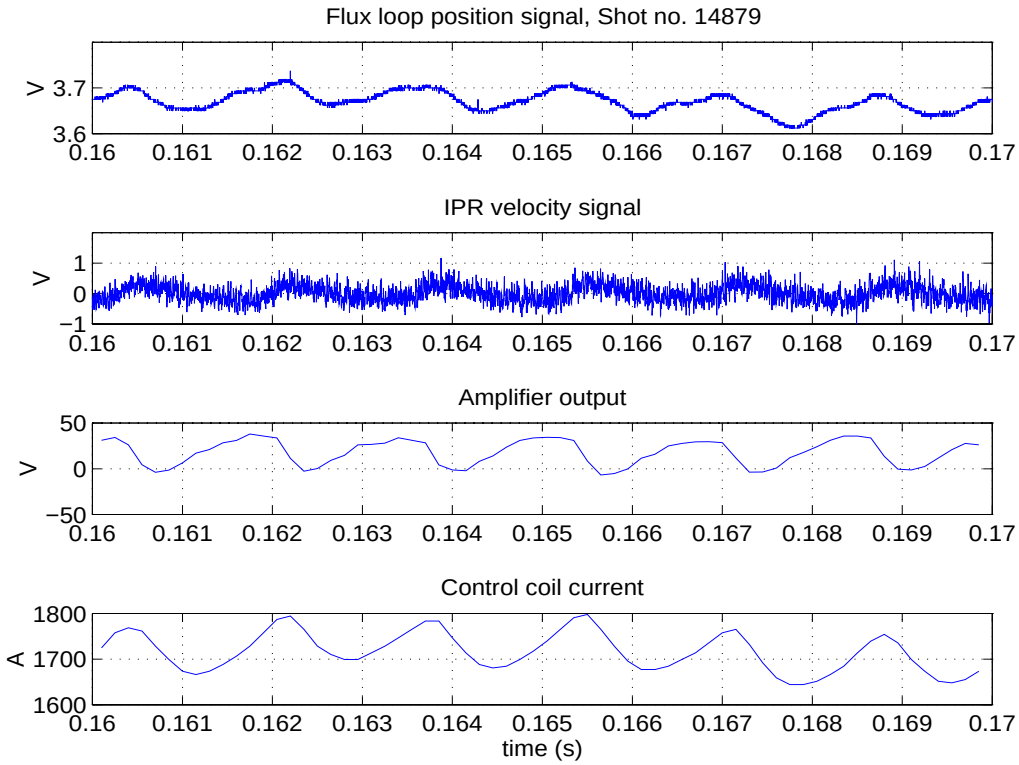


Figure 2.17 Detail of typical shot showing dominant 600Hz signal.

The IPR signal also has a large high frequency component and is compared with the FL velocity signal in Fig. 2.19. The plasma position is perturbed by a broadband random reference signal up to 10kHz. The low frequency gains of the signals have been normalized to allow a comparison of the amplitude roll off. At ~1kHz the FL signal is 3dB smaller than the IPR signals and rolls off more quickly. This could be due to shielding of the flux loops by the vessel wall and the pickup of MHD turbulence by the IPR signal. The vessel time constant is difficult to determine but theoretical estimates for radial field penetration through the vacuum vessel range from 420μs to 470μs and measured values are in the range 660μs to 670μs [Valovič94]. These values suggest a 3dB bandwidth of ~300Hz which is lower than the ~1kHz observed bandwidth. Beyond 5kHz the IPR noise floor is approximately ten times larger than the FL noise.

Plasma disturbances are often observed in operation of the plasma. One frequently observed disturbance is due to Edge Localized Modes (ELMs) in which the outer layer of the plasma rapidly dissipates energy. This is accompanied by a redistribution of the current density and pressure profiles. A change in the current density distribution changes the net vertical force acting on the plasma, leading to vertical position disturbances. In Fig. 2.20 the plasma is in L–mode (Low energy confinement time) up to 0.12s and the position and amplifier signals show the characteristic 600Hz oscillation. Changes in the plasma parameters cause the plasma to operate in the ELM–free H–mode (High energy confinement time). A step change in position (~4mm) and control coil current (~200A) can be observed at the same time. ELMs occur after 0.164s and are characterized by the spikes on the H_α signal measuring the intensity of light from the edge of the plasma. Each spike corresponds to an ELM. During the ELMy H–mode period the amplitudes of the ELMs decrease as the frequency increases and disturbances in the plasma position (up to ~2mm excursions) are clearly observed. ELM frequencies in the range 400Hz to 2kHz are frequently observed on COMPASS–D. Higher frequency ELMs also occur but are less clearly observed because their signal amplitudes are of the same level as noise. Large separated ELMs cause large impulse–like response excursions in the plasma position (~2mm peak to peak) and demand large voltages from the control amplifiers. Figure 2.21 shows a typical amplifier input and FL position response to large

separated ELMs, with the present P+D controller. Large ELMs can sometimes cause the amplifiers to saturate, occasionally leading to loss of stability (see [Todd93] and [Morris95]).

2.10 Discussion

Increasing the plasma vertical position can improve the efficiency of a tokamak. However the vertical position of vertically elongated plasma is open loop unstable and increasing the elongation leads to an increase in the instability growth rate. The consequences of loss of control in a large tokamak such as JET are severe and this is a key issue in the design of the ITER tokamak.

The details of the vertical position control system of COMPASS–D are presented in this chapter, along with observations on disturbances observed in operation. The 600Hz noise is observed on COMPASS–D and JET [JET95, p. 23]. Attenuation of this signal would enable less power to be used in the position control loop. The presence of 600Hz noise in ITER would depend on the type of power supplies used and in any case would be less important because of the large time constants in the system. The effect of large separated ELMs leading to amplifier saturation is also observed on JET. It is possible that this could contribute to loss of control, see [Lingertat95]. ELMs may be present in ITER and could be an important disturbance.

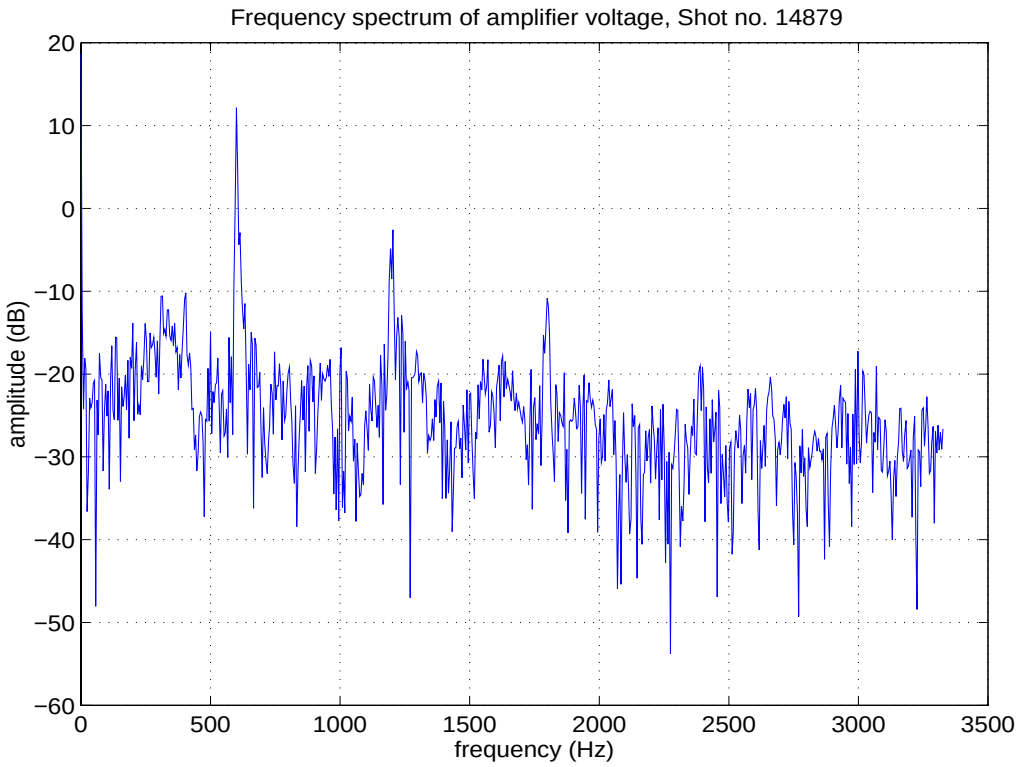


Figure 2.18 600Hz component and harmonics in amplifier voltage.

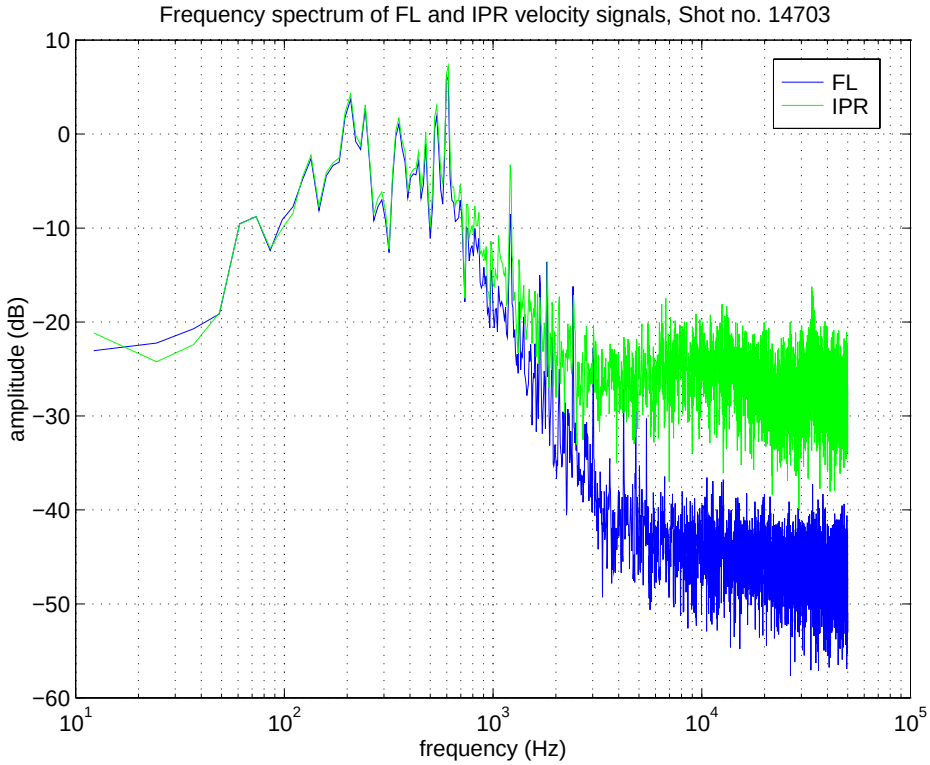


Figure 2.19 Amplitude spectra of IPR and FL velocity signals with low frequency amplitude normalized.

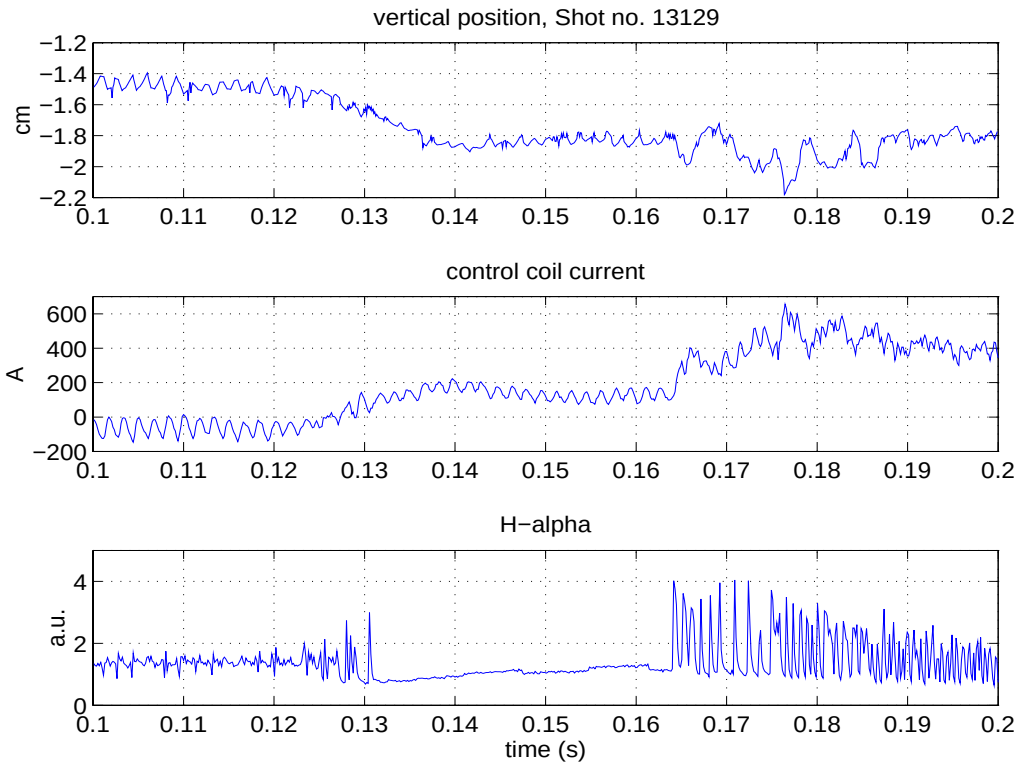


Figure 2.20 L–mode, ELM–free H–mode and ELMy H–mode operation.

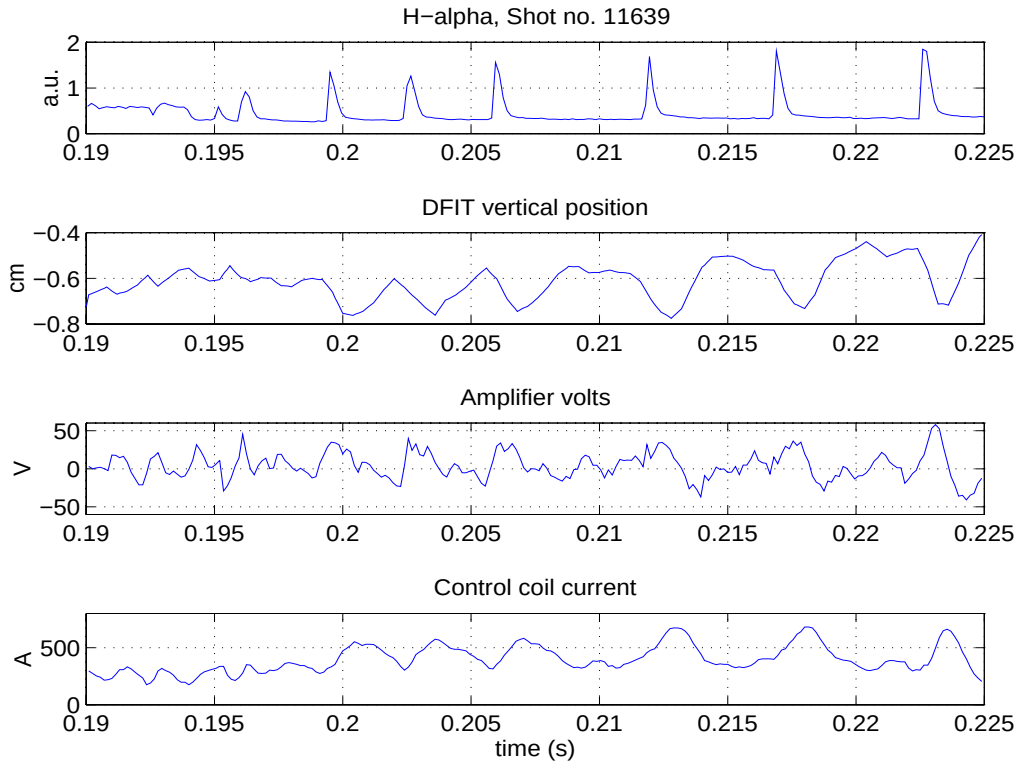


Figure 2.21 Large separated ELMs.

3 System Identification

System identification is the technique of identifying dynamical models from experimental data. It has been used on COMPASS–D to model the open loop response of vertical position signals to control coil currents. An example of some of the modelling results is presented in the next section. The identification process requires many decisions to be made concerning, for example, the identification method, model structure, model order etc., and the decisions made and reasons are described in the following sections. The main results for the plasma vertical position response are presented later in the chapter, along with some analysis of the results. The definitions and mathematical ideas in this chapter are obtained mainly from [Ljung87, Chapters 4 and 7 to 9] where they are described in more detail.

3.1 Introduction

Classical controller design methods using Bode or Nyquist diagrams require the frequency response of the plant. More recent optimal control methods often require a plant model, usually in transfer function or state space form. It is therefore desirable to obtain a model of the plant for controller design purposes.

Phenomenological models of the vertical position response range from simple filament models ([Lazarus90] and [Jardin82]) to complex MHD models including 3d eddy current effects induced around port holes and also the surrounding tokamak structure. The problem with these methods is that they rely on simplistic assumptions and include parameters such as mutual inductances which can be difficult to determine, or entail the use of computer simulations which are difficult to setup. For the more complicated models, model reduction is often required, see [Portone94], [Tinios93] or [Al–Husari91].

A “black box” model can sometimes be obtained directly from experimental data using system identification. This is the approach taken in this project to obtain the plasma response. The resulting model is a linear, finite dimension, time invariant scalar model. The plasma forms part of an infinite dimensional system and the vertical position is coupled to radial position, and deformability of the plasma shape can be a concern especially in highly elongated plasmas ([Pomphrey89], [Ward92] and [Ward94]). On COMPASS–D the vertical position is always regulated about a fixed position and local linearization is used to justify the choice of finite dimensional and linear modelling. The system performance in the flattop period of the plasma is the main concern and parameters such as elongation (κ) change little; hence a time invariant model is justified. The vertical position is slightly coupled to the radial position, but the latter control loop is stable and operates on a much slower timescale so is not considered. The system identification techniques used on COMPASS–D are described in [Ljung87]. Their first use on plasma vertical position in tokamaks is described in [Lister90], where closed loop models were identified.

The open loop model was identified on COMPASS–D by exciting the position using an external reference signal (r_{FL} in the block diagram of Fig. 2.15) and measuring the control coil currents (u) and position signals (z_{FL} and z_{IPR}). Figure 3.1 shows the reference signal typically used for the experiments and the current and position responses. The response depends strongly on plasma attributes such as the shape, and the current profile. The main model obtained in this chapter and used in the following chapters is based on an SND L–mode plasma with elongation κ=1.6 and plasma current I_p=142kA. Other models based on different elongations and in SNT configuration have also been identified.

Note that the position signals are obtained either from an electrical integrator in the case of the FL position signal, or after numerical integration in the case of the IPR signal. The signals obtained directly from the sensor coils are velocity signals, and any model identified using the velocity would have a zero at the origin. It is more difficult to identify models with poles and zeros over a large range of magnitudes. Integrating the velocity cancels the zero and makes the overall system simpler to identify.

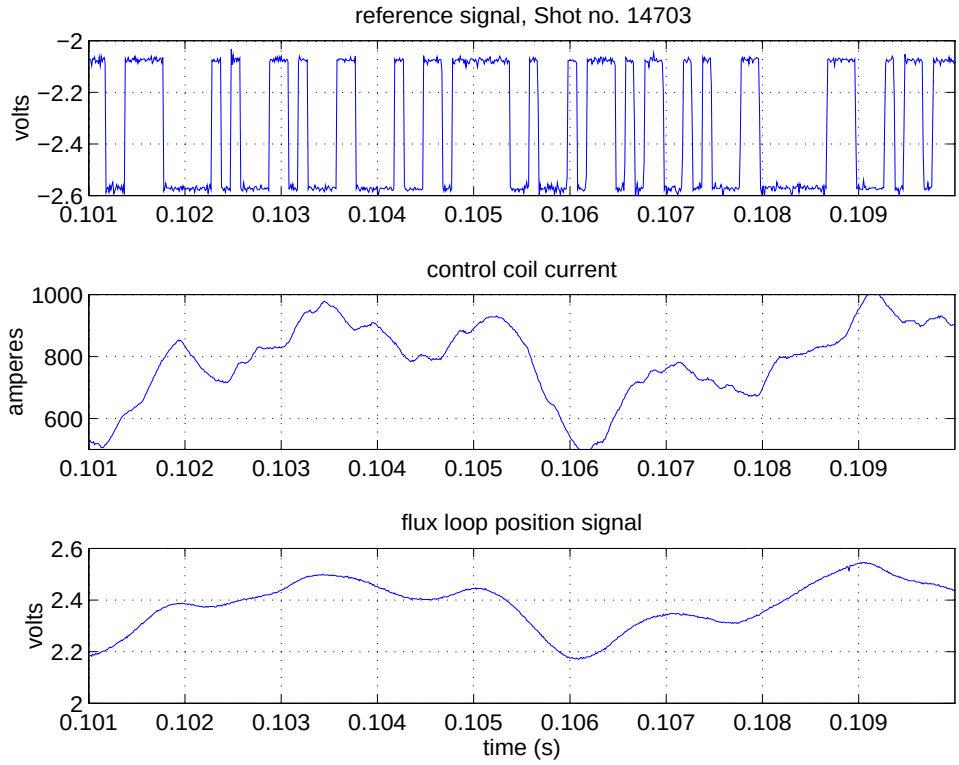


Figure 3.1 Random binary sequence reference position signal and amplifier current and FL position response.

The steps performed to produce the models are as follow:

1. Conduct plasma response experiments with RBS reference position signals during the flattop and data sampled at 100kHz.

2. Correct the time base of the data and then resample at 20kHz after antialias filtering.

3. Prefilter to remove 600Hz noise and emphasize the high frequency fit of model.

4. Remove the first 20 samples of data to remove transients from filtering.

5. Fit model coefficients to the input and output data using the least squares method.

6. Convert the model to continuous time or a frequency response plot as required.

An outline of the type of results obtained is briefly previewed in this section but they are described in more detail in later sections. The resulting models are discrete time, but to allow comparison with other models the results are presented in continuous

time. The value of a continuous time signal $v^c(t)$ at time $t=i\tau_s$ where τ_s is the sampling period is denoted v_i. The structure of the model obtained in this chapter is a difference equation

$$y_i = b_1 u_{i-1} + b_2 u_{i-2} - a_1 y_{i-1} - a_2 y_{i-2} - a_3 y_{i-3} \qquad \textbf{(3.1)}$$

where y represents the output (z_{FL} position in this case), u the input (control coil current) and coefficients a_i and b_i are determined by identification. Typical values for a standard plasma, with τ_s=50μs, are presented in Table 3.1. These parameters are used to calculate the frequency response and continuous time transfer function, and the variances are used to indicate confidence bounds associated with the frequency response. The level of bias of the estimated model is unknown but the system identification procedure is chosen to reduce any modelling bias.

Table 3.1 Discrete time model coefficients and estimated variances for an SND plasma, I_p=143kA, B_T=1.2T, κ=1.6 and FL position output signal (Shot no. 18001).

	a_1	a_2	a_3	b_1	b_2
value	-1.4587e0	8.3598e-2	3.2485e-1	-1.0686e-5	-3.5581e-5
variance	2.7294e-4	9.4663e-4	2.6893e-4	2.3468e-11	2.5960e-11

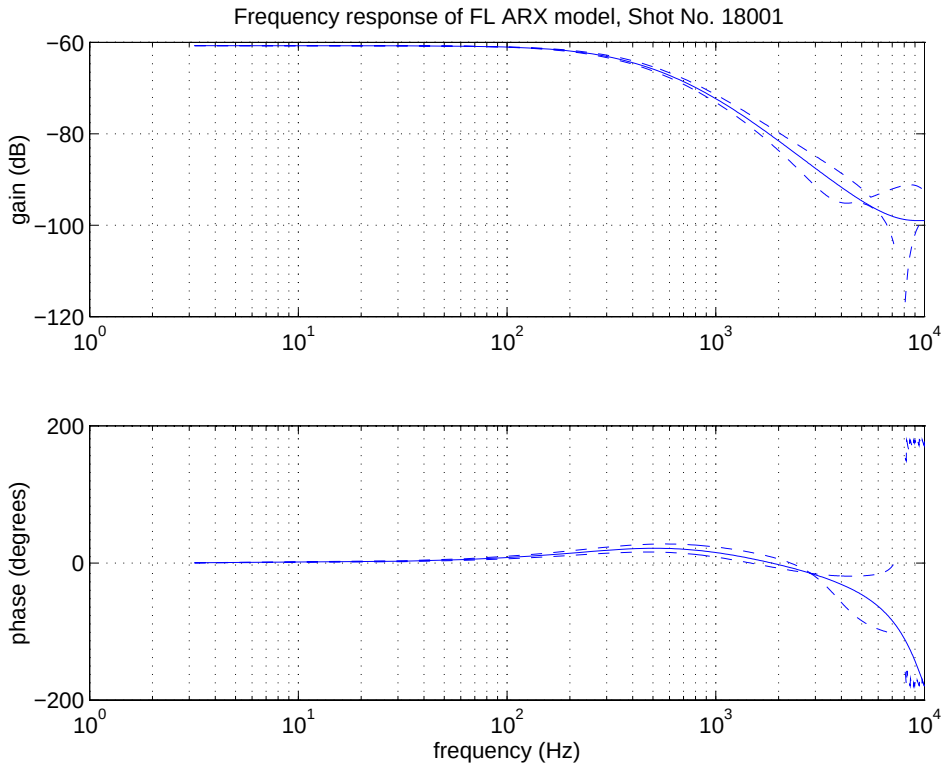
Defining the backward shift operator q^{-1}

$$q^{-1} v_i = v_{i-1}$$

allows the relationship between y and u to be written as

$$y_i = G(q^{-1}) u_i$$

where $G(q^{-1})$ is



(3.2)

Figure 3.2 Bode plot of plasma response.

The frequency response of the system is $G(e^{-j\omega_d})$ where ω_d is the discrete time frequency and $\omega_d=\pi$ rad/s represents the Nyquist frequency (half the sampling frequency). For a continuous time frequency ω_c, the equivalent discrete time frequency is $\omega_d \equiv \omega_c \tau_s$. The Bode plot in Fig. 3.2 shows the frequency response of the above model along with 95% confidence bounds. The discrete time transfer function is obtained using the Z–transform and is simply $G(z^{-1})$ where z is a complex variable. $G(z^{-1})$ is stable if and only if there are no poles of $G(z^{-1})$ outside the unit circle. The discrete time model can be converted to a continuous time transfer function ($G_c(s)$) by using the Tustin approximation ([Åström90])

$$G_c(s) = G(z^{-1})\Big|_{z=\frac{1+s\tau_s/2}{1-s\tau_s/2}}$$

where s is the Laplace transform variable. The resulting transfer function form of the plant model is

$$G_c(s) = K\frac{(s-z_1)(s-z_2)(s-z_3)}{(s-p_1)(s-p_2)(s-p_3)}$$

where z_i are the zeros and p_i are the poles of the system. In this case the model has two stable poles and one unstable pole with growth rate p_3=2451.1s^{-1}.

3.2 System identification method

The vertical position is unstable and so the system must be identified when operating in closed loop. It is not possible to use spectral analysis methods in a straight forward way because cause and effect are not easily separated. Identification methods which do not take into account the causal nature of the plant will not be successful [Ljung87, Section 14.2]. Predictor-error methods (PEM) can be used directly provided that a persistently exciting external signal is used [Söderström89 , Chapter 10]. The method chosen for identification of the COMPASS–D position response is the PEM technique applied directly to the input and output data [Vyas95]. Deconvolving from an identified closed loop model to find an open loop model (i.e. indirect identification) is also possible but numerically ill-conditioned because the closed loop sensitivity is small (i.e. feedback acts to reduce the effect of plant variations on the closed loop response). Other identification methods are available which can identify models with deterministic uncertainty bounds [Rubin93] but these methods are more complicated.

The basic idea behind PEM is that a model structure is chosen which allows future values of the system output to be predicted from past values, and then an optimization method is used to obtain model parameters which minimizes a norm of the prediction errors.

Suppose that the output y_i of a system is determined from a plant model $G_0(q^{-1})$ and a noise model $H_0(q^{-1})$, i.e.

$$y_i = G_0(q^{-1})u_i + H_0(q^{-1})e_i$$

where $\{e_i\}$ is a sequence of independent random variables with zero mean values and variances λ_0. For the plasma response the actual structure of G_0 and H_0 is unknown and may well be infinite order, nonlinear and time varying. Instead a model structure $G(q^{-1},\theta)$ and $H(q^{-1},\theta)$ is proposed which is thought to best approximate G_0 and H_0. The vector $\theta \in \mathbb{R}^d$ parameterizes the coefficients, and d is the total number of coefficients to determine in G and H. For the COMPASS–D model the structure of θ is

$$\theta = [a_1 \;\; a_2 \;\; a_3 \;\; b_1 \;\; b_2]^{\mathrm{T}}$$

with the model defined in (3.1). The parameterized system model $G(q^{-1},\theta)$ is defined in (3.2) and the noise model is

$$H(q^{-1},\theta) = \frac{1}{1 + a_1 q^{-1} + a_2 q^{-2} + a_3 q^{-3}}$$

The denominators of both G and H are common. The system identification procedure finds the coefficients parameterized by θ which best approximates the system in the model

$$y_i = G(q^{-1},\theta)u_i + H(q^{-1},\theta)e_i$$

Assuming y_r and u_r are known for $r \leq i-1$, then the one step ahead predictor is

$$\hat{y}_i(\theta) = W_u(q^{-1},\theta)u_i + W_y(q^{-1},\theta)y_i$$

where $W_y = 1 - H^{-1}$ and $W_u = H^{-1}G$. This allows the next output value to be predicted from previous values of input and output. The prediction error is defined as

$$\varepsilon_i(\theta) = y_i - \hat{y}_i(\theta).$$

The filters W_y and W_u form a predictor model if they are both stable. From [Ljung87, Definition 4.3], a model structure is a mapping from the parameter vector θ to the model set (in this case $G(q^{-1},\theta)$ and $H(q^{-1},\theta)$) such that each of the vector of filters $dW_u/d\theta$ and $dW_y/d\theta$ is stable. The gradients must be stable because they must be computed and used when searching for the model parameters. The choice of the model structure used for COMPASS–D is described below. A quadratic norm is often a standard choice for representing the size of the predictions errors and is convenient for computation and analysis [Ljung87, Section 7.2]. The norm of the prediction error (V) is then

$$V(\theta) \triangleq \frac{1}{n}\sum_{i=1}^{n} \varepsilon_i^2 \qquad \textbf{(3.3)}$$

where n is the number of predictions from the sampled data. The parameter vector θ is chosen such that

$$\hat{\theta} = \arg\min_{\theta} V(\theta)$$

For open loop operation (and other minor conditions) of the system, Parseval's theorem can be used to express the prediction error as [Ljung87, Section 8.5]

$$V(\theta) = \frac{1}{2\pi}\int_{-\pi}^{\pi} [|G_0(e^{-j\omega}) - G(e^{-j\omega},\theta)|^2 \Phi_u(\omega) + \Phi_v(\omega)] \frac{1}{|H(e^{-j\omega},\theta)|^2} d\omega \qquad \textbf{(3.4)}$$

Here $\Phi_v = \lambda_0 |H_0(e^{-j\omega})|^2$ is the noise spectral density and Φ_u is the input signal spectral density. It can be seen that the cost is approximately the sum of a frequency weighted error between G and G_0 and an additional term involving the noise model. The frequency weight of the fit of $G(e^{-j\omega},\theta)$ to $G_0(e^{-j\omega})$ is $\Phi_u/|H(e^{-j\omega},\theta)|^2$ which can be interpreted as a signal to noise ratio. The expression applies only for open loop systems but is used below to provide heuristic justification for some model choices.

3.3 Model structure

The choice of the ARX model is explained in this section. The model is identified using the least squares algorithm, which is also described, and bias and variance properties of the model are discussed.

A range of possible linear model structures can be described [Ljung87, Chapter 4] as

$$A(q^{-1})y_i = \frac{B(q^{-1})}{F(q^{-1})}u_i + \frac{C(q^{-1})}{D(q^{-1})}e_i \qquad \textbf{(3.5)}$$

where *A, B, C, D* and *F* are polynomials in q^{-1}. Model structures in common use such as ARX use only *A* and *B* ($Ay_i=Bu_i+e_i$), or Box-Jenkins *B,F,C* and *D* ($y_i=B/Fu_i+C/De_i$), but other combinations are possible. The predictor model obtained from (3.5) is

$$\hat{y}_i(\theta) = \frac{D(q^{-1})B(q^{-1})}{C(q^{-1})F(q^{-1})}u_i + \left[1 - \frac{D(q^{-1})A(q^{-1})}{C(q^{-1})}\right] y_i$$

The ARX model has a common denominator (*A*) for both the system (*G*) and the noise (*H*) dynamics. Since there is no a priori information to suggest that *G* and *H* have common poles it may be preferred to use a model which parameterizes *G* and *H* independently. However the plant contains an unstable pole which must be identified in either *A* or *F*. If it is included in *F* then the predictor model will be unstable, so an autoregressive term (*A*) must be used in the model identification. This precludes the use of the commonly used output error model structure ($y_i=B/Fu_i+e_i$) since an unstable pole in *F* causes the predictor model to be unstable. The simplest autoregressive model is the ARX model. Other possible models are ARMAX ($Ay_i=Bu_i+Ce_i$) etc. A useful advantage of using ARX models is that the model coefficients can be found easily using linear regression.

The predictor for an ARX model can be written in the form

$$\hat{y}_i(\theta) = \boldsymbol{x}_i^{\mathrm{T}}\theta \qquad \textbf{(3.6)}$$

where $\boldsymbol{x}_i \in \mathbb{R}^d$ is a vector containing the previous input and output samples. For the model in (3.1) $\boldsymbol{x}_i^{\mathrm{T}} = \begin{bmatrix} u_{i-1} & u_{i-2} & y_{i-1} & y_{i-2} & y_{i-3} \end{bmatrix}$. Given enough samples to form n predictions, (3.6) can be stacked to form the equation $\hat{\boldsymbol{Y}} = \boldsymbol{X}\theta$, $\hat{\boldsymbol{Y}} \in \mathbb{R}^n$ and $\boldsymbol{X} \in \mathbb{R}^{n \times d}$ where

$$\hat{\boldsymbol{Y}} = \begin{bmatrix} \hat{y}_1 \\ \hat{y}_2 \\ \vdots \\ \hat{y}_n \end{bmatrix}, \text{ and } \boldsymbol{X} = \begin{bmatrix} \boldsymbol{x}_1^{\mathrm{T}} \\ \boldsymbol{x}_2^{\mathrm{T}} \\ \vdots \\ \boldsymbol{x}_n^{\mathrm{T}} \end{bmatrix}.$$

If the measured output samples are stacked in a vector $\boldsymbol{Y}$ then a vector of residuals $\boldsymbol{\varepsilon} \in \mathbb{R}^n$ can be formed

$$\boldsymbol{\varepsilon} = \boldsymbol{Y} - \hat{\boldsymbol{Y}}, \ \boldsymbol{Y} = \begin{bmatrix} y_1 & y_2 & \cdots & y_n \end{bmatrix}^{\mathrm{T}}.$$

The cost function $V = \boldsymbol{\varepsilon}^{\mathrm{T}}\boldsymbol{\varepsilon}/n$ can be rewritten as

$$V = (\boldsymbol{Y} - \boldsymbol{X}\theta)^{\mathrm{T}}(\boldsymbol{Y} - \boldsymbol{X}\theta)/n$$

and the vector of parameters $(\hat{\theta})$ minimizing the cost can be found analytically to be

$$\hat{\theta} = (\boldsymbol{X}^{\mathrm{T}}\boldsymbol{X})^{-1}\boldsymbol{X}^{\mathrm{T}}\boldsymbol{Y}. \qquad \textbf{(3.7)}$$

It is assumed that the matrix $\boldsymbol{X}^{\mathrm{T}}\boldsymbol{X}$ is nonsingular which is equivalent to requiring a persistently exciting input signal.

Results on the bias and variance of the model parameters $(\hat{\theta})$ can be obtained by assuming that the true system can be modelled as

$$\boldsymbol{Y} = \boldsymbol{X}\theta_{\boldsymbol{0}} + \boldsymbol{e}, \ \boldsymbol{e} = \begin{bmatrix} e_1 & e_2 & \cdots & e_n \end{bmatrix}^{\mathrm{T}} \in \mathbb{R}^n. \qquad \textbf{(3.8)}$$

Substituting (3.8) into (3.7) allows an expression for the bias

$$E(\hat{\theta}-\theta_0)=E(\boldsymbol{X}^T\boldsymbol{X})^{-1}\boldsymbol{X}^{\mathrm{T}}\boldsymbol{e}$$

The symbol *E* represents the expectation operator. It can be shown [Wellstead91, Section 3.2] that the model is unbiassed if the probability that $n^{-1}\boldsymbol{X}^{\mathrm{T}}\boldsymbol{e}>0$ tends to zero as *n* tend to infinity. The quantity $n^{-1}\boldsymbol{X}^{\mathrm{T}}\boldsymbol{e}$ is the cross correlation between the data and noise sequences. Therefore uncorrelated (or asymptotically uncorrelated) noise and data is necessary for unbiassed estimates. The covariance $(\boldsymbol{P}\in\mathbb{R}^{d\times d})$ defined as

$$\boldsymbol{P}=E\left[(\hat{\theta}-\theta_0)(\hat{\theta}-\theta_0)^{\mathrm{T}}\right]$$

can be calculated from

$$\boldsymbol{P}=\lambda_0 E_x\left[(\boldsymbol{X}^{\mathrm{T}}\boldsymbol{X})^{-1}\right]$$

Small covariances require $(\boldsymbol{X}^{\mathrm{T}}\boldsymbol{X})^{-1}$ to be small and therefore large *n*. An unbiassed estimate of λ_0 can be obtained from

$$\hat{\lambda}=\frac{1}{n-d}\varepsilon^{\mathrm{T}}\varepsilon,\ d=dim(\theta)$$

The covariance is then estimated from

$$\hat{\boldsymbol{P}}=\hat{\lambda}(\boldsymbol{X}^T\boldsymbol{X})^{-1} \qquad \textbf{(3.9)}$$

It is often useful to obtain an indication of the variance of the frequency response of the model. This can be approximated by assuming a linear relationship between the frequency response and the parameter vector. A first term Taylor approximation is often used to establish this relationship [Amin88]. Defining the vector $\boldsymbol{g}(\omega)$ as the real and imaginary part of the frequency response of the model

$$\boldsymbol{g}\triangleq\begin{bmatrix}\Re G(e^{-j\omega},\theta)\\ \Im G(e^{-j\omega},\theta)\end{bmatrix}$$

and defining $\tilde{\theta} \triangleq \theta - \hat{\theta}$ and $\tilde{\boldsymbol{g}} \triangleq \boldsymbol{g} - \hat{\boldsymbol{g}}$ allows the frequency response to be calculated

$$\tilde{\boldsymbol{g}} \approx \begin{bmatrix} \Re d\hat{G}/d\theta \\ \Im d\hat{G}/d\theta \end{bmatrix} \tilde{\theta}$$

or $\tilde{\boldsymbol{g}} \approx \Gamma\tilde{\theta}$ where

$$\Gamma \triangleq \begin{bmatrix} \Re d\hat{G}/d\theta \\ \Im d\hat{G}/d\theta \end{bmatrix} = \begin{bmatrix} \Re\dfrac{\partial \hat{G}}{\partial \theta_1} & \Re\dfrac{\partial \hat{G}}{\partial \theta_2} & \cdots & \Re\dfrac{\partial \hat{G}}{\partial \theta_d} \\ \Im\dfrac{\partial \hat{G}}{\partial \theta_1} & \Im\dfrac{\partial \hat{G}}{\partial \theta_2} & \cdots & \Im\dfrac{\partial \hat{G}}{\partial \theta_d} \end{bmatrix}$$

Assuming $\tilde{\theta}$ is distributed normally with zero mean and covariance $\boldsymbol{P}$ then $\tilde{\boldsymbol{g}}$ is distributed normally with zero mean and covariance $\Gamma^T \boldsymbol{P} \Gamma$. Note that the quantity $\tilde{\boldsymbol{g}}^T(\Gamma \boldsymbol{P} \Gamma^T)^{-1}\tilde{\boldsymbol{g}}$ has a χ^2 distribution with two degrees of freedom [Mardia79, Section 2.5].

The results can be used to plot confidence bounds of the variance on the frequency responses of the identified models. Ellipses are drawn on the Nyquist plot in Fig. 3.3 representing the 95% confidence level. At a given frequency ω the frequency response of the model is the complex value $\hat{G}(e^{-j\omega})$ or the vector $\hat{\boldsymbol{g}}(\omega)$. This value is not drawn in the plot but is represented by the centre of each ellipse. The points on each ellipse mark the values $\hat{\boldsymbol{g}} + \tilde{\boldsymbol{g}}$ at a given frequency, where $\tilde{\boldsymbol{g}}$ is the set of values which satisfy

$$\tilde{\boldsymbol{g}}^T(\Gamma \hat{\boldsymbol{P}} \Gamma^T)^{-1}\tilde{\boldsymbol{g}} = \mu_{95}$$

The coefficient μ_{95}=5.99 represents the 95% confidence level of a χ^2 random variable with two degrees of freedom. The approximation $\hat{\boldsymbol{P}}(3.9)$ is used for the parameter covariance, but the χ^2 approximation still holds because of the large number of predictions (n>3000) used in the identification [Cloud86].

The results in Fig. 3.3 show that the length of the ellipses (along the longest axis) increases with frequency from DC to 400Hz. The ellipses then become smaller

reaching a minimum at 5kHz before the plot rapidly approaches the origin. The Bode plot in Fig. 3.2 shows the effect of the ellipses on the minimum and maximum estimate of amplitude and phase at each frequency. The kink at 5kHz is clearly observed on the diagram.

The above analysis of confidence bounds for ARX models depends on a linear approximation between parameter vector and θ frequency response. A concern with the ARX variance estimates is that the Taylor approximation used above may not be valid. The ARX model is therefore compared with an FIR model, which has the advantage that the frequency response is linearly related to the parameter vector. FIR models do not require an approximation for calculation of the frequency domain confidence bounds. Open loop unstable plants can be modelled as bicausal FIR model [Kouvaritakis92a]. The coefficients (g_j) in the model

$$y_i = \sum_{j=-q_m}^{q_p} g_j u_{i-j} + \zeta_i$$

are found from a least squares fit and ζ represents the measurement noise. The coefficients are plotted in Fig. 3.4. Both the ARX and the FIR model (with q_m=q_p=25) have similar frequency responses and the confidence bounds overlap above 200Hz. The fact that the bounds do not overlap below 200Hz is an indication of bias in the models. Below 1kHz the ARX model has more conservative (larger) confidence bounds. Above 1kHz the absolute radius of the uncertainty ellipses (Fig. 3.5) increases with frequency in the FIR model but decreases in the ARX model.

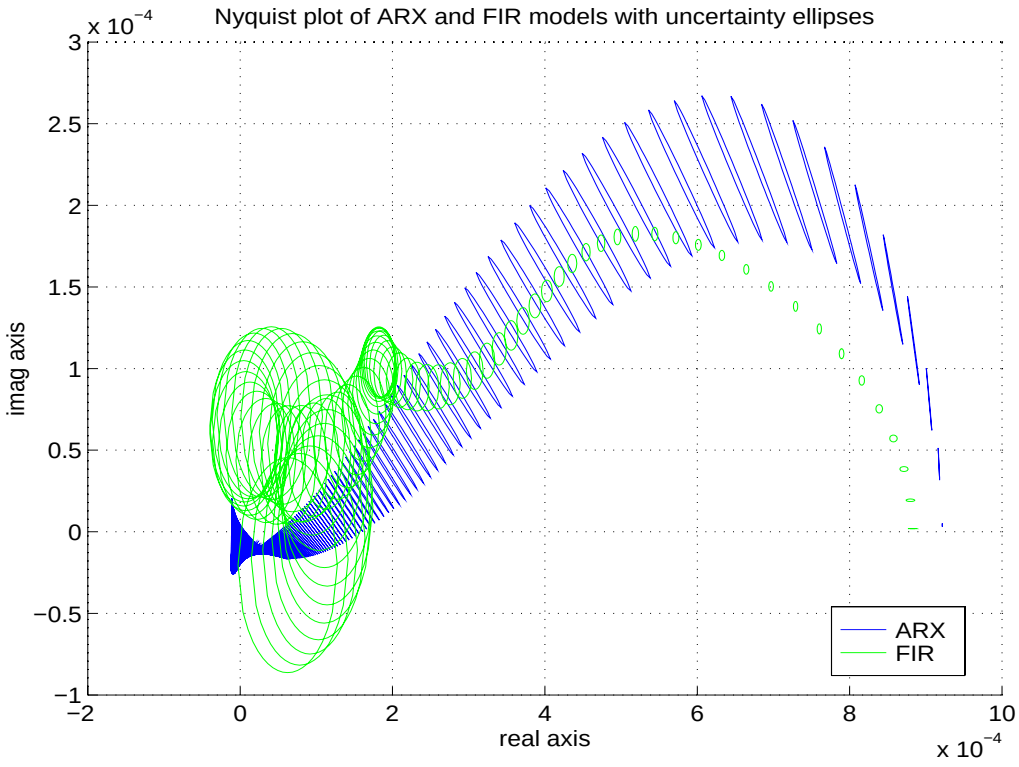


Figure 3.3 Nyquist plot with 95% confidence bounds.

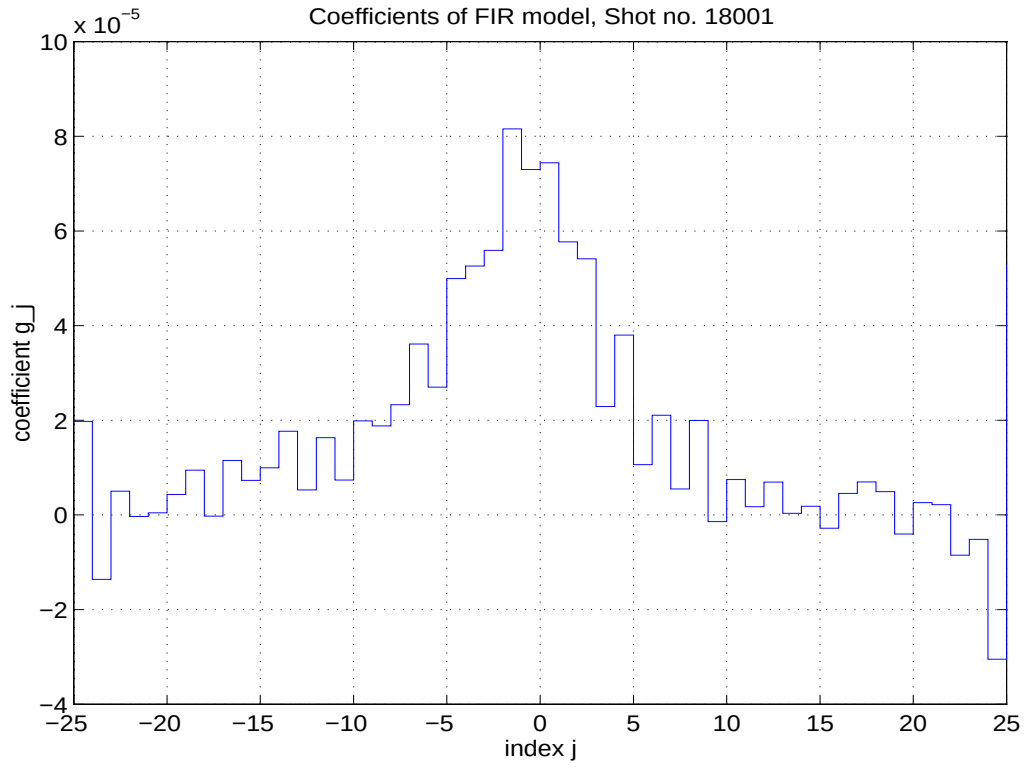


Figure 3.4 FIR model coefficients.

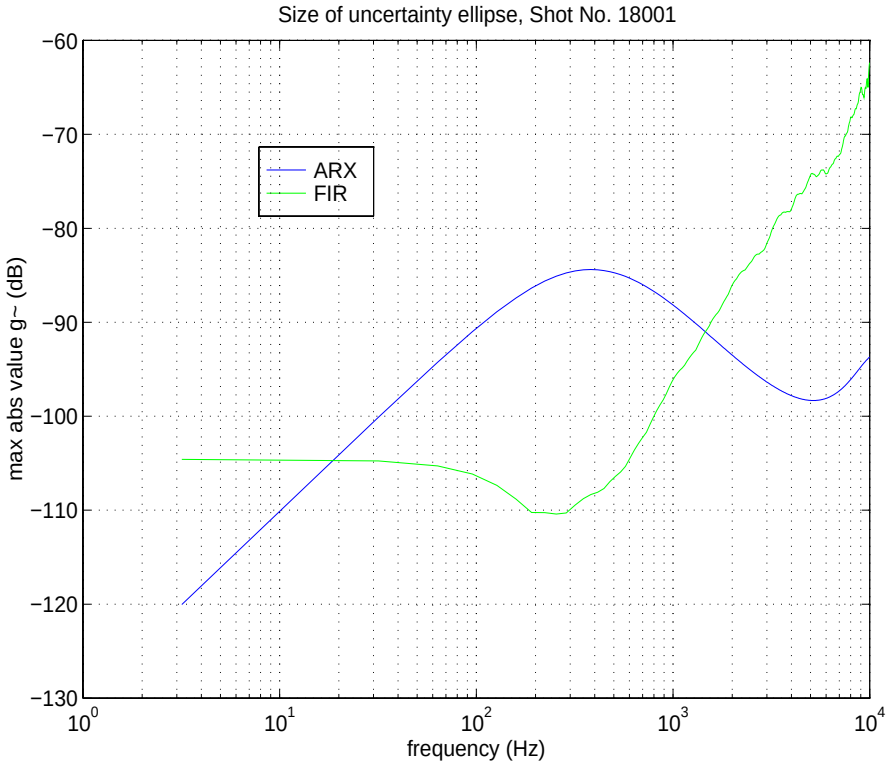


Figure 3.5 Size of 95% confidence ellipse against frequency.

3.4 Signal analysis

As stated earlier a persistently exciting input is required to excite the modes of the plasma response and to enable the model to be identified. The matrix $\boldsymbol{X}^{\mathrm{T}}\boldsymbol{X}$ in (3.7) must be nonsingular, which is satisfied if the columns of $\boldsymbol{X}$ are linearly independent. This may not be true if the system operates in feedback because of the dependence of input signals on past value of the output. Introducing an external reference signal ensures that the matrix $\boldsymbol{X}^{\mathrm{T}}\boldsymbol{X}$ is nonsingular. If the reference signal causes the columns of $\boldsymbol{X}$ to be uncorrelated with the noise then the model is unbiassed.

The signal chosen to provide excitation was a random binary sequence perturbing the position reference r_{FL} (Fig. 2.11). The signal switches between two levels at random at 100μs intervals. For the shot in Fig. 3.1 the reference signal switches between −2.1V and −2.6V. The standard reference signal is typically constant at -2.29V. The resulting waveform has a large variance ($0.25V^2$) intended to provide a large signal to noise ratio over a wide range of frequencies. The reference frequency spectrum (Fig. 3.6) shows that the spectrum contains components up to at least 3kHz and includes lobes at intervals of 10kHz due to the switching frequency. The peak to peak variation in the position signals are ~0.6V for the FL signal and ~2V for the IPR signal corresponding to a peak to peak variation in position of ~1cm. The signal variances are $0.0112V^2$ for

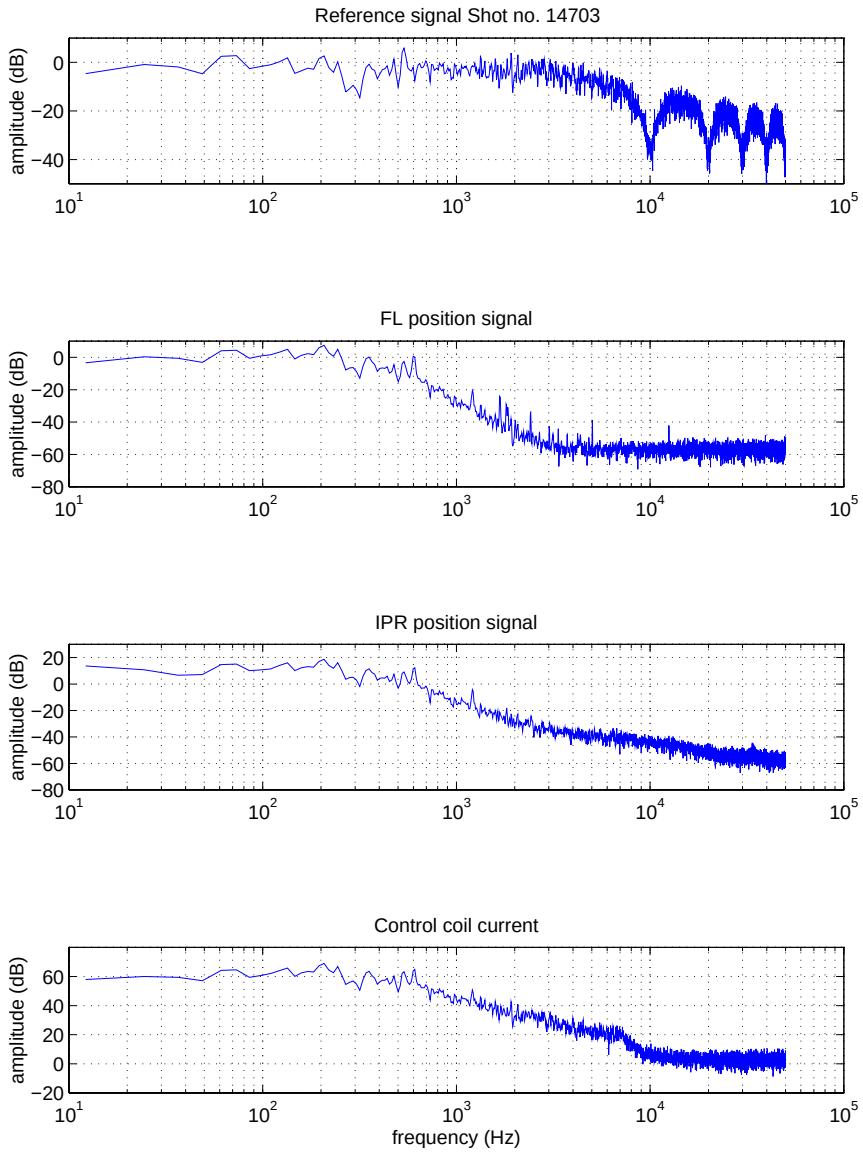


Figure 3.6 Frequency spectra of reference and input/output data shot no. 14703.

the FL signal, $0.155V^2$ for the IPR signal and $3.35\times10^{-6}m^2$ for a position signal obtained from DFIT reconstructions. The position signals and current spectra all start to roll off above 700Hz. The resulting current signal spectrum depends on the L/R time of the control coils which is relatively large compared with the plasma instability growth time and so it is important to ensure the signal amplitude is large at high frequencies. A binary signal allows for a large variance without saturating the power amplifiers. The spectrum of the FL signal (shown in more detail in Fig. 3.7) contains peaks at 600Hz and higher harmonics, and also a peak at 1675Hz which is not clearly present in the other signals. The 1675Hz component is unintentional pickup present only in a small range of plasma shots.

The data was sampled during the flat top period at 100kHz for 160ms and then resampled at 20kHz. Antialiasing filters are used to reduce the frequency components above 10kHz. The control coil current signal is transmitted through an optical link before being sampled. The link has a 10kHz 3dB bandwidth with two pole roll off, and so therefore acts as an antialiasing filter. The position signals are antialiased in software by a filter with the same characteristics as the optical link.

Resampling to a lower sampling frequency improves the numerical conditioning of the model fitting procedure. A fast sampling rate would make the rows of $\boldsymbol{X}$ similar leading to rank deficient $\boldsymbol{X}^{\mathrm{T}}\boldsymbol{X}$. Very fast sampling rates result in large model orders, high order delays, and poles clustered around unity. At 20kHz the sampling frequency is more than 50 times the open loop bandwidth and 10 times the closed loop bandwidth and so is fast enough to capture the important dynamics.

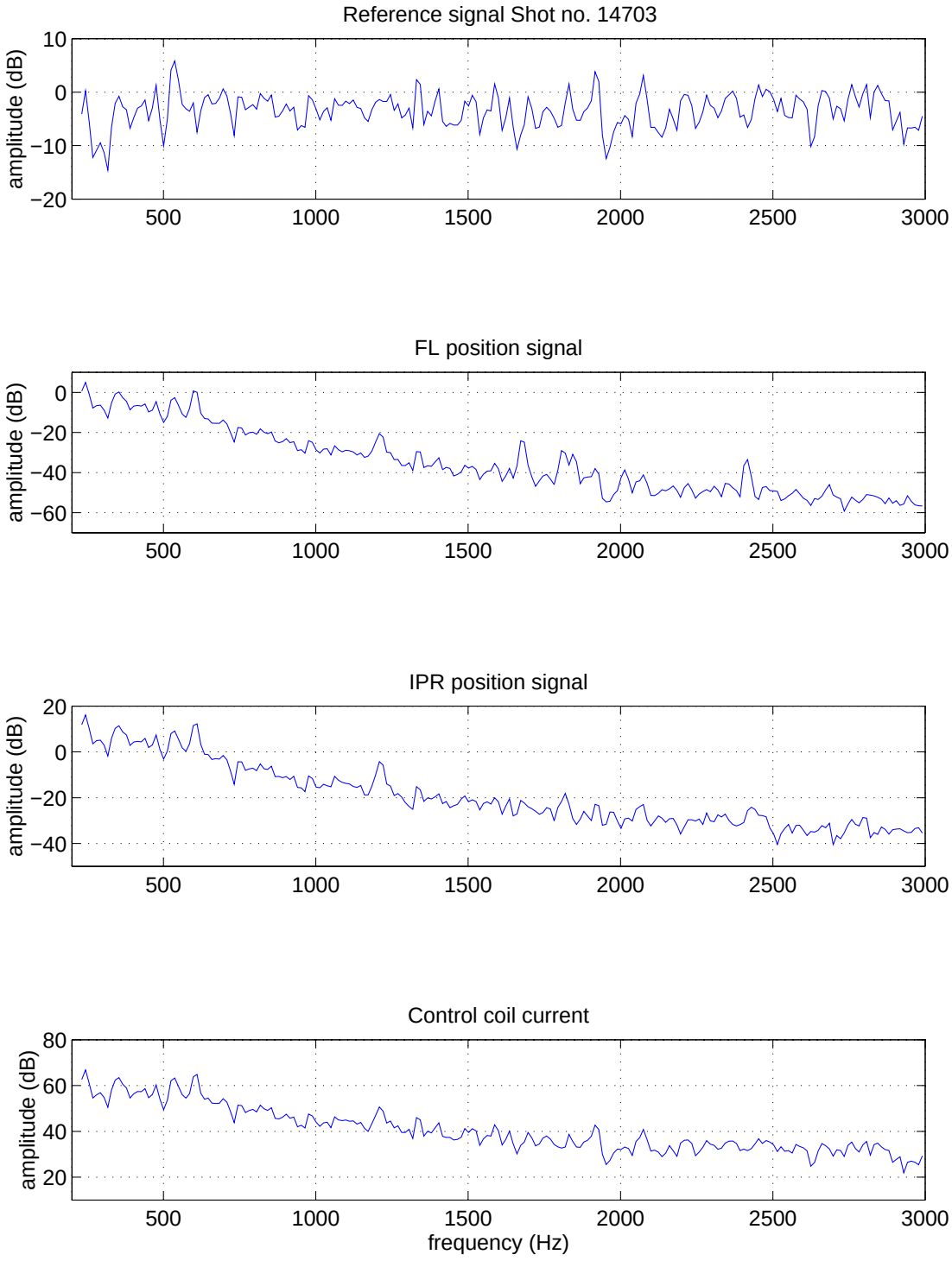


Figure 3.7 Detail of spectra for shot no. 14703.

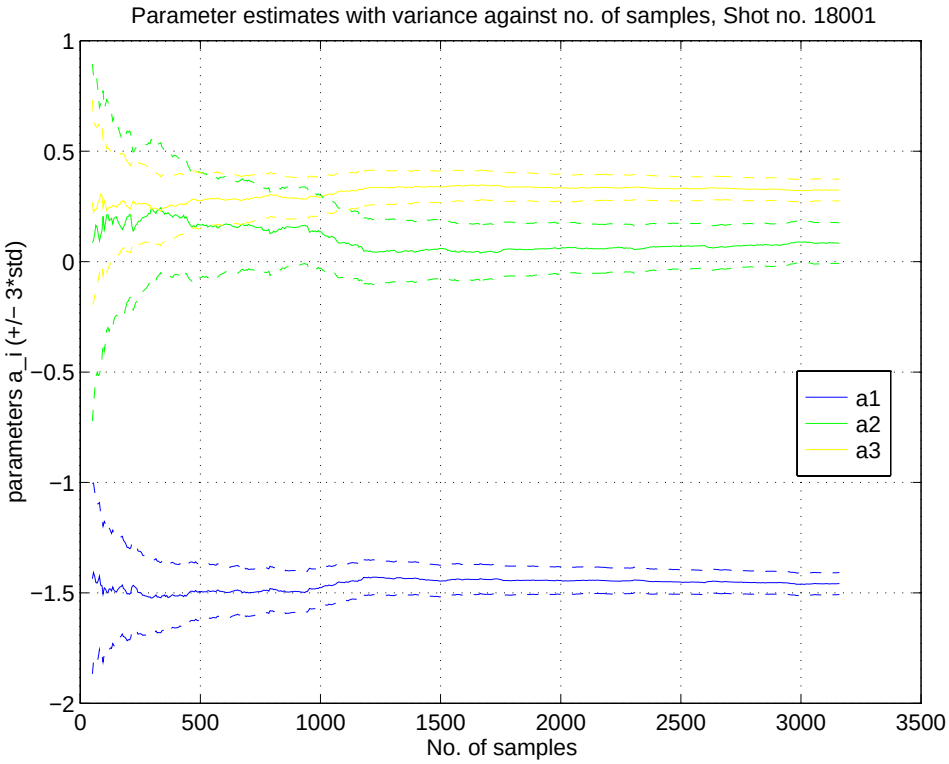


Figure 3.8 Effect of increasing no. of samples on estimates (a_1, a_2 and a_3) and ±3 standard deviations.

The quantity of data taken (160ms) was limited mainly by the length of the flattop period of a typical plasma shot. However it proved to be adequate as seen in Fig. 3.8. The plot shows the parameter estimates and variances as the number of samples used to estimate the model is increased. The variances are estimated from the diagonal of the covariance matrix (3.9). The variances rapidly converge towards 500 samples and very little change in parameter estimate or variance occurs above 1500 samples.

3.5 Prefiltering of data

As indicated earlier from open loop results (3.4) the model fit is weighted in the frequency domain by the signal to noise ratio of the system. The model will be closer to the actual system at the emphasized frequencies. Changing the weight can change the frequency range which is emphasized and therefore affect the bias of the estimate. The result assumes that the data is not obtained from closed loop but heuristically a similar relationship between signal to noise ratio and model fit is expected. In theory prefiltering the data can alter the frequency weighting and can therefore be used to

reduce the bias at frequencies of interest. The use of prefiltering is examined in this section.

The experimental input and output signals have a large 600Hz component, and the coil current signal has poor high frequency components because of its large L/R time constant. The data is prefiltered to remove the 600Hz noise and improve the high frequency fit. Prefiltering the data such that $u^F=L(q^{-1})u$ and $y^F=L(q^{-1})y$ where $L(q^{-1})$ represents the filter transfer function results in the model

$$y_i^F = Gu_i^F + He_i$$

Here G and H are assumed to be obtained from identification of the filtered data. This implies that for the original data

$$y_i = Gu_i + \frac{H}{L}e_i$$

Prefiltering the data effectively changes the noise model from H to H/L. If L is a 600Hz notch filter then the noise model H/L has a peak at 600Hz. Similarly making L a high pass filter results in a noise model with large low frequency components, reducing the low frequency weighting in the model fit.

Figure 3.9 shows the effect of 600Hz notch filtering on the autocorrelation of the residuals from the FL model. The filter is second order and has more than 3dB attenuation in the range 580 to 620Hz. The peaks in the figure at intervals of 33 samples correspond to 600Hz. Prefiltering with the 600Hz notch improves the whiteness of the residuals since it is less dominated by the 600Hz component. The next largest component is at 1675Hz. This was detected more clearly by examining frequency spectra of the residuals. Note that using a 1675Hz notch in addition to the 600Hz notch makes less of a difference. The IPR residuals (Fig. 3.10) are less dominated by the 600Hz and 1675Hz components. Filtering the components leaves a small level of autocorrelation.

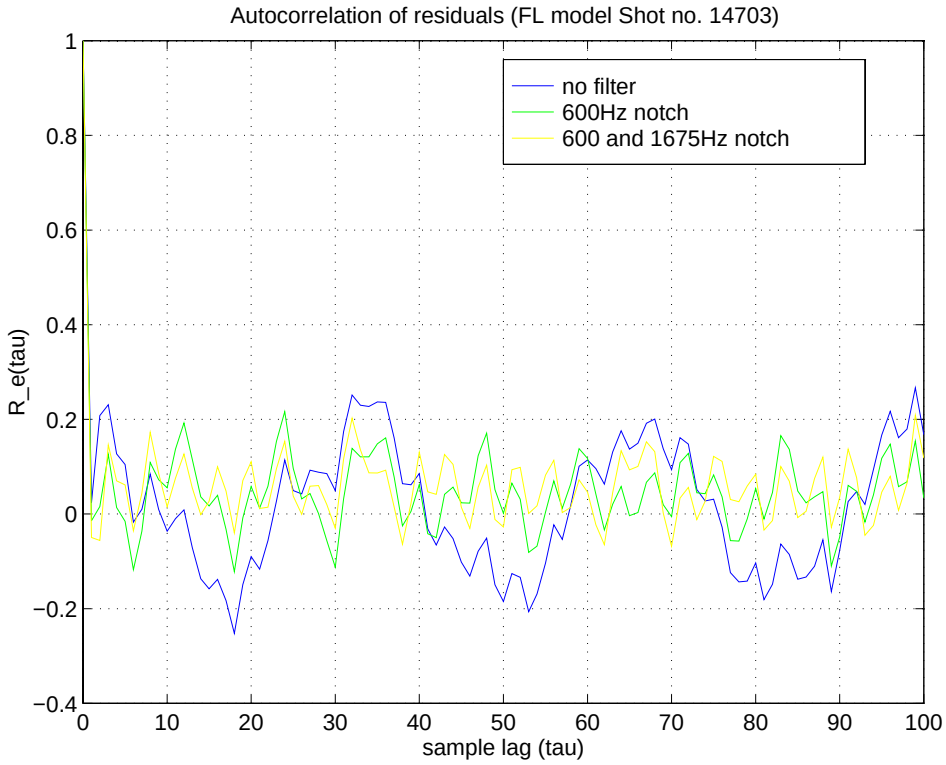


Figure 3.9 Autocorrelation of residuals for FL model.

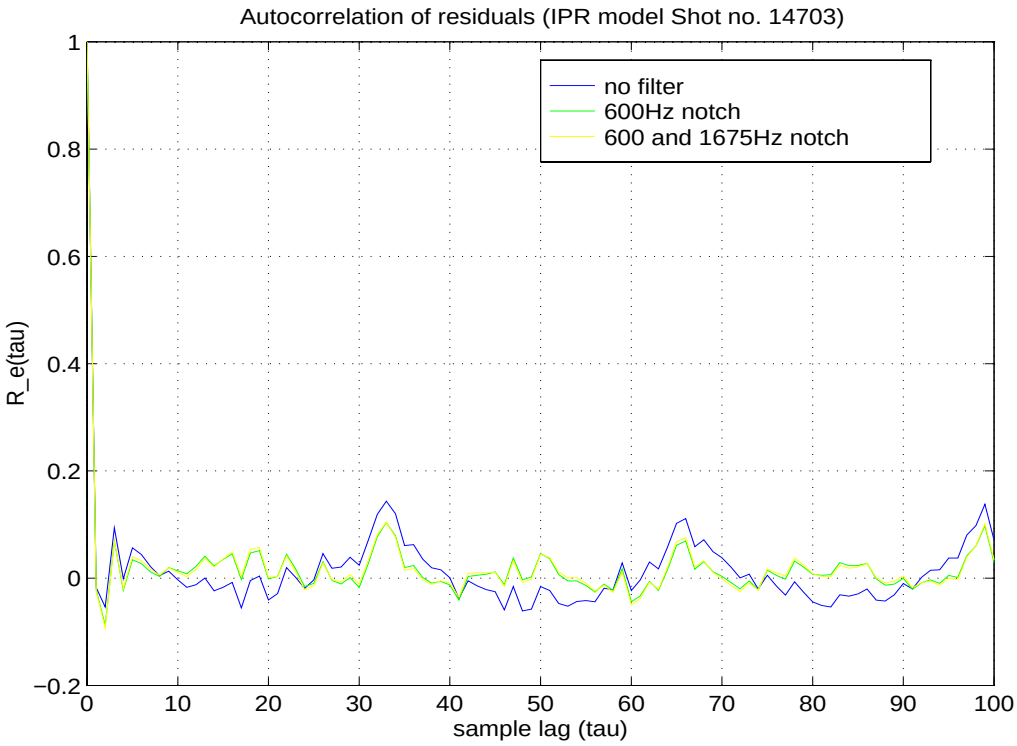


Figure 3.10 Autocorrelation of residuals for IPR model.

At high frequencies the absolute error of $|G_0-G|$ is small because G is small. The input spectral density is also low at high frequencies and this would suggest that the model fit at high frequencies is relatively poor compared to low frequencies. However the noise model $H=1/A$ is low pass and emphasizes the high frequencies. Introducing a high pass prefilter so that $H=1/LA$ further improves the high pass fit. The effect of high pass filtering with first order filters with cutoff frequencies in the range 20Hz to 500Hz was examined. High pass filtering made very little difference to the Bode plots of the FL models. Applying a 600Hz notch to the input and output data changed the frequency response by up to 0.5dB below 1kHz and up to 4dB above 5kHz. Additional notch filtering to remove the 1675 and other components and high pass filtering caused very little extra change from 600Hz only notch filtering. The effect of high pass filtering can be seen more clearly for IPR models (Fig. 3.11). The frequency response changes by up to 0.5dB if a 600Hz notch is used, with very little extra change (<0.1dB) for additional notch filtering. Using a 100Hz high pass filter with the 600Hz notch causes a bigger change up to 2dB. As for the FL model the cutoff frequency of the high pass filter is unimportant in the range 20 to 500Hz.

Assessing the implications from this section is difficult. Small changes in the frequency responses of the models occur if the data is prefiltered. Notch filtering at 600Hz is justified on the grounds that this improves the whiteness of the residual autocorrelation and that this matches the assumptions of the model more closely. For both FL and IPR models the effect is to produce small changes in the frequency response of the order of 1dB. The change in bias is larger than the variance 95% confidence level of the frequency responses below ~500Hz (Fig. 3.2) but well within the confidence level above ~2kHz. Further notch filtering to remove harmonics and 1675Hz had little effect. High pass filtering is used on the grounds that the model is weighted at low frequencies because of the 19.2Hz bandwidth of the control coils. It also reduces the effect of low frequency drift and disturbances. The effect on the FL model is minimal but the IPR model is changed by a small amount. The results that follow in this thesis are obtained from data prefiltered by the 600Hz notch and the 100Hz high pass filter. Whether this has reduced the bias of the model is unclear. Most of the results following in this thesis are derived from the FL model and so the effect of the high pass filter is not of great importance.

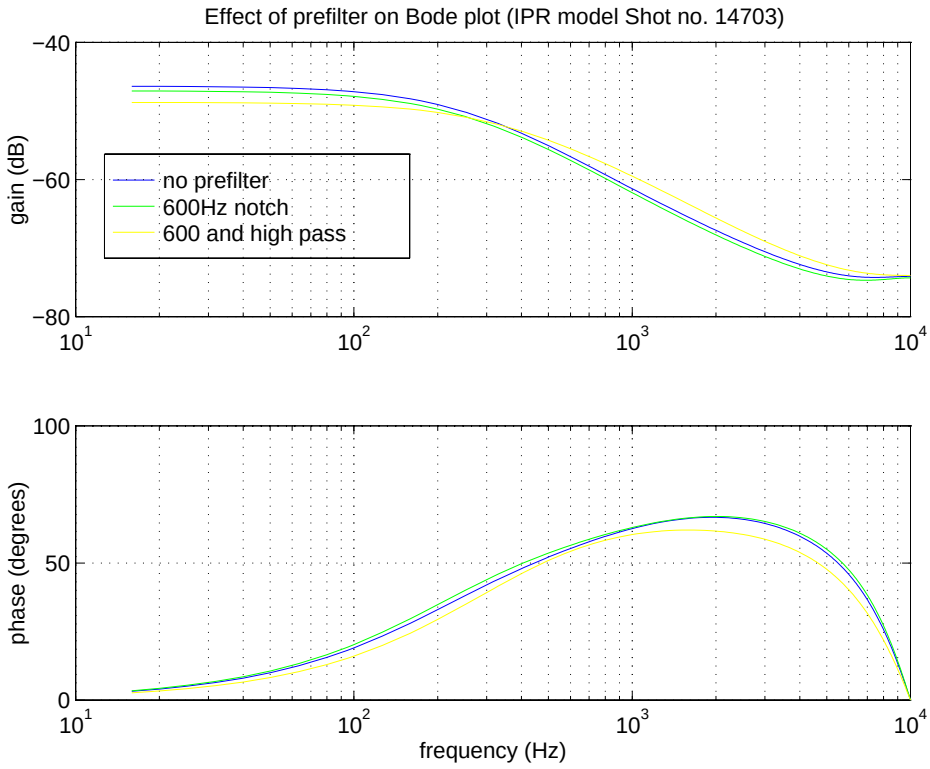


Figure 3.11 Effect of high pass prefilter on model frequency response.

3.6 Model order

The model order was selected by comparing models which have different numbers of parameters in the polynomials *A* and *B*. Cross–validation is often used to compare models. Cross–validation means that the models are calculated from an identification set of data, and then evaluated by comparing results from simulated and measured responses from a separate test set of data. Open loop simulations are not possible for the vertical position models because they are unstable. Instead the mean square error of the residuals (3.3) is used as a basis for comparing models. A lower cost indicates a closer fit to the data and hypothetically a closer fit to the actual system dynamics. In general higher order models tend to produce smaller values of residual costs but also generate estimates with larger variances and tend to fit the noise characteristics of the system rather than the system dynamics. Formal methods exist for the selection of model order. These are often based on cost criteria involving functions of the residual error and the number of model parameters, see [Freeman85] and [Akaike74]. A large number of samples (>3000) are available for estimating the models and so the variance of the estimates are relatively small and less of a concern when selecting the

model order. In this section the model is selected in a heuristic manner by examining plots of the residual cost against model order and examining Bode plots of different models.

The plot in Fig. 3.12 shows on a logarithmic scale the residual cost (V) of models with different orders. The number of parameters identified in the polynomials *A* and *B* are n_a and n_b respectively. A significant improvement in cost is observed at fixed n_b when n_a is increased from 1 to 2, but there is much less of an improvement as n_a increases beyond 2. There is also very little variation of cost with n_b for any $n_a \geq 2$. This suggests that any model with $n_a \geq 2$ will have a small residual cost. The Bode plot in Fig. 3.13 show the frequency responses of different models clustered around the n_a=3 and n_b=2 model. Low order models (n_a=1, n_b=1, and n_a=2 ,n_b=2) deviate from the cluster above 1kHz. This suggests that too low an order results in a large bias. The higher order models (n_a=5 and n_a=10) exhibit complex dynamics above 1kHz but with the response centred around the n_a=3 model. The variance of the frequency response is relatively high at high frequencies (Fig. 3.2) and so the behaviour of the high order models may be due to poor variance or fitting to noise. The model order selected for analysis in the rest of this thesis is n_a=3, n_b=2. This represents the best compromise between residual cost, bias and variance.

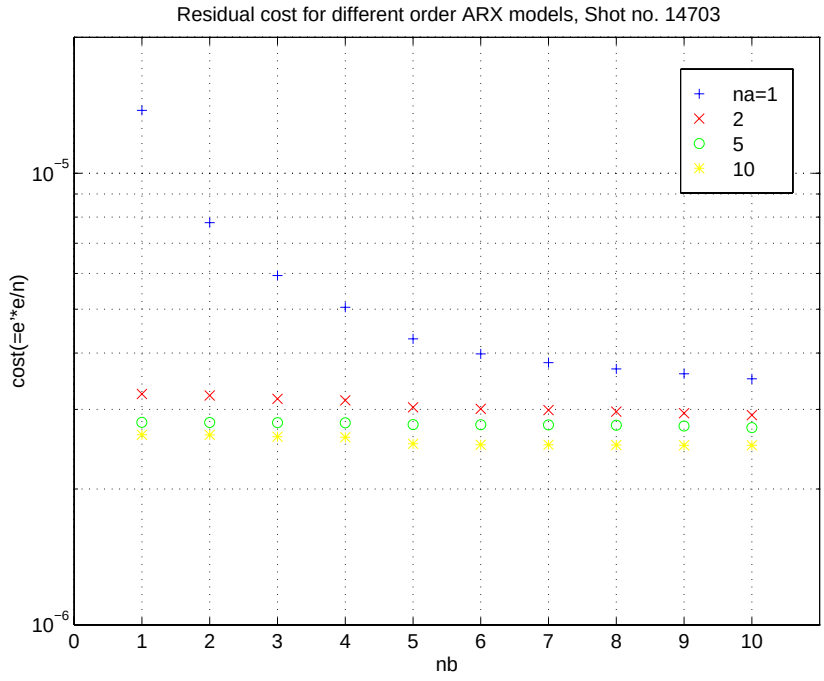


Figure 3.12 Residual cost for different model orders.

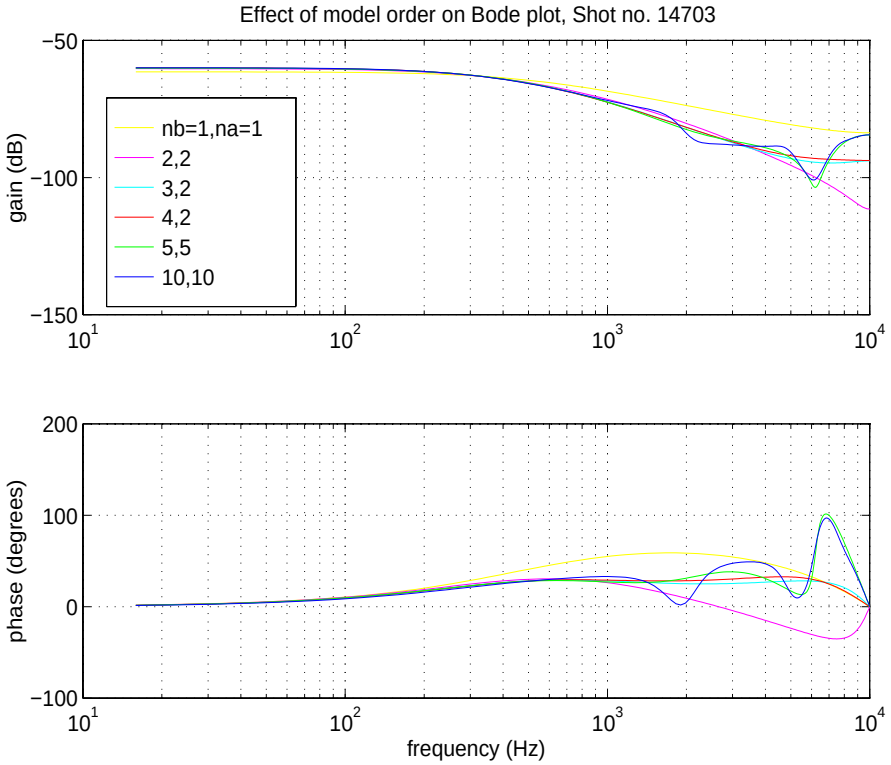


Figure 3.13 Effect of model order on Bode plots.

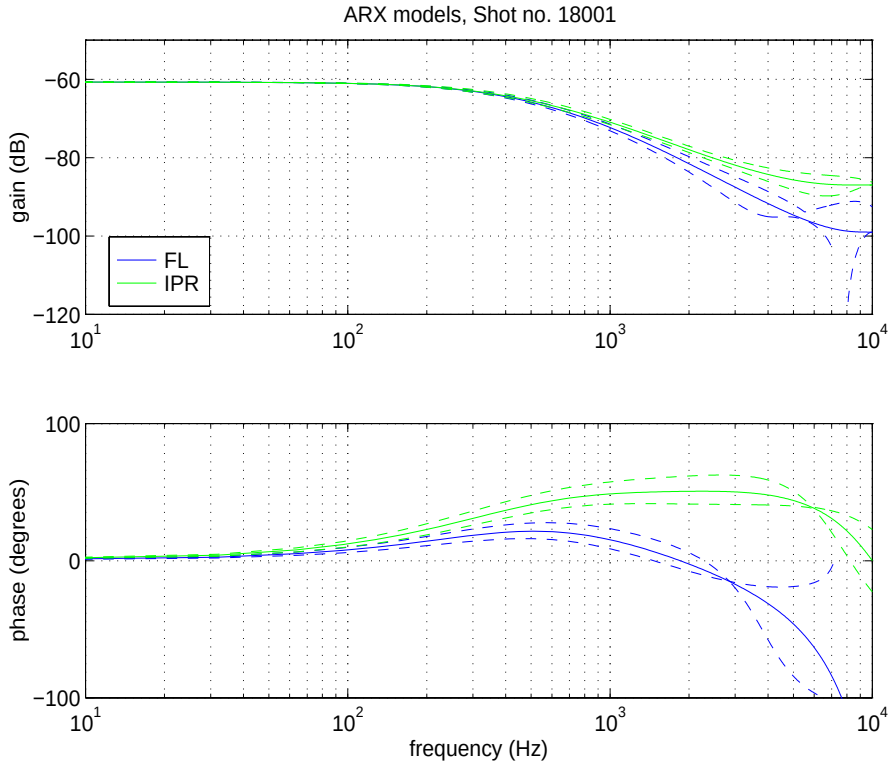


Figure 3.14 Comparison of FL and IPR frequency response. The IPR gain is normalized to the FL gain to allow comparison of the model roll off.

3.7 Experimental results

The system identification procedure was applied to plasmas at different operating points. In particular the effect of the shaping field on the plasma model was studied. Results on the effect of the toroidal field are also presented. Plasma operation in ELMy H–mode and ELM free H–mode is also examined. The procedure used to obtain the models was the same for each shot. Note that in all the shots the plasma is open loop unstable and that a single unstable pole is obtained in each model without any a priori information on the plant instability. A list of shots with RBS excitation is provided in Table 3.2. Comparison of predicted loop performance and experimental performance are presented in the following chapter.

Fig. 3.14 compares Bode plots of models obtained from shot no. 18001 for FL and IPR position signals. The 95% confidence bounds calculated from the uncertainty ellipses are also shown. The gain of the IPR model is divided by a factor of 3.90 to normalize the DC gain to the FL model value. This allows the roll off to be compared directly. Both models have a 3dB bandwidth of 350Hz. This is on the same time scale as the instability growth rate of both models (~2500) and the vessel time constant (estimated in the region 400 to 600μs). The FL model roll off is steeper and the difference between the two models it 3dB at 1750Hz. The IPR model has less phase lag with maximum value 22° compared with a maximum of 50° for the FL model. The FL phase lag and gain roll off is expected from shielding by the vessel wall.

Increasing the shaping current in theory increases the instability growth rate. Experiments were performed in which the shaping current was ramped up slowly during the flattop whilst the vertical position was being excited by an RBS signal. Models were then identified from 50ms data windows at different times. Figure 3.15 shows the FL model continuous time unstable pole against the I_s/I_p ratio in the middle of the time window for the SND and SNT configuration shaping coils. For shot no. 14704 (SND) I_s was ramped up from 3900A at the start of the RBS sequence (0.1s), to 7000A at the end of the sequence (0.26s). The plasma current was constant throughout the shot at I_p=144kA. For shot no. 16553 (SNT) the shaping current was ramped from I_s=1800A at t=0.1s to 4500A at 0.26s with I_p=151kA. As expected increasing the I_s/I_p ratio for the two configurations increases the instability growth rate.

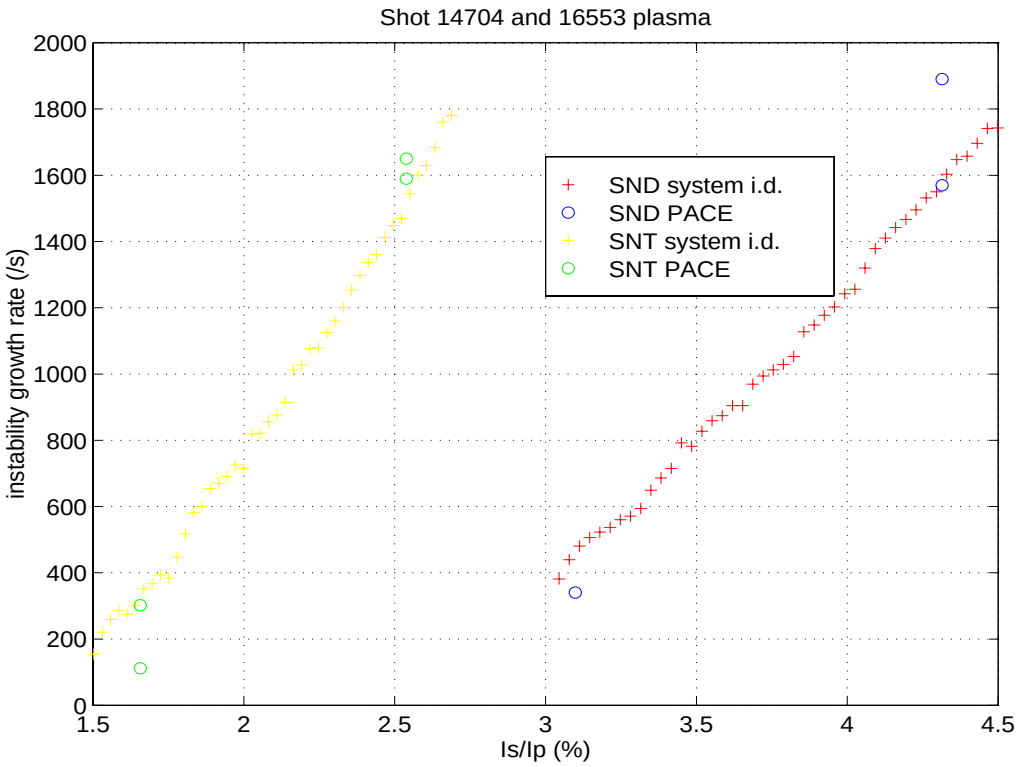


Figure 3.15 Open loop instability growth rate for SND and SNT plasma.

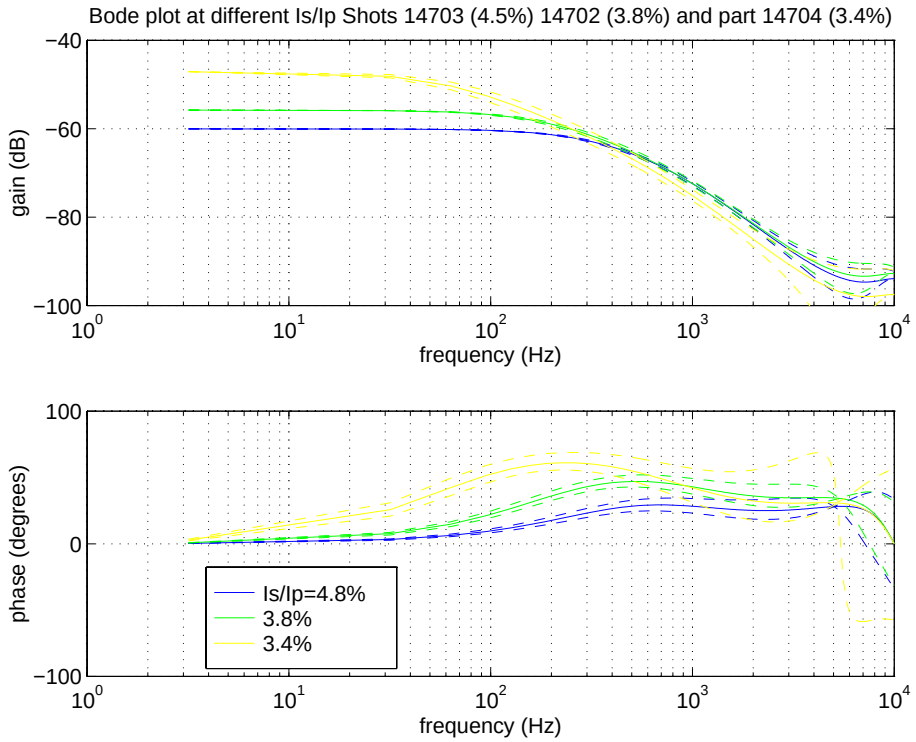


Figure 3.16 Bode plot of SND configuration plasma at different I_s/I_p.

There is a strong dependence of growth rate on shaping field, with roughly a fivefold increase in instability growth rate measured for each shot with less than a doubling of shaping current. Also marked are estimates of growth rate obtained independently by Dr. P.J. Knight, UKAEA Fusion [Knight95], from the PACE axisymmetric current filament simulation program [Knight92]. The estimates are in good agreement with the system identification results.

Table 3.2 List of shots with RBS excitation.

Shot no.	I_p/kA	I_s/I_p /%	B_T/T	growth rate/s^{-1}	DC gain
14702	144	3.82	1.5	1251	1.6×10^{-3}
14703	143	4.83	1.5	2299	1.0×10^{-3}
14704	144	2.7 to 4.9	1.5	~400 to ~1800	
16553 (SNT)	151	1.2 to 3.0	1.5	~200 to ~1600	
17775	175	4.74	1.1	2156	9.0×10^{-4}
17850	143	4.77	1.3	2084	1.0×10^{-3}
18001	142	4.89	1.2	2451	9.2×10^{-4}

Figure 3.16 shows three FL models at different I_s/I_p ratios in the SND configuration. The 4.8% and 3.8% models were obtained with I_s/I_p fixed over 160ms. The 95% confidence limits are relatively small and much smaller than the difference between the two models. The 3.4% model is obtained from a 50ms window of the I_s/I_p ramp shot used in Fig. 3.15. The confidence bounds are wider but still much less than the model differences. As the I_s/I_p ratio increases, the 3dB bandwidth increases and the DC gain decreases. The gain is similar for all three models above 400Hz. The phase lead decreases with I_s/I_p and this, along with an increase in bandwidth, is expected when the magnitude of an unstable pole increases.

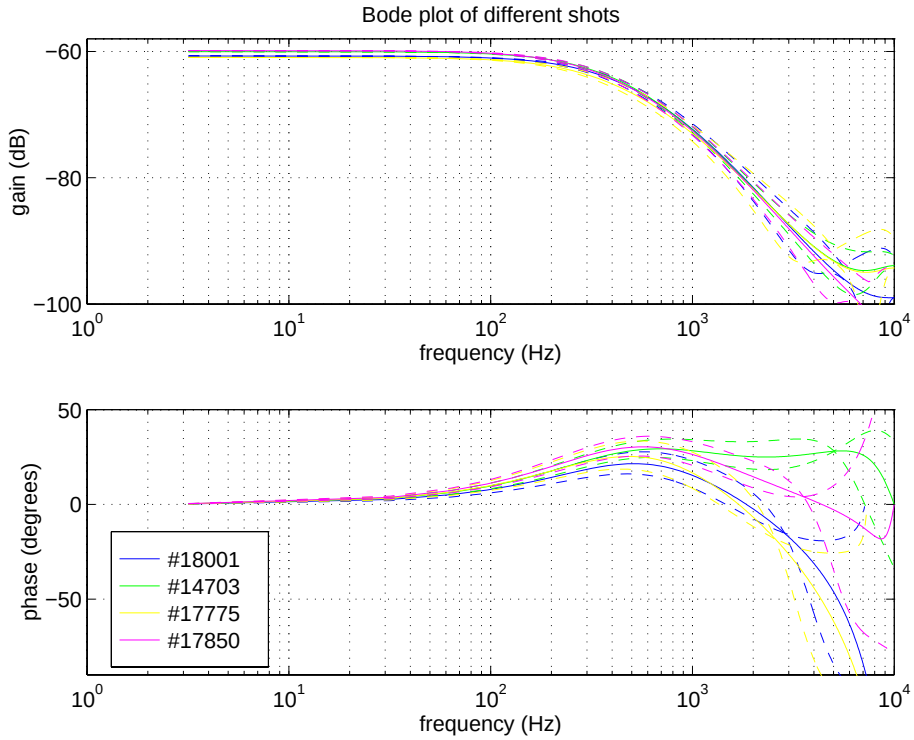


Figure 3.17 Effect of toroidal field on frequency response.

The effect of the toroidal field on the vertical position frequency response was also studied on COMPASS–D. Using a heuristic argument the toroidal field can alter the current profile of the plasma and therefore change the dynamics of the system. Plasma instabilities force the safety factor at the centre of the plasma to unity. Changing the toroidal field B_T (or plasma current) changes the safety factor at the edge (2.2), with high values leading to a more peaked profile. Figure 3.17 contains the Bode plots from shots with similar I_s/I_p ratios. There is little evidence of any effect when changing B_T from 1.1T (at I_p=175kA) to 1.5T (at I_p=143kA). Any small changes that exist may be due to the slight variations in I_s/I_p ratio than the toroidal field.

The shot in Fig. 3.18 operates in ELMy H–mode until 128ms and then switches into ELM free operation. The plasma disrupts at 148ms. Frequency responses for these models were obtained with 25ms of data during the ELMy period and 20ms during the ELM free period. The model frequency responses (Fig. 3.19) are similar but the 95% confidence limits are too large to draw any conclusions.

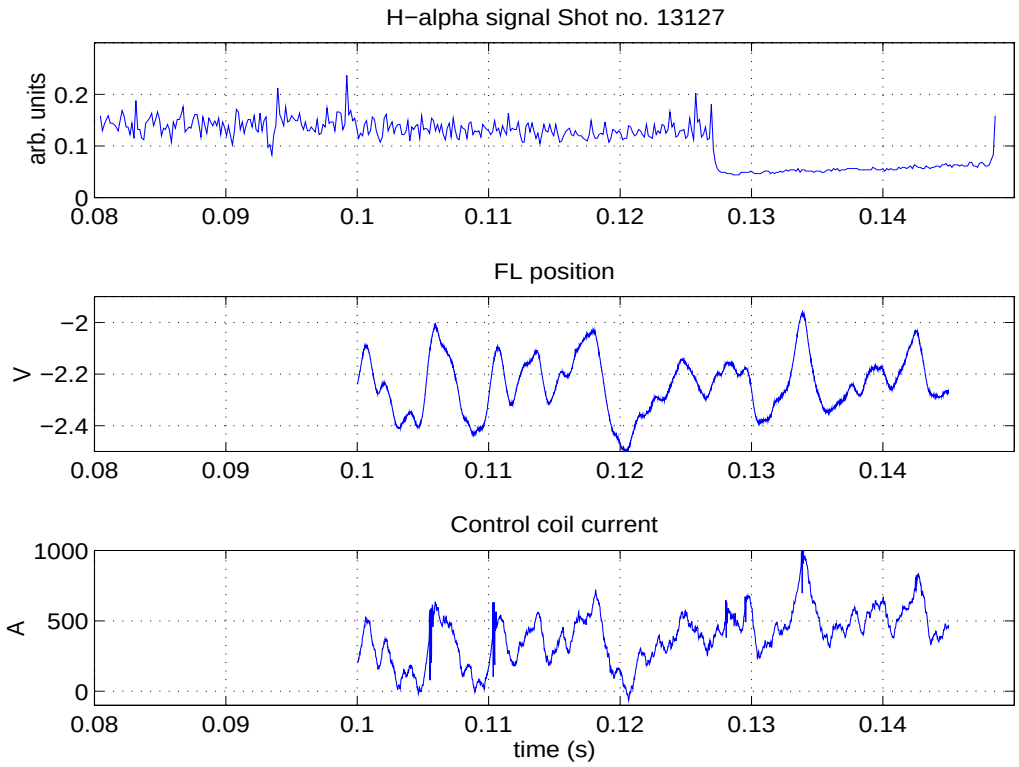


Figure 3.18 ELMy to ELM free H–mode plasma.

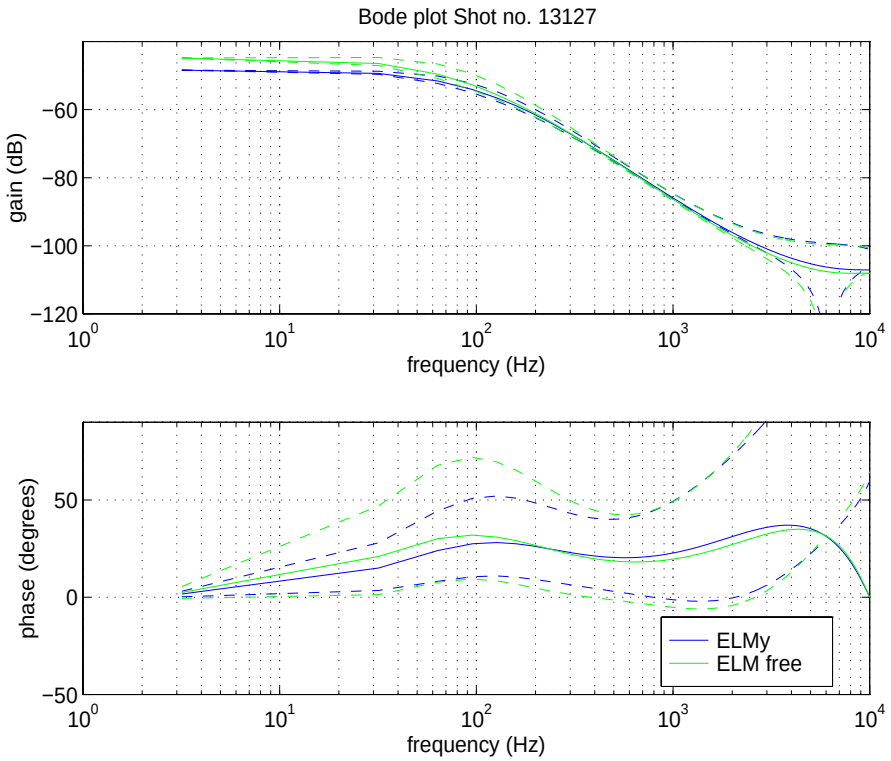


Figure 3.19 Frequency responses of ELMy and ELM free periods.

3.8 Summary

The aim of this chapter has been to examine a system identification method to model the open loop plasma vertical position response to control coil currents and to examine properties of the model.

The first part of the chapter examines the use of PEM in system identification and it is noted that in open loop identification the model fit is weighted by the signal to noise ratio of the system. The role of the model structure is examined and it was shown that an autoregressive term is required to identify unstable poles. The estimated model parameters are unbiassed if the noise and data sequences are uncorrelated, and confidence bounds can be calculated from estimates of the model parameter variances.

A 10kHz RBS signal was used to excite the modes of the plasma position system and 160ms of data was collected from each experiment. The models were then identified at a sampling frequency of 20kHz. The data was prefiltered to remove the 600Hz noise component and high pass filtered to emphasize the high frequency fit of the models. A low order model structure was chosen which represented a compromise between model bias and variance.

The system identification procedure was used on a variety of shots aimed at examining the dependence of the model on the shaping field. The dependence of model on toroidal field and ELMy and ELM–free operation in H–mode was also studied. All models contained a single unstable pole and the FL signal model exhibited a faster amplitude roll off at high frequencies and less phase lead than the equivalent IPR signal model. The instability growth rate is strongly dependent on shape but less so on toroidal field. Increasing the shaping field for a given plasma current reduces the DC gain of the model and increases the bandwidth. The phase lead decreases with shaping field. The models were less sensitive to toroidal field in the range 1.1T to 1.5T. This may indicate that any changes in current profile that may have occurred did not significantly alter the plasma coupling to the vessel structure. Determining models from the short ELMy and ELM–free periods on COMPASS–D proved to be difficult because of the large model variances arising from using a limited number of data samples.

The models developed above are used in the following chapter to design high order controllers and are compared with experimental results on the loop stability margins.

4 Linear Control

4.1 P+D performance

The COMPASS–D analogue P+D controller as described earlier performs well in practice with the exception of large 600Hz oscillations and occasional loss of control when disturbed by large separated ELMs. The system adequately stabilizes plasmas with high instability growth rates (of order $2500s^{-1}$).

The P+D controller makes use of internal magnetic field sensors which are not affected by shielding from the vessel wall. Internal measurements will not be available on ITER because of harsh reactor conditions. This will adversely affect the controller stability margins as indicated in Fig. 4.1. The plot shows the Nyquist diagram of the loop gain ($L_{FL/IPR}$) for COMPASS–D with the internal and external measurements

$$L_{FL/IPR} = -G_s G_l G_a G_c (G_{FL} K_p - sG_{IPR} K_d / G_i)$$

The functions refer to the components of the block diagram in Fig. 2.15 with parameters and gains described in Chapter 2. The transfer function $L_{FL/IPR}$ represents the loop gain of the COMPASS–D vertical position system in routine operation. The plot encircles the $-1+0j$ point once anticlockwise, which is required for closed loop stability of a plant with one unstable pole. The DC gain is -5.57 and the phase crossover frequencies ($\sphericalangle L = 180°$) are 170Hz and 3960Hz. The corresponding upper and lower gain margins are 0.723 and 12.25 respectively. The gain crossover frequency ($|L| = 1$) is 369Hz with phase margin $22°$.

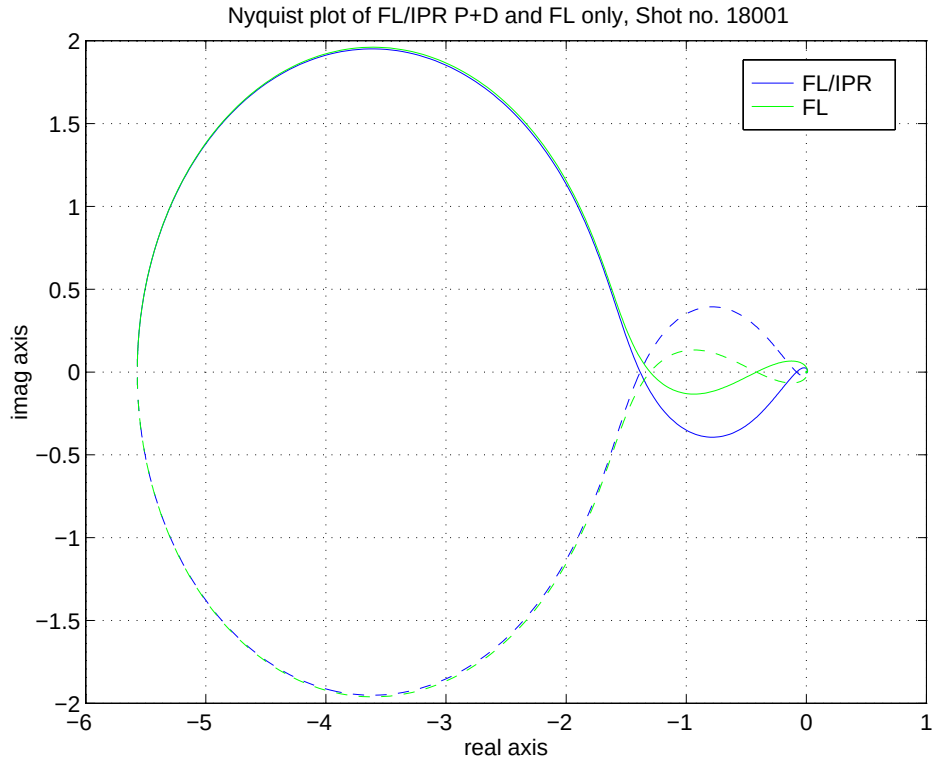


Figure 4.1 Nyquist diagram of FL/IPR loop ($L_{FL/IPR}$) and FL only loop (L_{FL}).

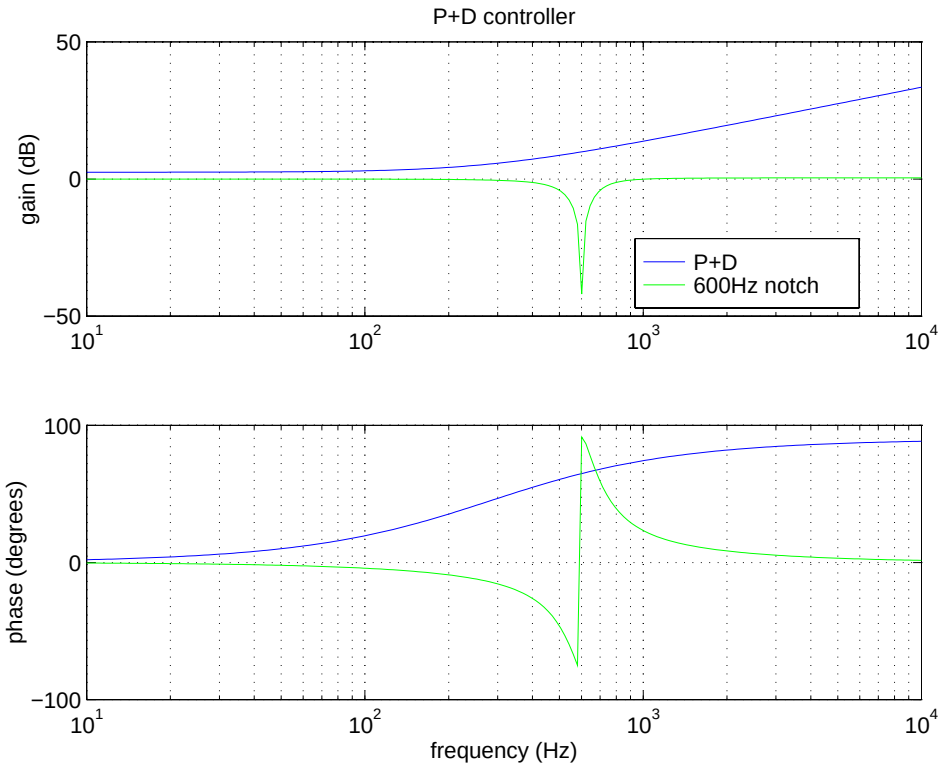


Figure 4.2 Bode plot of P+D controller and 600Hz notch filter.

Also marked on the diagram is the loop gain for the loop with FL measurements for both position and velocity

$$L_{FL} = -G_s G_l G_a G_c G_{FL}(K_p^{/} - sK_d^{/}/G_i)$$

The controller gains $K_p' = K_p$ and $K_d' = K_d G_{IPR}(0)/G_{FL}(0)$ are chosen to provide the same time constant as the FL/IPR hybrid system ($L_{FL/IPR}$). The plot passes closer to the $-1+0j$ point. The phase crossover frequencies are 231Hz and 951Hz with corresponding upper and lower gain margins 0.77 and 2.41. The gain crossover frequency is 388Hz with phase margin 7.5°. Small errors in the model or changes in the operating point would cause the FL only system to become unstable. This is mainly due to the phase lag introduced by the vessel wall. Moving the controller zero to a lower frequency increases the phase lead but also increases the gain (Fig. 4.2). The gain margins can be changed significantly but the phase margin cannot be appreciably improved.

Another problem on COMPASS–D is the presence of 600Hz noise, which is also present on JET. This could be removed by introducing a notch filter. However as the Bode plot in Fig. 4.2 shows, the filter introduces more phase lag below 600Hz with

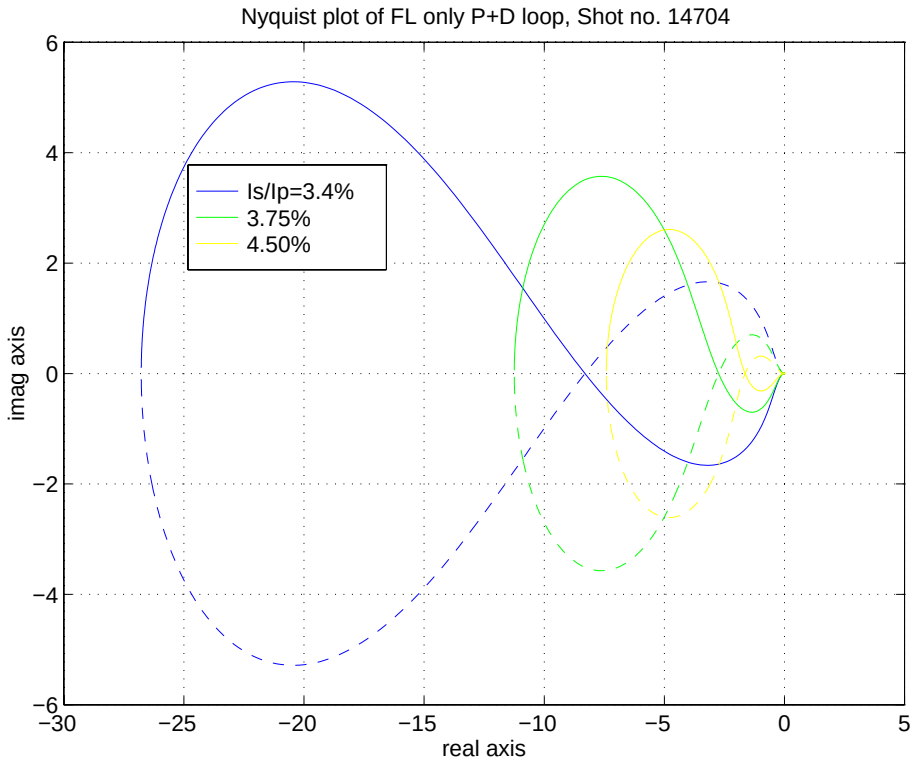


Figure 4.3 Nyquist plot of P+D FL only loop at different I_s/I_p.

adverse effects on stability.

Experiments conducted on COMPASS–D with the FL only P+D controller were attempted. It proved difficult to find any combination of P+D gains to stabilize the plasma at the required I_s/I_p ratio. Lower I_s/I_p plasmas were easy to stabilize as shown in the Nyquist diagram of Fig. 4.3. The plot shows the loop gain L_{FL} when the plant model G_{FL} is identified at different I_s/I_p ratios. Seen clearly is the effect of the plant DC gain decreasing with I_s/I_p. Also note the effect of decreasing phase lead, which brings the Nyquist plots closer to the -1+0j point at higher I_s/I_p.

4.2 Controller objectives

Advanced controllers were designed and tested on COMPASS–D with the aim of demonstrating two objectives. The first is that it is possible to improve vertical position stability when the velocity sensors are shielded by the vessel wall (as may be the case for ITER). The second is that it is also possible to reduce the effect of thyristor power supply noise (as present on COMPASS–D and JET).

The main objective of any controller is to stabilize the system (during startup and the flattop period). The controller should be able to accommodate the change in I_s and I_p during the startup. The plasma will be stable at startup and open loop unstable during flattop. The controller must robustly stabilize the plasma with stability margins large enough to allow for plant model uncertainty. Variations in the plasma system can also occur because of changes in the plasma current density profile due to different toroidal fields, plasma heating and L or H–mode of operation.

The main objective on COMPASS–D is regulation of the plasma at a fixed reference position during the shot and when experiencing different disturbance loads and sensor noise. For COMPASS–D the main problem is voltage saturation of the power amplifiers. Minimizing the oscillations due to the 600Hz disturbance and noise would allow a larger amplifier headroom.

Modern control theory allows the design of high order controllers to meet these objectives with the possibility of improving the performance of the system. Two different approaches were followed to design the controller. The first approach uses continuous time $\mathbf{H}_\infty$ control theory. The second approach uses SGPC control theory

and is based in discrete time. The two approaches result in controllers which have frequency responses which resemble each other. Results of experimental tests of the controllers on COMPASS–D are presented. Some model validation tests were also conducted on COMPASS–D to compare gain margins predicted from the system identification models with experimentally measured values.

4.3 H_∞ problem structure

Plasma position controllers based on the $\mathbf{H}_\infty$ design method have been proposed for tokamaks (see [Al–Husari91] and [Portone94]). This method allows constraints based on the frequency response of the closed loop system to be specified and a solution for a controller meeting the constraints to be found. Useful references are [Doyle92] and [Green95]. A brief explanation of the $\mathbf{H}_\infty$ norm and how the constraints are specified is first presented. The plant model and weights chosen are then described followed by experimental results. The controller was implemented on the DSP (digital signal processor) described in Section 2.8.

For a transfer function $F(s)$ the $\mathbf{H}_\infty$ norm of $F(s)$ $(\|F(s)\|_\infty)$ is the maximum value of the amplitude of the frequency response of $F(s)$, i.e.

$$\|F(s)\|_\infty \triangleq \max_\omega |F(j\omega)|$$

The norm is useful in specifying the robust stability and performance properties of the closed loop. If the loop gain of the system is defined as $L(s) \triangleq G(s)K(s)$ then the closed loop sensitivity is $S(s) \triangleq 1/(1+L)$ and the complementary sensitivity is $T(s) \triangleq L/(1+L)$. Given a nominal model of the plant G and the controller K, it may be the case that the predicted closed loop system is stable. However the actual plant G' may differ from G due to modelling errors. In this case the closed loop system may not be stable. A set of models based on the nominal plant with a multiplicative uncertainty bound can be considered

$$G' \in \left\{ G(1+W_1\Delta);\ \|\Delta\|_\infty < \gamma \right\}$$

where γ is a scalar, $W_1(s)$ is a stable weight and $\Delta(s)$ is any transfer function such that G and G' have the same number of unstable poles. The weight W_1 is chosen to allow a larger range of uncertainty at a chosen frequency range. The scalar γ is a measure of the stability margin of the system, with larger values of γ allowing for a larger range of uncertainty. A controller is able to stabilize any plant G' in the set if and only if

$$\|\gamma W_1 T\|_\infty < 1 \qquad \textbf{(4.2)}$$

A heuristic interpretation of this condition can be obtained by examining a typical Nyquist diagram (Fig. 4.1). The distance from the $-1+0j$ point and a point on the loop gain $L(j\omega)$ is $1+L(j\omega)$. Ideally the quantity $1+L$ is large to accommodate any variations in the plant model. The reciprocal of the distance is S, and T is proportional to the reciprocal. Ensuring that either S or T is small ensures that the distance $1+L$ is large.

The effect of the 600Hz noise on the control signal can be reduced by a similar constraint. The closed loop transfer function from the noise source n to the controller demand signal v is KS (Fig. 4.4). A weight with a peak at 600Hz and small at other frequencies can be constructed (see Fig. 4.5). The constraint is then

$$\|W_2 KS\|_\infty < 1 \qquad \textbf{(4.3)}$$

Since W_2 is large at 600Hz, KS must be small at 600Hz to satisfy the constraint. Putting a notch filter in the plant without this constraint results in controllers that cancel the notch and leave the closed loop gain at 600Hz relatively large.

The position error e should be small at low frequencies for satisfactory regulation of the plasma position. The transfer function from a noise or plant output disturbance to the error is S. A low pass filter can be used to penalize S at low frequencies with the constraint

$$\|W_3 S\|_\infty < 1 \qquad \textbf{(4.4)}$$

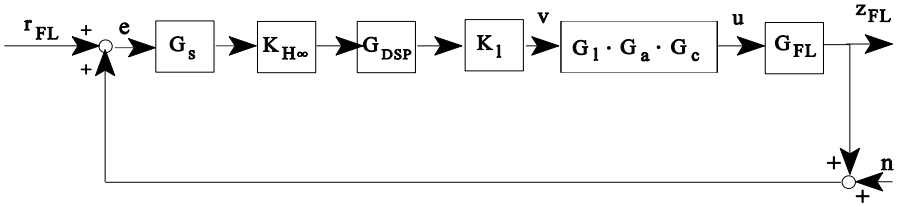


Figure 4.4 H_∞ Block diagram.

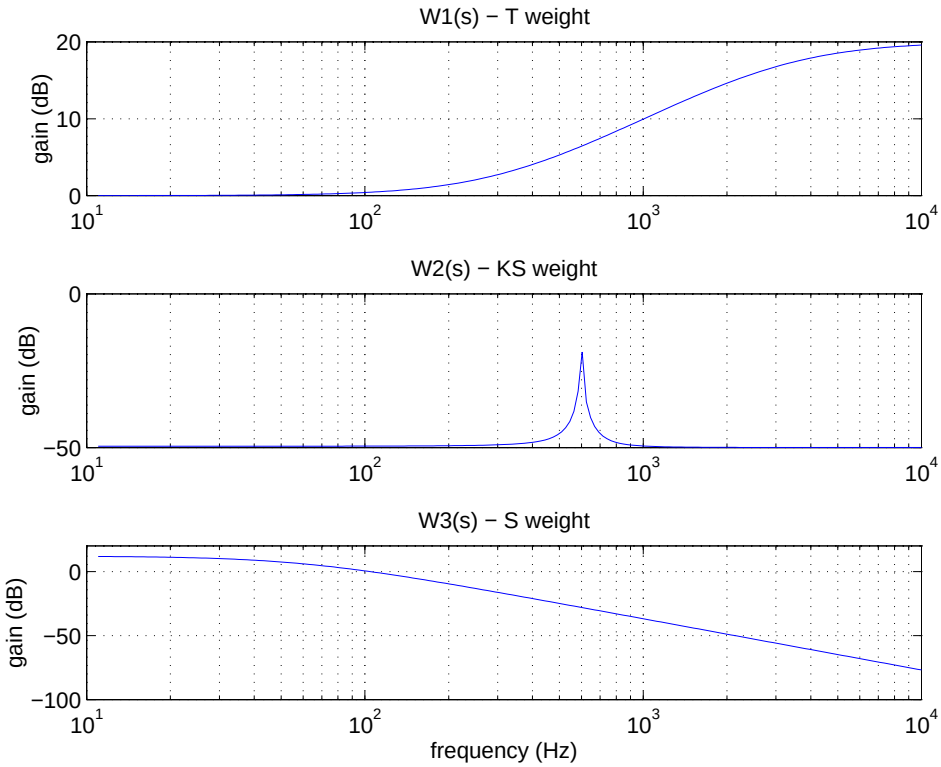


Figure 4.5 Weights for H_∞ controller.

The overall optimization problem is then to find the controller which satisfies all three constraints for the largest value of γ. This is difficult to calculate but a more tractable problem is to find the controller which satisfies

$$\left\| \begin{matrix} \gamma W_1 T \\ W_2 KS \\ W_3 S \end{matrix} \right\|_\infty < 1 \Leftrightarrow \left\| (|\gamma W_1 T|^2 + |W_2 KS|^2 + |W_3 S|^2)^{1/2} \right\|_\infty < 1 \qquad \textbf{(4.5)}$$

A brief discussion of the optimization process follows and is useful not only for the $\mathbf{H}_\infty$ controller, but also the SGPC controller in this chapter and the peak impulse response controller in the next chapter.

The first step is to parameterize the set of all stabilizing controllers for a given plant. First the set $\mathbb{R}\mathbf{H}_\infty$ is defined as the set of all stable real–rational proper transfer functions. Then the plant $G(s)$ is factorized by coprime factors $N(s)$ and $D(s)$ such that

$$G(s) = \frac{N(s)}{D(s)}$$

Coprime factors are any pair of transfer functions $N(s) \in \mathbb{R}\mathbf{H}_\infty$ and $D(s) \in \mathbb{R}\mathbf{H}_\infty$ for which there exists another pair of transfer functions $X(s) \in \mathbb{R}\mathbf{H}_\infty$ and $Y(s) \in \mathbb{R}\mathbf{H}_\infty$ such that the Bezout identity is satisfied

$$NX + DY = 1.$$

Any controller $K(s)$ stabilizing the plant $G(s)$ can be written in terms of the Youla parameter $Q(s) \in \mathbb{R}\mathbf{H}_\infty$

$$K = \frac{X + DQ}{Y - NQ}$$

The problem of finding the stabilizing controller K which satisfies the constraints in (4.5) can be transformed into a search over the set $\mathbb{R}\mathbf{H}_\infty$. Any closed loop transfer function is an affine function of Q for example,

$$\begin{aligned} T &= N(X+DQ) \\ KS &= D(X+DQ) \\ S &= D(Y-NQ) \end{aligned}$$

Methods exists for calculating the optimal Q. The Matlab Robust Control Toolbox [Chiang92] was used to obtain the $\mathbf{H}_\infty$ optimal controller. The controller was checked with models of the plasma during startup to ensure stability. The controller was then converted to discrete time form and finally tested on COMPASS–D.

The $\mathbf{H}_\infty$ controller was implemented using the DSP as shown in the block diagram of Fig. 4.4. All the transfer functions are continuous time and where necessary are continuous time approximations of discrete time systems. The plant transfer functions (G_{FL}, G_s, and $G_lG_aG_c$) are the same as for the P+D loop. A multiplying waveform generator is also used and is represented by K_l. In most experiments its gain is normalized to unity but it is used to find the stability gain margins in experiments described in the next section. The DSP transfer function (G_{DSP}) is used to represent the parts of the DSP system not directly associated with the controller transfer function. It includes 50kHz Bessel filters which act as the input and output buffer amplifiers, a 37.5μs time delay and a zero order hold on the DSP DAC. An FIR filter is used to average four samples (at 80kHz sampling frequency) before the controller transfer function is applied. This is also included in G_{DSP} along with a DC gain K_{DSP}= 0.1. The elements of G_{DSP} are essentially fixed and should be considered as part of the plant when designing the controller. The transfer function of the $\mathbf{H}_\infty$ controller is represented by $K_{H\infty}$.

The plant model $G(s)$ used to obtain the controller consists of two parts $G=G_1G_2$. The first represents the amplifier, optical link and control coil model

$$G_1(s)=\frac{G_s K_{DSP} K_a p_a \bar{p}_a}{(sL_c+R_c)(s-p_a)(s-\bar{p}_a)}$$

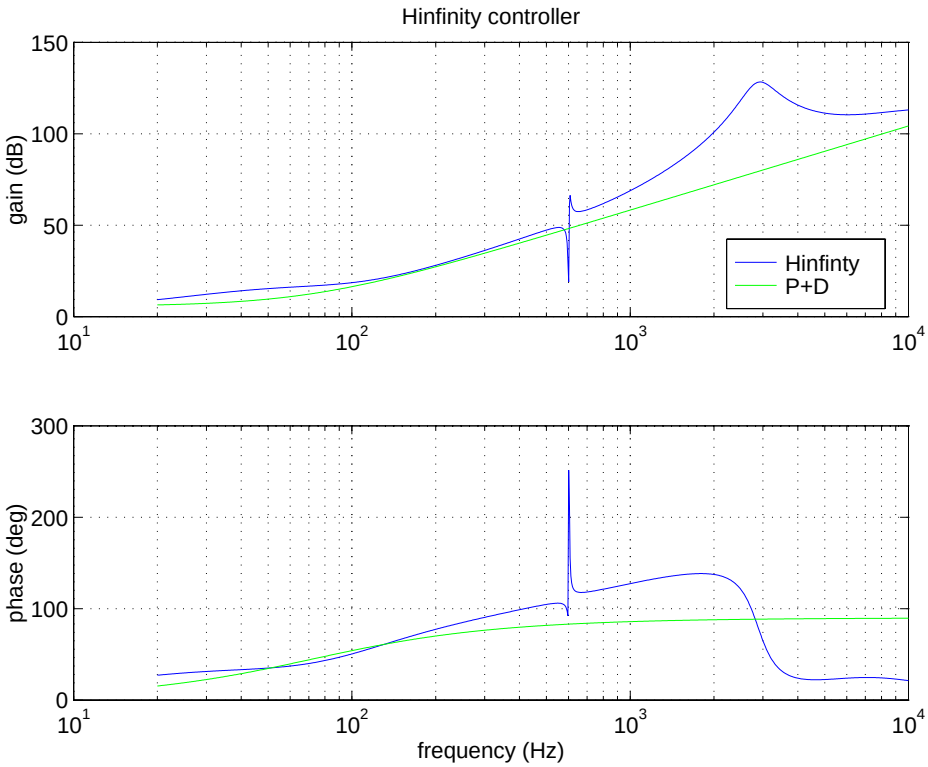


Figure 4.6 Bode plot of $\mathbf{H}_\infty$ and P+D controller.

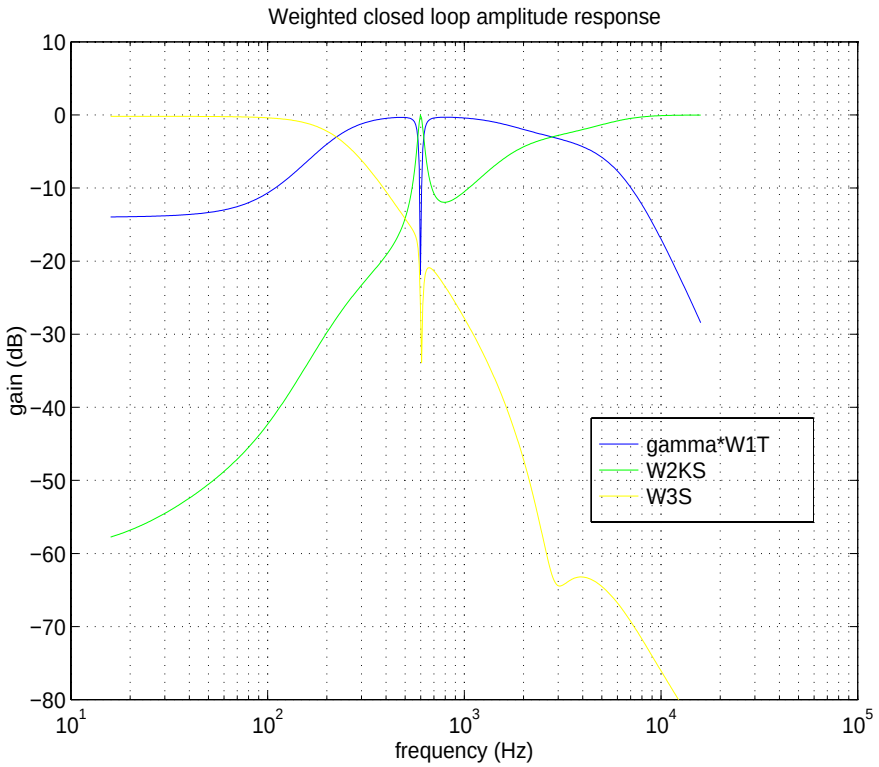


Figure 4.7 Weighted closed loop transfer functions.

where the values of the parameters are defined in Chapter 2. The high frequency poles and time delays (in the amplifier and DSP buffers etc.) are not included in G_1. Instead they are represented as a 100μs (two samples) delay in the discrete time plasma model obtained from system identification in the previous chapter. This is then converted to continuous time using Tustin's approximation to form G_2.

The weights for the controller are

$$W_1(s) = \frac{10\tau_1 s+1}{\tau_1 s+1}$$

$$W_2(s) = \frac{1}{315}\times\frac{(s-z_2)(s-\bar{z}_2)}{(s-p_2)(s-\bar{p}_2)}$$

$$W_3(s) = \frac{4}{(\tau_3 s+1)^2}$$

with τ_1=50μs, z_2=-843+3770js^{-1}, p_2=-0.5+3770js^{-1}, and τ_3=1/(120π)s. The amplitude responses of these weights are shown in Fig. 4.5. The weight on the uncertainty W_1 was chosen to ensure a large gap around the $-1+0j$ point. The frequencies at which the loop gain is close to the $-1+0j$ point are in the range ~200Hz to 1kHz. The weight was chosen in a heuristic manner by assuming that the multiplicative uncertainty at high frequencies was a factor of 10 times larger than the low frequency uncertainty. The weight zero was chosen at 2000s^{-1} because this produced loop gains with large gaps around the $-1+0j$ point. The value of γ in the weight is maximized by optimization. The weight W_2 was chosen with the 600Hz peak gain large to make the loop gain small at 600Hz. It was found that the maximum value of γ obtained was sensitive to the high frequency (>1kHz) gain of weight W_2. Smaller values of the weight produce larger values of γ but also leads to higher amplification of high frequency noise. The robust stability properties using this weight is strongly dependent on the high frequency noise characteristics of the system. The DC gain of W_2 was fixed at 1/300. Empirical experience suggested that this allowed a stable closed loop with no problems associated with high frequency noise amplification. Early experiments on COMPASS–D with controllers designed without weight W_3 resulted in large steady state errors. The controller DC gain was low and as the I_s/I_p of the plasma was increased (with the DC gain of the plant decreasing), the plasma

position would drift steadily away from the reference position. This was overcome by using weight W_3 to ensure that the low frequency loop gain was large so that the steady state error was relatively small.

The controller was calculated from the nominal plant and weights with the optimal result γ=0.16 and a 13th order controller. The calculations were in state space form but for convenience the coefficients of the resulting controller continuous time transfer function are presented in Table 4.1. The 20kHz discrete time state space representation is then calculated using Tustin's approximation with prewarp compensation at 600Hz and the controller is then converted to second order section form and implemented on the DSP. The Bode plot of the controller in Fig. 4.6 shows a notch at 600Hz and extra phase lead below 600Hz when compared with a P+D controller. The weighted closed loop transfer functions in Fig. 4.7 show that each of the constraints is met.

Table 4.1 Coefficients of $\mathbf{H}_\infty$ controller transfer function.

power of *s*	numerator coefficient	denominator coefficient
s^{13}	0	1.000000000000000e+000
s^{12}	6.324798317899265e+008	2.901701553626014e+006
s^{11}	5.504424204403654e+014	2.046221773136846e+012
s^{10}	1.459573612324156e+020	5.292082507034910e+017
s^{9}	1.170147066811367e+025	4.979444371314840e+022
s^{8}	4.845515958934458e+029	2.556301851690816e+027
s^{7}	1.061393089846661e+034	7.167325992787366e+031
s^{6}	1.158097838097598e+038	1.310881951506497e+036
s^{5}	5.916586248930670e+041	1.772313411181326e+040
s^{4}	1.993423056038875e+045	1.330973846662705e+044
s^{3}	6.493215020700352e+048	3.243992521724254e+047
s^{2}	6.337801887267873e+051	1.667368323892760e+051
s^{1}	2.781995389625264e+054	1.145646357095258e+054
s^{0}	2.547199476431756e+056	2.097520822576406e+056

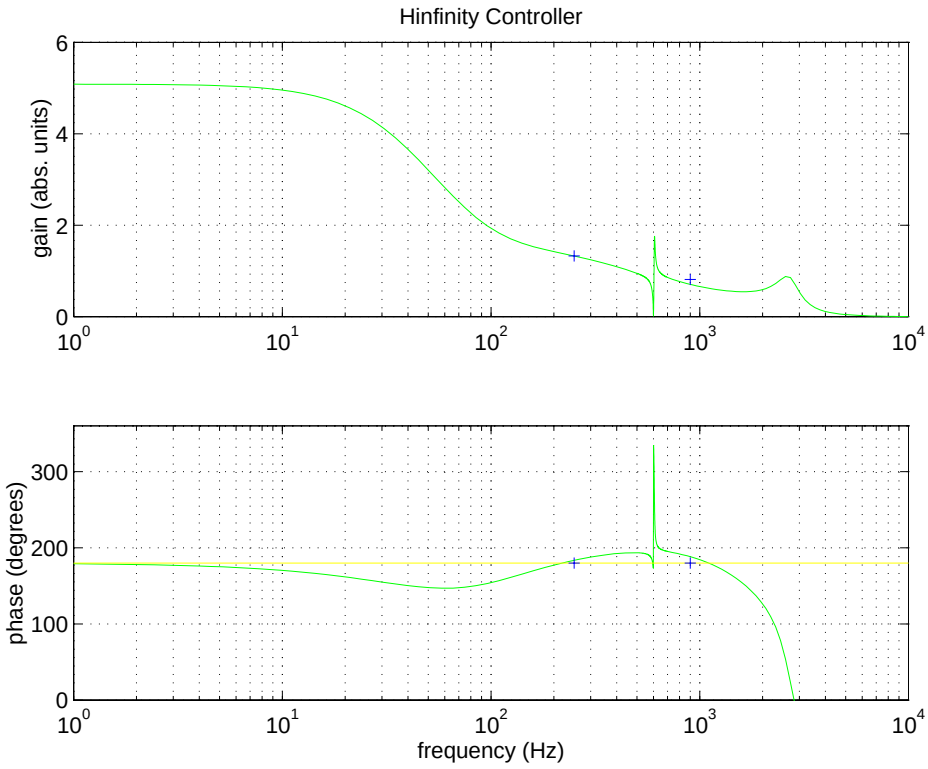


Figure 4.8 Bode plot of loop gain with $\mathbf{H}_\infty$ controller ($L_{H\infty}$). Loop gains determined from gain margin measurements are marked with crosses.

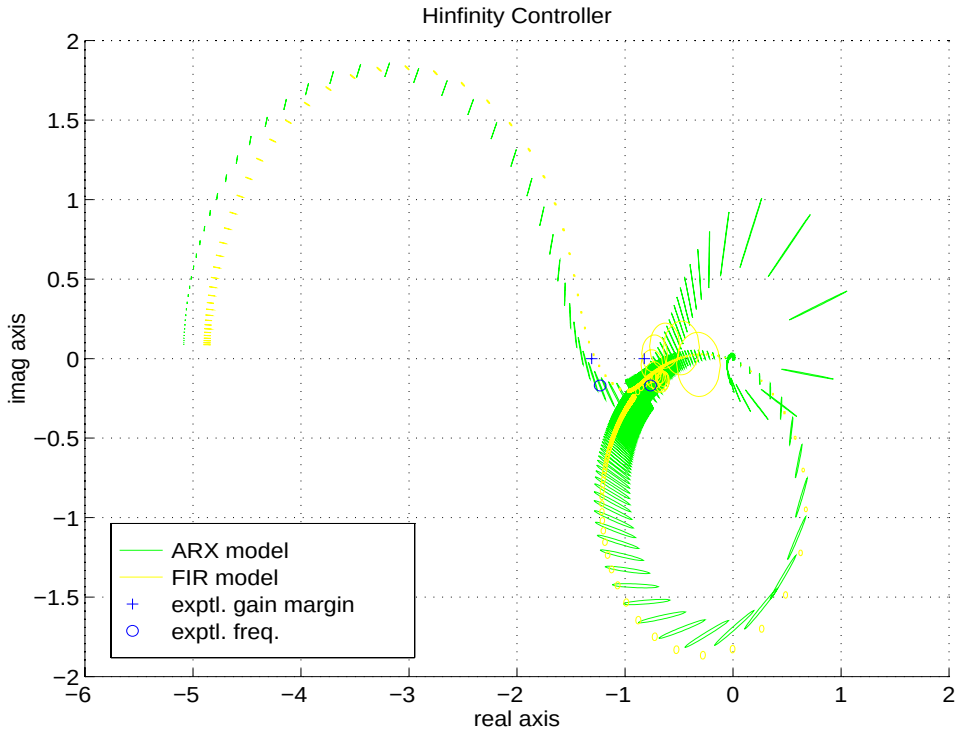


Figure 4.9 Nyquist plot of $L_{H\infty}$ using ARX and FIR models with 95% confidence bounds.

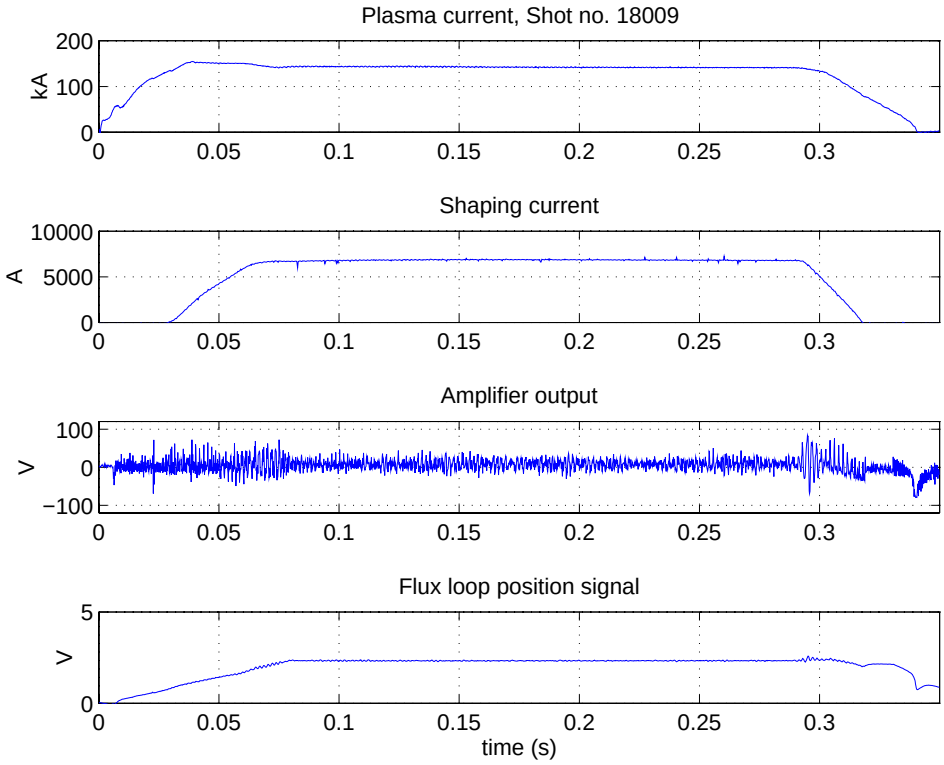


Figure 4.10 Shot using $\mathbf{H}_\infty$ controller ($K_{H\infty}$).

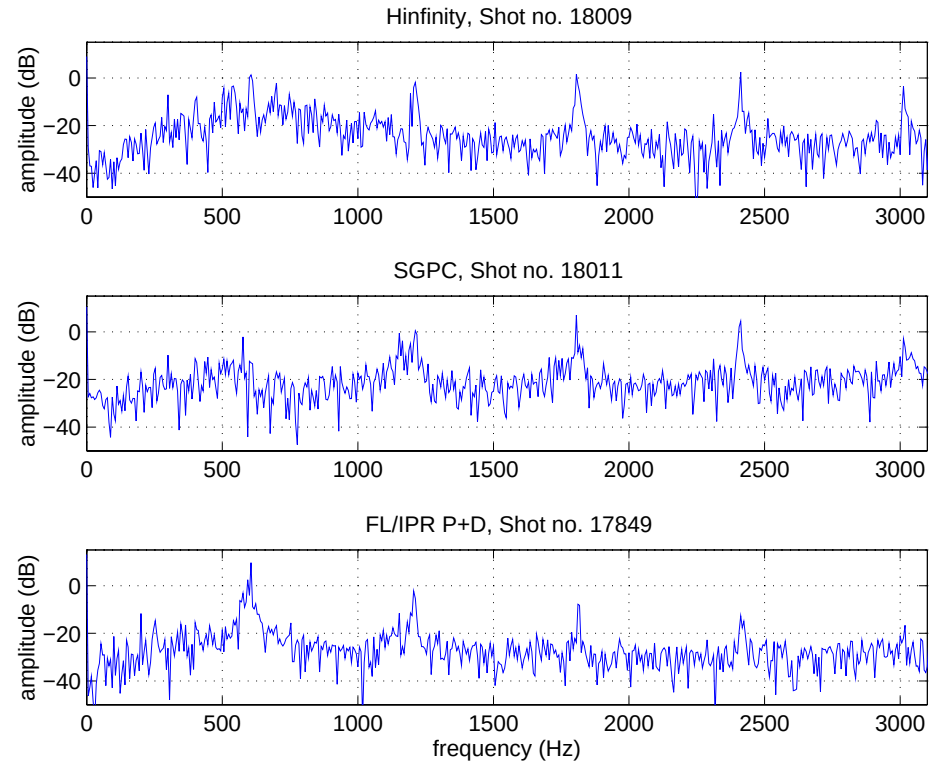


Figure 4.11 Comparison of amplifier frequency spectra.

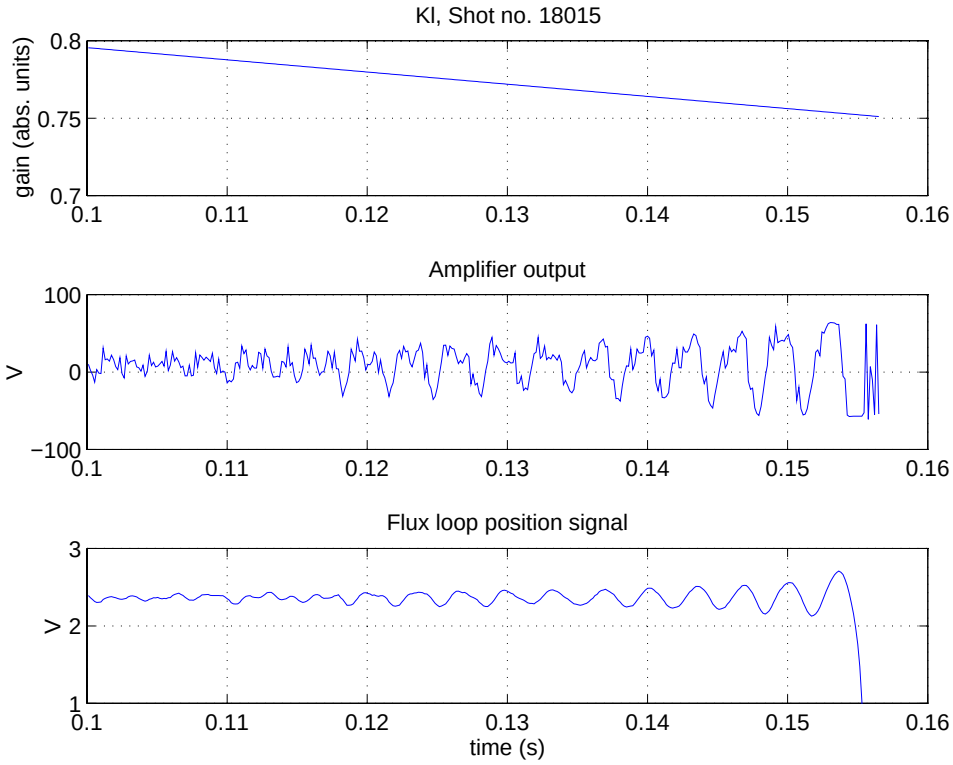


Figure 4.12 Effect of decreasing loop gain.

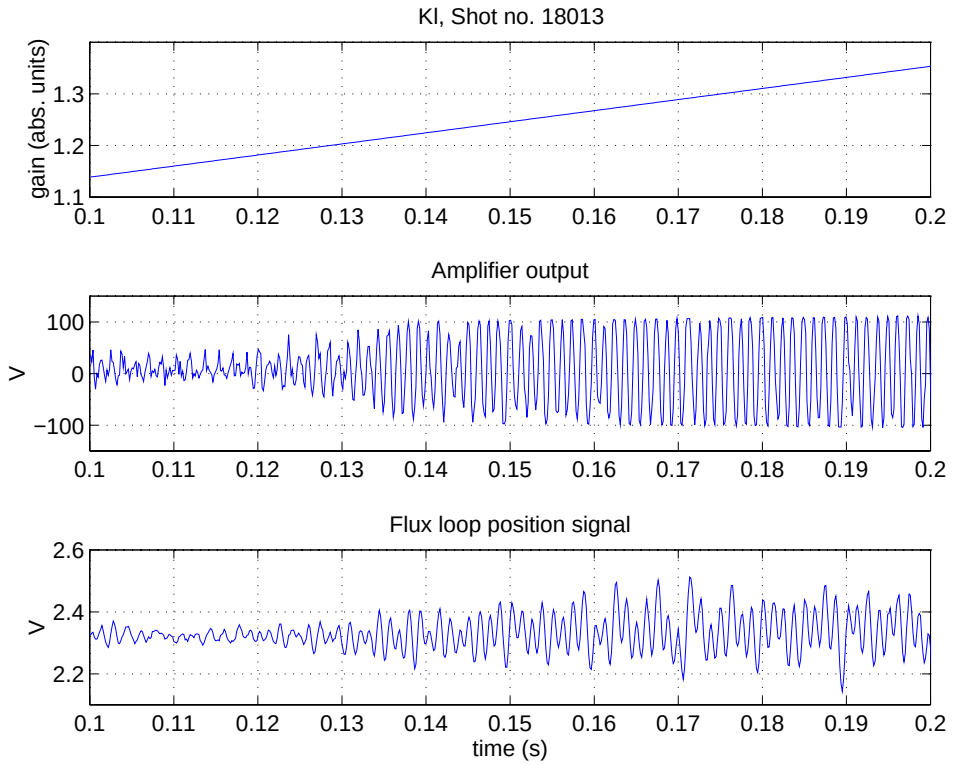


Figure 4.13 Effect of increasing loop gain.

4.4 H_∞ results

The $\mathbf{H}_\infty$ controller was tested on COMPASS–D in the loop shown in Fig. 4.4, with $K_{H\infty}$ representing the controller and K_l set to unity. The Bode and Nyquist plots of the loop gain $L_{H\infty}$

$$L_{H_\infty} = -G_s K_{H_\infty} G_{DSP} K_l G_l G_a G_c G_{FL}$$

are plotted in Figs. 4.8 and 4.9. The Nyquist plot passes close to the origin at 600Hz ($|L_{H\infty}| \approx 0.01$ at 600Hz) because the controller contains a notch at 600Hz. The results of using the controller on COMPASS–D are presented in Fig. 4.10. The plasma is stabilized at a typical SND plasma shape with I_p=142kA, I_s/I_p=4.83% and B_T=1.2T. The amplitude spectrum of the amplifier voltage does not contain the component at 600Hz (Fig. 4.11). The objectives were to stabilize the plasma for a typical shape using only the FL sensors and reducing the effect of the 600Hz noise on the control signal. These objectives were met satisfactorily.

Predictions of the gain margins were then compared with experimentally measured values by the changing the gain K_l during a shot. When decreasing the gain to K_l~0.78 the plasma position signal begins to oscillate at 250Hz. When K_l is below 0.76 control of the position is lost (Fig. 4.12). This provides information on the upper gain margin and crossover frequency as plotted in Figs. 4.8 and 4.9. The predicted values from the ARX model are K_l=0.72 and an oscillation frequency of 220Hz. Increasing the gain causes high frequency oscillations (Fig. 4.13) and the amplifier voltage become saturated. Saturation effectively reduces the gain of the system making it difficult to measure the lower gain margin. Loss of control occurs when K_l=1.88. However the gain for which the onset of oscillations occurs (K_l=1.23) and the frequency (900Hz) are indicated in the loop gain plot. The predicted values from the ARX model are K_l=1.60 and 1180Hz. Both gain margin results are in close agreement with the model demonstrating the validity of the system identification approach to modelling the plasma position system.

The crosses plotted in Figs. 4.8 and 4.9 are the values of $L_{H\infty}$ at 250 and 900Hz. They indicate that the phase lag of the loop is possibly underestimated. The lag is

approximately of the order of 50μs, delaying $L_{H\infty}$ by 4.5° at 250Hz and 16.2° at 900Hz. The shot in Fig. 4.14 shows the results of using an initial design of controller with the corresponding Nyquist plot in Fig. 4.15. This controller has a smaller stability margin and the plasma position and amplifier voltage oscillates with a beat envelope. The amplitude response indicates that the system resonates at 490 and 635Hz. The closed loop gain is also plotted in Fig. 4.16 along with a loop with extra phase delay (50μs). The oscillations are predicted by the model (at 440 and 630Hz). The conclusion is that the ARX model predicts the gain margins with close agreement from experimental results but that there is also some evidence of a small underestimate of the system phase lag.

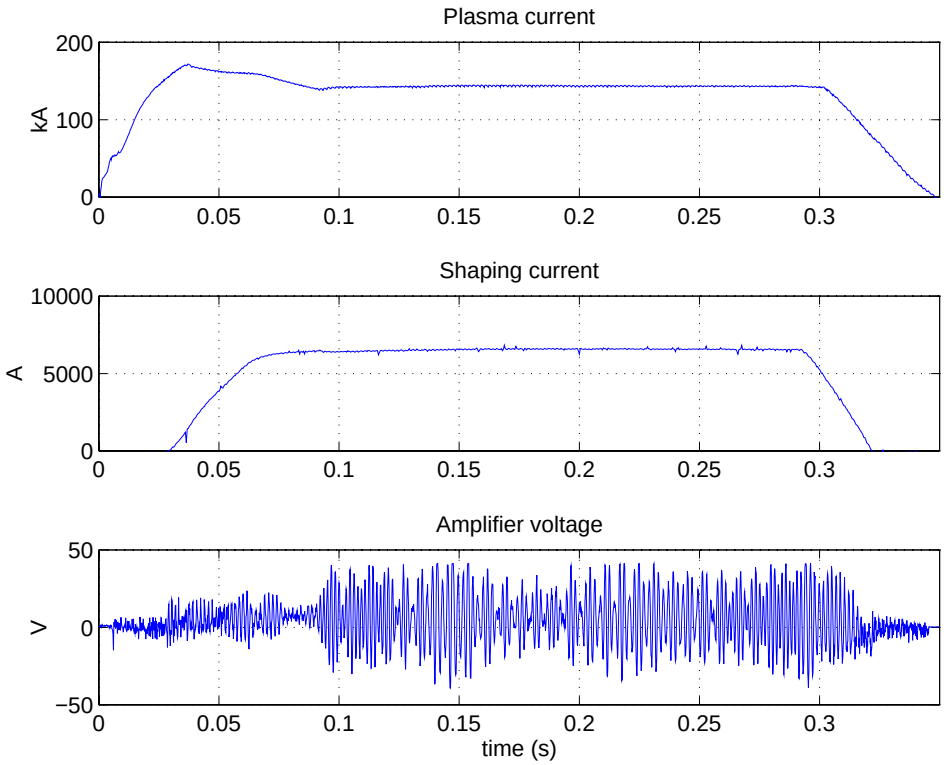


Figure 4.14 Vertical position signals for shot with poor stability margin.

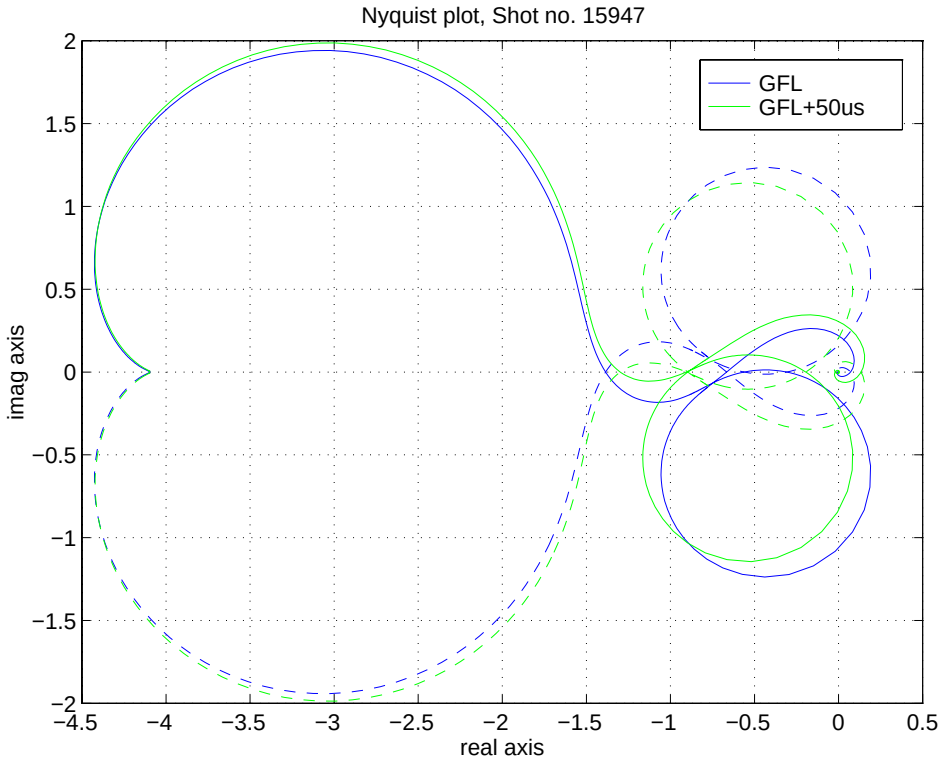


Figure 4.15 Nyquist plot of shot with poor stability margin. The nominal loop gain is plotted along with the effect of including a 50μs pure time delay.

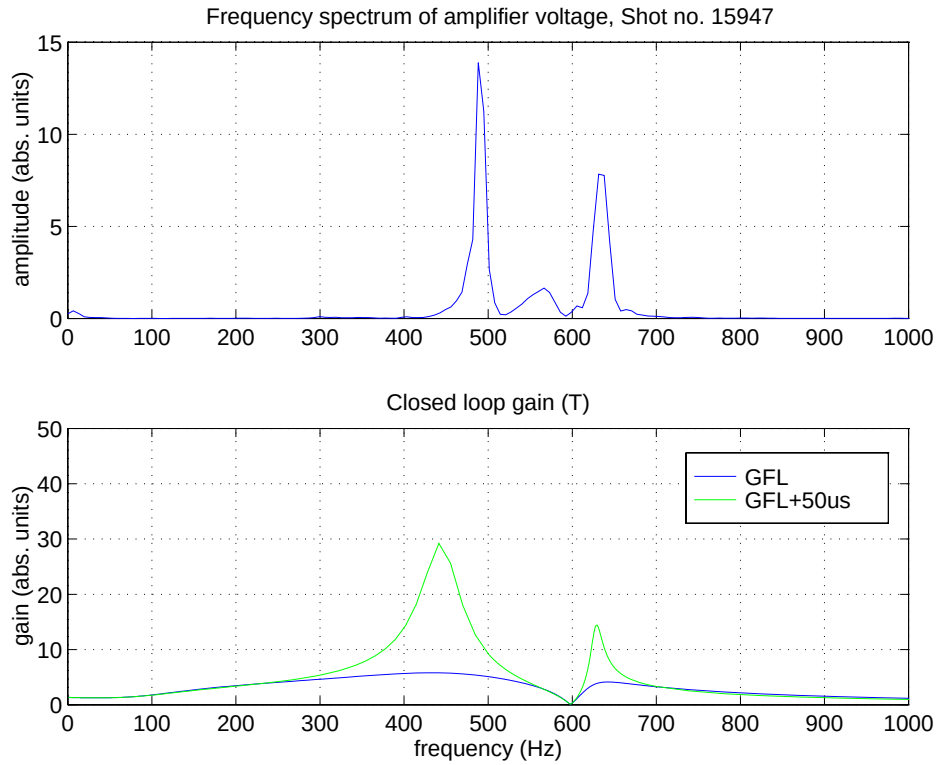


Figure 4.16 Bode plot of closed loop gain showing resonant peaks.

The effect of the controller DC gain on the steady state position error is observed in Fig. 4.17. The controller was designed to optimize the $\mathbf{H}_\infty$ constraint

$$\|\gamma KS\|_\infty<1$$

without constraints on *S* or *T*. A 600Hz notch filter was then combined with the controller. The resulting controller DC gain was 0.427 compared with a value of 1.214 obtained for $K_{H\infty}$. In Fig. 4.17 the ratio I_s/I_p increases from 1.56% at t=0.08s to 4.88% at t=0.11s. The plasma current is at the relatively low value ~65kA because part of the current drive apparatus was unavailable for the experiment. The reference position signal was at −2.1V during the time t>0.08s, but the Figure shows a steady upwards drift in position as the shape ratio increases. Loss of closed loop stability occurs at 0.11s. As observed in the previous chapter increasing the shape decreases the DC gain of the plant $|G_{FL}|$ and therefore the loop gain $|L|$ becomes smaller. The steady state error is a function of $|S|$ and therefore increases with shape. From the different models of the last chapter *L* is estimated to change from -8.61 at 3% I_s/I_p to -2.38 at 4.5% I_s/I_p. The corresponding change in $|S|$ is from 0.132 to 0.723 possibly explaining the drift in position during the shot. The constraint $\|W_3S\|_\infty<1$ is used to ensure that $|S|$ is small and to keep the steady state error tolerably small.

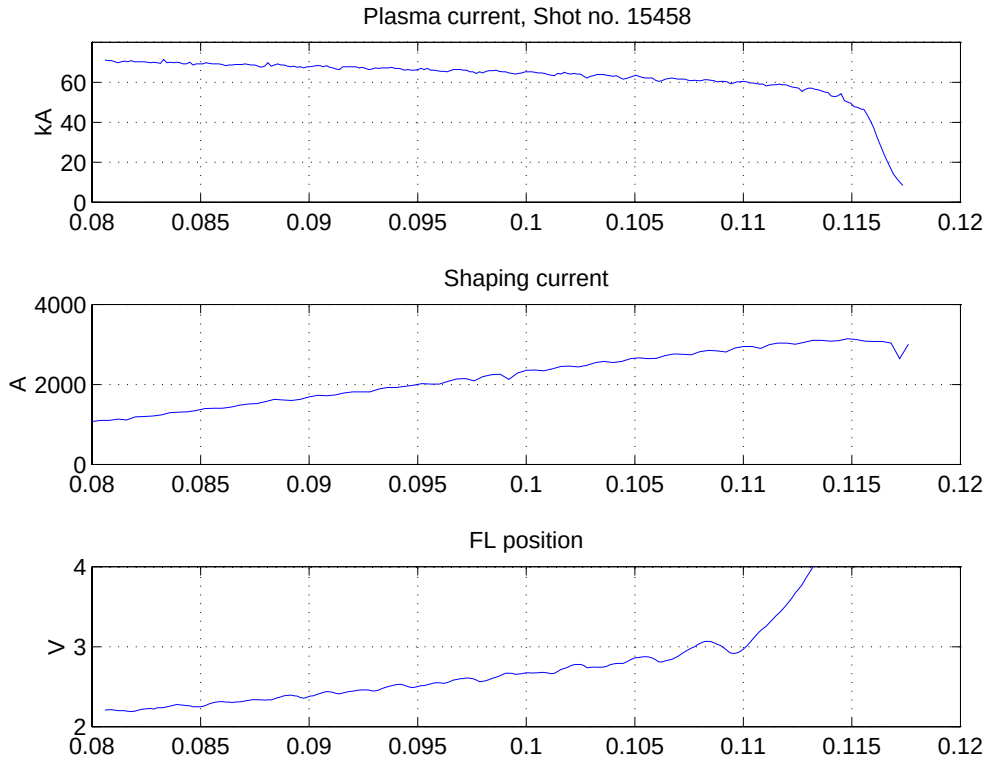


Figure 4.17 Drift in FL position as I_s/I_p increases.

4.5 SGPC

A widely used control strategy is Model Based Predictive Control (MBPC) [Clarke94]. The approach is based in the discrete time domain and the objective is the minimization of control activity and predicted output error over a finite time horizon. The basic method is to predict the future output of the plant as a sum of a free response (calculated from past known data) and a forced response (depending on future and known control actions). The predictions are calculated using a model of the plant. For convenience the plant model in this section is assumed to have the form

$$y(z^{-1}) = z^{-1}\frac{b(z^{-1})}{a(z^{-1})}u(z^{-1}) \qquad \textbf{(4.6)}$$

where $a(z^{-1})=1+\cdots+a_n z^{-n}$ and $b(z^{-1})=b_0+\cdots+b_{n-1}z^{-n+1}$. The plant model can be reformulated in terms of control increments $\Delta u_t \triangleq u_t - u_{t-1}$ by multiplying by $A(z^{-1}) \triangleq a(z^{-1})\Delta(z^{-1})$ where $\Delta(z^{-1}) \triangleq 1 - z^{-1}$

$$A(z^{-1})y(z^{-1}) = z^{-1}b(z^{-1})\Delta u(z^{-1})$$

The polynomial A has the form $A(z^{-1})=A_0+A_1z^{-1}+\cdots+A_{n+1}z^{-n-1}$ (A_0=1). At a sample instant t the plant output at the next sample $(\hat{y}_{t+1})$ can be predicted from the past values of the output $(y_t,\ldots,y_{t-n})$, the past control increments $(\Delta u_{t-1},\ldots,\Delta u_{t-n})$, and from assuming that the control increment to be implemented is known $(\Delta\hat{u}_t)$

$$\hat{y}_{t+1} = b_0\Delta\hat{u}_t + b_1\Delta u_{t-1} + \cdots + b_n\Delta u_{t-n} - A_1 y_t - \cdots - A_{n+1}y_{t-n}$$

Iterating forward to predict two and three samples ahead (assuming future values of $\Delta\hat{u}$ are known) gives

$$\begin{aligned} y_{t+2} + A_1 y_{t+1} &= b_0\Delta\hat{u}_{t+1} + b_1\Delta\hat{u}_t + b_2\Delta u_{t-1} + \cdots + b_n\Delta u_{t-n+1} - A_2 y_t - \cdots - A_{n+1}y_{t-n+1} \\ y_{t+3} + A_1 y_{t+2} + A_2 y_{t+1} &= b_0\Delta\hat{u}_{t+2} + \cdots + b_2\Delta\hat{u}_t + b_3\Delta u_{t-1} + \cdots + b_n\Delta u_{t-n+2} - A_3 y_t - \cdots - A_{n+1}y_{t-n+2} \end{aligned}$$

The equations can be stacked to predict a vector $\hat{\boldsymbol{y}}\in\mathbb{R}^{n_y}$ of the next n_y outputs from a vector of the past n+1 outputs $\boldsymbol{y}\in\mathbb{R}^{n+1}$, the past $n-1$ inputs $\Delta\boldsymbol{u}\in\mathbb{R}^{n-1}$ and assuming knowledge of the next n_u control increments $\Delta\hat{\boldsymbol{u}}\in\mathbb{R}^{n_u}$

$$C_A\hat{\boldsymbol{y}} = \Gamma_b\Delta\hat{\boldsymbol{u}} + H_b\Delta\boldsymbol{u} - H_A\boldsymbol{y}$$

Here the vectors are defined as

$$\hat{\boldsymbol{y}} \triangleq \begin{bmatrix} \hat{y}_{t+1} \\ \vdots \\ \hat{y}_{t+n_y} \end{bmatrix},\ \Delta\hat{\boldsymbol{u}} \triangleq \begin{bmatrix} \Delta\hat{u}_t \\ \vdots \\ \Delta\hat{u}_{t+n_u-1} \end{bmatrix},\ \boldsymbol{y} \triangleq \begin{bmatrix} y_t \\ \vdots \\ y_{t-n} \end{bmatrix},\ \text{and}\ \Delta\boldsymbol{u} \triangleq \begin{bmatrix} \Delta u_{t-1} \\ \vdots \\ \Delta\hat{u}_{t-n+1} \end{bmatrix}$$

The matrices are derived from the polynomials A and b and are defined as follows. For a polynomial $m(z^{-1})$ with n_m coefficients, $m(z^{-1}) \triangleq m_0 + m_1 z^{-1} + \cdots + m_{n_m-1} z^{-n_m+1}$ the matrix $C_m \in \mathbb{R}^{n_y \times n_y}$ is the Toeplitz matrix in which element i,j is m_{i-j}, $H_m \in \mathbb{R}^{n_y \times (n_m-1)}$ is the Hankel matrix in which element i,j is m_{i+j-1}, and Γ_m and M_m are defined by the first n_u and last $n_y - n_u$ columns of C_m. The structure of C_m and H_m are more clearly illustrated as

$$C_m = \begin{bmatrix} m_0 & 0 & 0 & \cdots & 0 & 0 \\ m_1 & m_0 & 0 & \cdots & 0 & 0 \\ \vdots & \vdots & \vdots & \vdots & \vdots & \vdots \\ m_{n_m-1} & m_{n_m-2} & m_{n_m-3} & \cdots & 0 & 0 \\ 0 & m_{n_m-1} & m_{n_m-2} & \cdots & 0 & 0 \\ \vdots & \vdots & \vdots & \vdots & \vdots & \vdots \\ 0 & 0 & 0 & \cdots & m_1 & m_0 \end{bmatrix}, \text{ and } H_m = \begin{bmatrix} m_1 & m_2 & \cdots & m_q \\ m_2 & m_3 & \cdots & 0 \\ \vdots & \vdots & \vdots & \vdots \\ m_{n_m-1} & 0 & \vdots & 0 \\ 0 & 0 & \vdots & 0 \\ \vdots & \vdots & \vdots & \vdots \end{bmatrix} \quad \textbf{(4.7)}$$

Vectors used later in this section are **0**, **1** and **e** which are respectively a vector of zeros, a vector of ones and the first standard basis vector; the dimensions of the vectors are appropriate to the context. The DC value of $m(z^{-1})$ will be indicated by $m(1)$.

MBPC has been applied to simulations of the JET vertical position control system [Zheng93] using the Generalized Predictive Control (GPC) algorithm. For GPC a performance index (J) is formulated

$$J = \|\hat{\boldsymbol{r}} - \hat{\boldsymbol{y}}\|_2^2 + \lambda \|\Delta \hat{\boldsymbol{u}}\|_2^2$$

The vector $\hat{\boldsymbol{r}} \in \mathbb{R}^{n_y}$ refers to the future reference output values. The parameters used to tune the controller are the output and control horizons n_y and n_u respectively and the weight λ penalizing the control activity. For the GPC algorithm [Clarke87], at each sample instant t the control signal vector $\Delta \hat{\boldsymbol{u}}$ is chosen to minimize the cost J. The first controller increment $(\Delta \hat{u}_t)$ is implemented and the procedure is then repeated at the next sample instant.

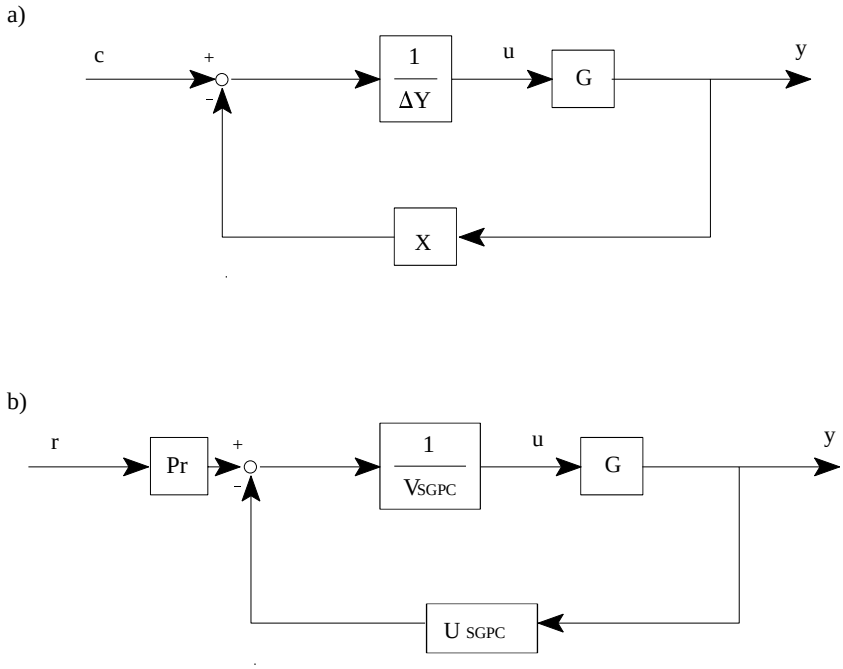


Figure 4.18 Scheme for designing SGPC controller.

Many MBPC algorithms, such as GPC, if not used carefully do not guarantee stability. One method of guaranteeing stability with MBPC is to subject the cost to end point constraints (such as requiring that the plant output and control signal do not change after a finite horizon). Developments of GPC have lead to algorithms which guarantee stability, including the Stable Generalized Predictive control (SGPC) [Kouvaritakis92b]. The method can also be used to separate the performance objective from robust stability. The controller is obtained in two steps. The optimal performance is calculated in the first step and then a second optimization is used to improve robust stability without affecting the performance.

The SGPC approach differs from GPC because the problem is changed from finding the control increments of an open loop plant to that of finding the input *c* to a closed loop system (Fig. 4.18a). The polynomials *X* and *Y* are any two polynomials which satisfy the Bezout identity

$$a(z^{-1})\Delta(z^{-1})X(z^{-1})+z^{-1}b(z^{-1})Y(z^{-1})=1 \qquad \textbf{(4.8)}$$

The closed loop is implemented with the X in the numerator of the feedback path and $Y\Delta$ in the denominator of the forward path.

The transfer functions from $c(z^{-1})$ to $u(z^{-1})$ and $y(z^{-1})$ are

$$\begin{aligned} y(z^{-1}) &= z^{-1}b(z^{-1})c(z^{-1}) \\ u(z^{-1}) &= A(z^{-1})c(z^{-1}) \end{aligned} \qquad \textbf{(4.9)}$$

For any arbitrary choice of $\hat{c}_{t+i}$ $(0\le i<n_c)$ and if $\hat{c}_{t+i}=\hat{c}_{\infty}$ $(i\ge n_c)$ where

$$\hat{c}_{\infty}\triangleq\frac{\hat{r}_{t+ny}}{b(1)}$$

then the plant output and control increment satisfy the end point constraints

$$\begin{aligned} \hat{y}_{t+i} &= \hat{r}_{t+n_y} \quad (\forall i>n_y,\ n_y=n_c+n-1) \\ \Delta\hat{u}_{t+i} &= 0 \quad (\forall i\ge n_u,\ n_u=n_c+n+1) \end{aligned}$$

Thus SGPC is an efficient method of introducing end point constraints into the GPC cost and therefore guarantees stability. The future values of $\hat{\boldsymbol{y}}\in\mathbb{R}^{n_y}$ and $\Delta\hat{\boldsymbol{u}}\in\mathbb{R}^{n_u}$ can be calculated from

$$\begin{aligned} \hat{\boldsymbol{y}} &= \Gamma_b\hat{\boldsymbol{c}}+M_b\mathbf{1}c_{\infty}-P_1\boldsymbol{y}-P_2\Delta\boldsymbol{u} \\ \Delta\hat{\boldsymbol{u}} &= \Gamma_A\hat{\boldsymbol{c}}+M_A\mathbf{1}c_{\infty}-P_3\boldsymbol{y}-P_4\Delta\boldsymbol{u} \end{aligned}$$

where

$$
\begin{aligned}
P_1 &= C_b H_{z^{-1}Y} + C_X H_A \\
P_2 &= C_b H_X - C_X H_b \\
P_3 &= C_A H_{z^{-1}Y} + C_{z^{-1}Y} H_A \\
P_4 &= C_A H_X + C_{z^{-1}Y} H_b
\end{aligned}
$$

The optimization problem is now to choose the optimal $\hat{\boldsymbol{c}} \in \mathbb{R}^{n_c}$ to minimize the GPC cost (J) where

$$\hat{\boldsymbol{c}} = [\hat{c}_t \;\; \hat{c}_{t+1} \;\; \cdots \;\; c_{t+n_c-1}]^{\mathrm{T}}$$

The SGPC control law is implemented at sample instant t by using the first element $\hat{c}_t$ to find $\Delta\hat{u}_t$ and implementing the increment. The process is then repeated at the next sample instant. The optimal value $\hat{c}_t$ can be calculated recursively from past values of input and output

$$\hat{c}_t = P_r \hat{\boldsymbol{r}} + S_1 \boldsymbol{y} + S_2 \Delta \boldsymbol{u}$$

where

$$
\begin{aligned}
S_1 &= P(\Gamma_b^{\mathrm{T}} P_1 + \lambda \Gamma_A^{\mathrm{T}} P_3) \\
S_2 &= P(\Gamma_b^{\mathrm{T}} P_2 + \lambda \Gamma_A^{\mathrm{T}} P_4) \\
P &= \boldsymbol{e}^{\mathrm{T}} (\Gamma_b^{\mathrm{T}} \Gamma_b + \lambda \Gamma_A^{\mathrm{T}} \Gamma_A)^{-1} \\
P_r &= P\Gamma_b^{\mathrm{T}} - [\boldsymbol{0}, P(\Gamma_b^{\mathrm{T}} M_b \boldsymbol{1} + \lambda \Gamma_A^{\mathrm{T}} M_A \boldsymbol{1})/b(1)]
\end{aligned}
$$

The coefficients of the polynomials $U(z^{-1})$ and $V(z^{-1})$ can be obtained from the coefficients of the vectors $[-S_1 + \boldsymbol{e}^{\mathrm{T}} P_3]$ and $[1, -S_2 + \boldsymbol{e}^{\mathrm{T}} P_4]$ respectively. This gives the closed loop pole polynomial

$$P_c = a(z^{-1})\Delta(z^{-1})V(z^{-1}) + z^{-1}b(z^{-1})U(z^{-1}) \quad \textbf{(4.10)}$$

The resulting closed loop transfer functions are

$$y(z^{-1}) = \frac{z^{-1}b(z^{-1})P_r(z^{-1})}{P_c(z^{-1})}r(z^{-1})$$

$$\Delta u(z^{-1}) = \frac{A(z^{-1})P_r(z^{-1})}{P_c(z^{-1})}r(z^{-1})$$

The controller is conveniently implemented using the scheme of Fig. 4.18b where U_{SGPC} and V_{SGPC} are any pair of polynomials such that the closed loop pole polynomial is P_c. The polynomials U_{SGPC} and V_{SGPC} can be obtained from the particular solutions U and V satisfying the Diophantine equation (4.10)

$$U_{SGPC} = U + aQ$$

$$V_{SGPC} = V + z^{-1}bQ$$

where $Q \in \mathbb{R}\mathbf{H}_\infty$ is the Youla parameter. Note that the integrator $(\Delta(z^{-1}))$ need not be included in the denominator of the controller provided that the closed pole polynomial is P_c.

The SGPC algorithm guarantees stability but can have poor robustness properties. The end point constraints impose deadbeat control and therefore the algorithm produces systems with high control activity at the expense of robust stability. Heuristic arguments suggest that controllers with lower control activity can have improved robustness properties and this motivates the use of the CaSC (Cautious Stable predictive Control) algorithm based on SGPC [Gossner95].

The SGPC algorithm applies the signal c to the closed loop system obtained after solving the Bezout identity of Equation (4.8). This leads to the deadbeat closed loop responses in (4.9). This in turn leads to the end point constraint which are a sufficient

but not necessary condition for stability. Instead of (4.8) a condition which is both necessary and sufficient is the Diophantine equation

$$a(z^{-1})\Delta(z^{-1})Y(z^{-1})+z^{-1}b(z^{-1})X(z^{-1})=a^{-}(z^{-1})b^{-}(z^{-1})$$

Here the plant numerator and denominator polynomials are split into two parts $a=a^{+}a^{-}$ and $b=b^{+}b^{-}$ where the roots of a^{+} and b^{+} lie outside or on the unit disc and the roots of a^{-} and b^{-} lie strictly inside the unit disc. The prediction equations for the plant are then

$$y(z^{-1}) = \frac{a^{+}(z^{-1})}{b^{-}(z^{-1})}c(z^{-1})$$

$$u(z^{-1}) = \frac{z^{-1}b^{+}(z^{-1})}{a^{-}(z^{-1})}c(z^{-1})$$

and they are stable for any $c(z^{-1})\in\mathbb{R}\mathbf{H}_{\infty}$. The plant output and control signal no longer converge after a finite number of samples and therefore the sufficient stability results of SGPC do not apply. However asymptotic convergence is all that is required for necessary and sufficient conditions of stability and this is obtained using the CaSC controller. The CaSC performance index can be formulated in terms of an infinite sum

$$J=\sum_{i=1}^{\infty}(\hat{r}_{t+i}-\hat{y}_{t+i})^2+\lambda\sum_{i=0}^{\infty}\Delta\hat{u}_{t+i}^2 \qquad \textbf{(4.11)}$$

If $\hat{c}_{t+i}$ is fixed for all $i\geq n_c$ at

$$\hat{c}_{\infty}=\frac{r_{t+n_y}a^{-}(1)}{b^{+}(1)}$$

(where $n_y = n_{b^+} + n_c$) then the minimization of the CaSC performance index with respect to $\hat{\boldsymbol{c}}$ results in a stabilizing controller for all values of n_c. The CaSC controller can be obtained from the solutions of the Diophantine equation

$$a(z^{-1})V(z^{-1}) + z^{-1}b(z^{-1})U(z^{-1}) = P_c \qquad \textbf{(4.12)}$$

where the following matrices determine the closed loop pole polynomial and the prefilter

$$\begin{aligned}
S_1 &= P(\Gamma_{b^+}^{\mathrm{T}}\Gamma_{1/a^-}^{\mathrm{T}}\Gamma_{1/a^-}P_1 + \lambda\Gamma_{A^+}^{\mathrm{T}}\Gamma_{1/b^+}^{\mathrm{T}}\Gamma_{b^+}^{\mathrm{T}}P_3)\\
S_2 &= P(\Gamma_{b^+}^{\mathrm{T}}\Gamma_{1/a^-}^{\mathrm{T}}\Gamma_{1/a^-}P_2 + \lambda\Gamma_{A^+}^{\mathrm{T}}\Gamma_{1/b^+}^{\mathrm{T}}\Gamma_{b^+}^{\mathrm{T}}P_4)\\
P &= \boldsymbol{e}^{\mathrm{T}}(\Gamma_{b^+}^{\mathrm{T}}\Gamma_{1/a^-}^{\mathrm{T}}\Gamma_{1/a^-}\Gamma_{b^+} + \Gamma_{A^+}^{\mathrm{T}}\Gamma_{1/b^-}^{\mathrm{T}}\Gamma_{1/b^-}\Gamma_{A^+})\\
P_r &= P\Gamma_{b^+}^{\mathrm{T}}\Gamma_{1/a^-}^{\mathrm{T}}\Gamma_{1/a^-} - \left[\mathbf{0},\ P(\Gamma_{b^+}^{\mathrm{T}}\Gamma_{1/a^-}^{\mathrm{T}}\Gamma_{1/a^-}M_{b^+}\mathbf{1} + \lambda\Gamma_{A^+}^{\mathrm{T}}\Gamma_{1/b^-}^{\mathrm{T}}\Gamma_{1/b^-}M_{A^+}\mathbf{1})\frac{a^-(1)}{b^+(1)}\right]
\end{aligned} \qquad \textbf{(4.13)}$$

The matrices Γ_{1/a^-} and Γ_{1/b^-} have an infinite number of rows (the first column of each matrix contains the impulse response of $1/a^-(z^{-1})$ and $1/b^-(z^{-1})$ respectively). However $\Gamma_{1/a^-}^{\mathrm{T}}\Gamma_{1/a^-} \in \mathbb{R}^{(n_{b^+}+n_c+1)\times(n_{b^+}+n_c+1)}$ and $\Gamma_{1/b^-}^{\mathrm{T}}\Gamma_{1/b^-} \in \mathbb{R}^{(n_{a^+}+n_c+1)\times(n_{a^+}+n_c+1)}$ are finite dimensional and can be calculated [Rossiter96]. The controller is implemented as in Fig. 4.18b with $U_{SGPC}=U$ and $V_{SGPC}=V$. The structure of the controller allows the robust stability property of the loop to be changed without affecting performance. Note that the closed loop transfer functions from r to u and y in Fig. 4.18b are

$$\frac{y(z^{-1})}{r(z^{-1})} = \frac{z^{-1}b(z^{-1})P_r(z^{-1})}{P_c(z^{-1})}$$

$$\frac{u(z^{-1})}{r(z^{-1})} = \frac{a(z^{-1})P_r(z^{-1})}{P_c(z^{-1})}$$

where P_c is the optimal closed loop pole polynomial for the CaSC performance index. Two particular solutions U and V to the Diophantine equation (4.12) can be obtained from the coefficients of the vectors $[-S_1 + \boldsymbol{e}^{\mathrm{T}}P_3]$ and $[1, -S_2 + \boldsymbol{e}^{\mathrm{T}}P_4]$ respectively.

Any pair of solutions U and V to the Diophantine equation (4.12) will produce the optimal closed loop pole polynomial P_c. Given one pair of solutions U and V to (4.12),

the entire set of controllers U_{SGPC} and V_{SGPC}, which if implemented as in Fig. 4.18 give the optimal CaSC performance, are

$$\begin{aligned} U_{SGPC} &= U+aQ \\ V_{SGPC} &= V-z^{-1}bQ \end{aligned} \tag{4.14}$$

where $Q \in \mathbb{R}\mathbf{H}_\infty$ parameterizes the set. The CaSC performance index of the loop is independent of Q. However the robust stability properties of the loop do depend on Q. Using the additive model of uncertainty $G' \in \{G+W\Delta_u;\ W \in \mathbb{R}\mathbf{H}_\infty\}$ where Δ_u is any transfer function such that G' and G have the same number of unstable poles, then the closed loop is stable for any Δ_u in the set $\|\Delta_u\|_\infty<1$ if and only if

$$\|WKS\|_\infty<1$$

(provided the nominal closed loop is stable). Rewriting *WKS* gives

$$WKS=\frac{Wa\Delta_u(U+aQ)}{P_c} \tag{4.15}$$

and the parameter Q can be used to minimize *WKS* without affecting the performance. Minimizing *WKS* over a set of stable transfer functions Q forms a standard $\mathbf{H}_\infty$ optimization problem. One convenient method of solving the problem is to use a polynomial $Q(z^{-1})$

$$Q(z^{-1})=\sum_{i=0}^{n_Q} q_i z^{-1}$$

where n_Q is chosen to be the order of the polynomial and q_i are the coefficients. The optimal choice of Q can be chosen using Lawson's weighted least squares algorithm.

A CaSC controller was designed for the COMPASS-D vertical position control system. The discrete time model of the plant was obtained in two parts. The first part is the discrete time model of the plasma system identified in Chapter 3. The second part was a discrete time approximation to the control coil and amplifier model

$$G_2(s)=\frac{G_s K_{DSP} K_a p_a \bar{p}_a}{(sL_c+R_c)(s-p_a)(s-\bar{p}_a)}$$

As is the case with the $\mathbf{H}_\infty$ the high frequency poles and time delays are approximated as a two sample delay in the plant. The resulting plant model $G(z^{-1})=g_n(z^{-1})/g_d(z^{-1})$ is 6th order. A second order notch filter is also introduced into the loop to attenuate 600Hz, and has the transfer function $f_n(z^{-1})/f_d(z^{-1})$. The plant model is cast in the form of (4.6), with $zb=g_n f_n$ and $a=g_d f_d$. The order of a is n=8. Polynomials a^- and b^- are also calculated to contain the roots which are strictly inside the unit disc of the polynomials g_d and g_n respectively. The zeros of the notch numerator and denominator all lie inside the unit disc but are close to the unit circle. Resonant poles are not desired in the closed loop transfer function and therefore the roots of f_n and f_d are not included in a^- and b^-. The prediction matrices $H_\bullet$, $\Gamma_\bullet$ and $M_\bullet$ are calculated with the structures indicated in (4.7) and the solutions to the CaSC cost (4.11) are obtained as in (4.13). The weights chosen for the cost were λ=1000 and n_c=50. They were chosen to heavily penalize control activity (λ) and to allow slow response times with a long control horizon (n_c). Heuristic arguments suggest that controllers that are less highly tuned can be made to have good robust stability properties. The optimal closed loop pole polynomial can be calculated and solutions for U and V are obtained for the Diophantine equation (4.12).

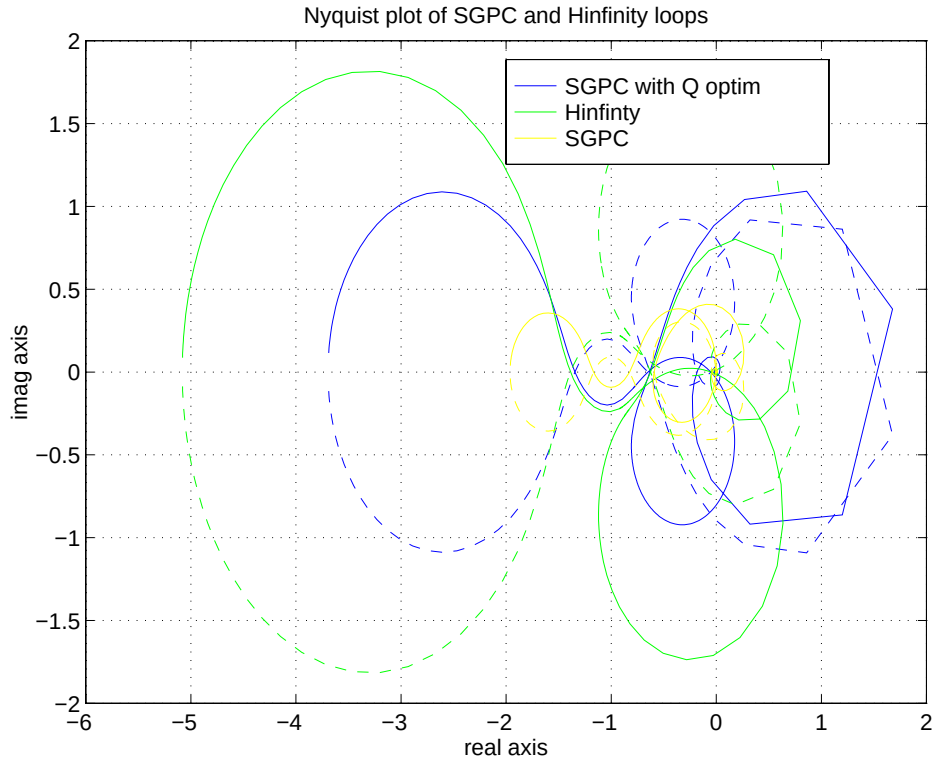


Figure 4.19 Nyquist plot of loop gain with SGPC controller with *Q* optimization (K_{SGPC}). For comparison the loop gain with the $\mathbf{H}_\infty$ controller ($K_{H\infty}$) and the SGPC controller without *Q* optimization.

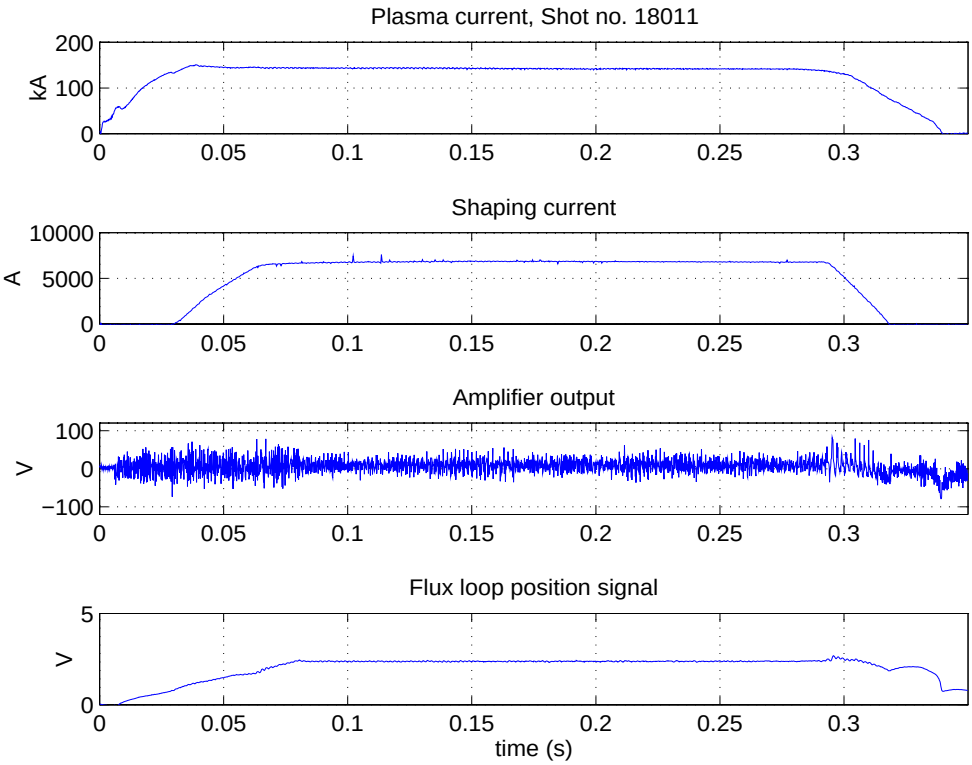


Figure 4.20 Result of using CaSC controller (K_{SGPC}).

The next step is to improve the robustness properties of the loop. The robustness weight (W) was chosen to ensure an adequate stability margin at 295Hz which is approximately the gain crossover frequency. A large penalty was also placed at 600Hz to ensure the effect of the notch filter was not reduced. Lawson's weighted least squares algorithm was used to find the optimal Q of order n_Q=7 minimizing $\|WKS\|_\infty$ in (4.15). The controller for COMPASS–D was then obtained from (4.14). The calculations were performed using a Matlab toolbox written by J.R. Gossner, Department of Engineering Science, University of Oxford.

The controller was tested on COMPASS–D with a conventional implementation (Fig. 4.4). A prefilter is not required because the reference signal is constant during the flattop period of the shot and $K_{H\infty}$ was replaced by

$$K_{SGPC}(z^{-1}) = \frac{f_n(z^{-1})U_{SGPC}(z^{-1})}{f_d(z^{-1})V_{SGPC}(z^{-1})}$$

The coefficients of K_{SGPC} are presented in Table 4.2. The resulting controller has similar loop gain properties as the $\mathbf{H}_\infty$ controller (Fig. 4.19). Testing the controller on COMPASS–D proved that it stabilized the plasma vertical position using only external position measurements (Fig. 4.20) and attenuated the 600Hz noise at the amplifier output (Fig. 4.11).

Table 4.2 Coefficients of CaSC controller transfer function.

power of z	numerator coefficient	denominator coefficient
z^{0}	2.868719403385606e+002	1.000000000000000e+000
z^{-1}	-1.061924660393594e+003	-2.569860693920740e+000
z^{-2}	1.370665204973962e+003	2.261869554950982e+000
z^{-3}	-6.286945344434714e+002	-6.672122101187714e-001
z^{-4}	4.475921496641483e+000	-2.113055569426964e-002
z^{-5}	5.512162857297434e+001	-9.878276497609650e-002
z^{-6}	-2.068899293022965e+002	-1.355502008869090e-002
z^{-7}	2.998508400813154e+002	1.756814147803599e-001
z^{-8}	-1.199446401611803e+002	2.994236294726640e-002
z^{-9}	-1.237060032815165e+001	-2.454201277259068e-002
z^{-10}	1.656225194472967e+001	-6.147201057106934e-002
z^{-11}	-4.872351907566882e+000	-3.001068133635350e-002
z^{-12}	1.156228384066670e+000	2.358792311778699e-002
z^{-13}	0	3.760418727337588e-003

4.6 Conclusions

The COMPASS–D analogue P+D controller performs satisfactorily in practice, with the exception of large 600Hz oscillations and occasional loss of control when disturbed by large separated ELMs. The typical SND plasmas used on COMPASS–D have instability growth rates of order 2500 s^{-1}. The success of the P+D controller is due in part to the use of internal magnetic pickup coils to provide the derivative part of the control signal. External measurements are shielded by the vessel wall which has a radial field penetration time constant estimated in the range 420μs to 670μs. The wall introduces a phase delay into the position signals. The phase delay reduces the phase margins of the control system when only external measurements are used in the loop.

Internal position measurements will not be available on ITER because of the harsh reactor conditions. Therefore closed loop stability may be more difficult to achieve with a simple P+D controller. The 600Hz oscillations on COMPASS–D are also observed on JET and it is important to reduce the effect of this noise on power amplifier output signals. A notch filter would introduce phase lag below 600Hz and would therefore reduce the phase margins of the loop.

Higher order controller potentially offer advantages over simple P+D controllers but are more difficult to design. Two different design approaches were used to develop high order controllers with the objectives of stabilizing the plasma position using only external measurements and attenuating the 600Hz oscillations at the amplifier output. Both approaches ($\mathbf{H}_\infty$ and SGPC) resulted in 13th order controllers with similar loop gain properties and both were tested on COMPASS–D. The two controllers stabilized the plasma position achieving the two objectives, neither of which were possible with a simple P+D controller. The results on COMPASS–D demonstrate that compared with simple P+D controllers high order controllers offer improvements to the performance and stability of the vertical position control loop. The results also demonstrate the importance of considering the effect of experimentally observed noise and disturbances when formulating the controller objectives.

Measurements of the loop gain margin and phase crossover frequencies on COMPASS–D were compared to predicted values and were found to be in good agreement. The results indicated the validity of using system identification to model the open loop plasma position system. Other experiments using controllers with a low DC gain showed that the position error increases as the shape (I_s/I_p) increases. This is consistent with predictions because the DC gain of the plasma model decreases with I_s/I_p. A small phase delay discrepancy (of order 50μs) was observed in the gain margin estimates. This small discrepancy was also apparent in the comparison of predicted and observed behaviour of an initial experiment. The plasma position resonated at two different frequencies and whilst the nominal closed loop model does not predicted a resonant frequency response, a model including a small phase delay matches the resonant behaviour of the experiment.

5 Peak Impulse Response

5.1 Introduction

Large separated ELMs on COMPASS–D (Fig. 2.21) produce an impulse like response in the vertical position control system. These disturbances can sometimes lead to disruptions because large voltage swings on the amplifiers cause saturation and loss of control. A first step in reducing the peak response to ELMs would be to minimize the peak of the impulse response.

This chapter examines the use of optimization techniques to calculate the optimal performance that can be achieved with linear controllers. The results are useful in determining the limits of performance and therefore providing a benchmark against which other controllers can be compared.

5.2 Optimal solution

In this section we find a theoretically optimal controller which minimizes the peak of the impulse response. Dahleh and Pearson [Dahleh88] have developed a method for deriving the discrete time optimal controller minimizing the maximum magnitude of the response for a fixed input. For an arbitrary plant, the optimal response is found from the solution of a linear programming (LP) problem with a finite number of variables and a constraint involving the sum of a series of an infinite number of terms. The resulting optimal controller is of infinite order. A restricted order optimal controller can be found if the series is truncated. For a restricted class of plants which includes the COMPASS–D model the LP problem can be solved analytically, as is shown below.

In this section the Z-transform of a time-sequence $\{f_i\}$ is defined as in [Dahleh88]

$$F(z)=\sum_{i=0}^{\infty} f_i z^{i}$$

Note that this is defined in terms of z and not the more usual z^{-1} which means that $F(z)$ is unstable if it has any poles inside the unit disc. The plant transfer function is represented by $G(z)$ and the controller as $K(z)$. Letting t_i represent the impulse response of the closed loop transfer function $T(z)\triangleq G(z)K(z)(1+G(z)K(z))^{-1}$ and defining the peak of the impulse response $\|t_i\|_\infty \triangleq \max_i |t_i|$, then the optimal cost is

$$\mu_* = \min_K \{\|t_i\|_\infty : \ K \ \text{stabilizes} \ G\} \qquad \textbf{(5.1)}$$

The result for COMPASS–D type plants is presented below.

Proposition 5.1

Consider a plant with a single unstable pole at a, m zeros at the origin and no other poles or zeros inside the unit disc.

a) The optimal cost is

$$\mu_* = \frac{1-|a|}{|a|^m}.$$

The optimal closed loop response is a step of height μ_* after a time delay of m samples as shown in Fig. 5.1a. The order of the controller is infinite.

b) Consider the case when the order of the closed loop response is restricted to n where $n \geq n_n + n_d + 1$ and n_n and n_d are the orders of the plant numerator and denominator respectively. Then the restricted order optimal cost is

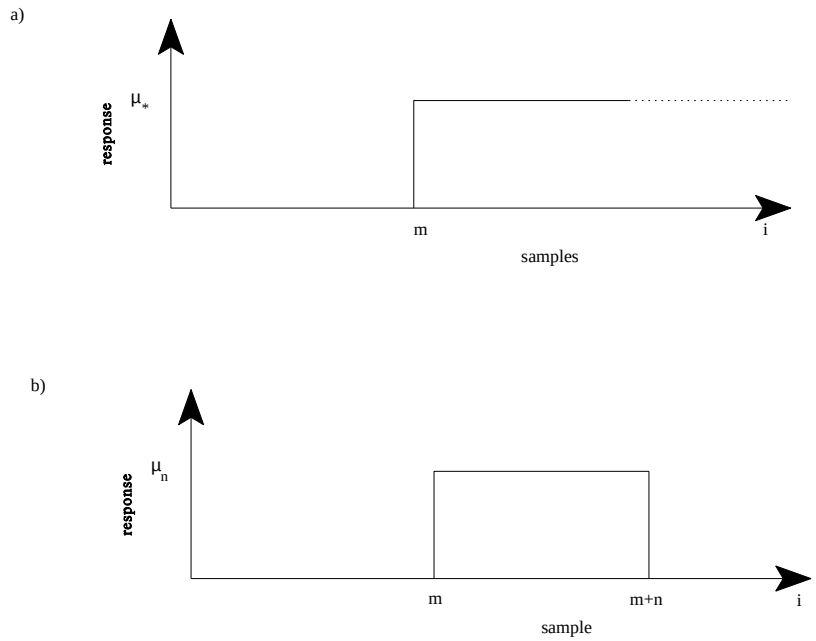


Figure 5.1 Closed loop response of optimal and suboptimal peak response controllers for COMPASS–D type plants.

$$\mu_n = \frac{1-|a|}{|a|^m - |a|^{n+1}}.$$

The resulting response is a pulse as shown in Fig. 5.1b. The controller order is $n_d+n-m-1$.

Proof of proposition 5.1

This proof closely follows the approach of Dahleh and Pearson [Dahleh88] and involves parameterizing all stabilizing controllers and then formulating an LP problem. Simplifications are then made for the class of plants under consideration. The proof is presented for the optimal case (Proposition 5.1 case a)) and is then followed by a discussion for case b).

The plant model $G(z)$ can be factorized as $G(z)=N(z)/D(z)$ (N is the numerator polynomial including m zeros at the origin and D is the denominator polynomial including a zero at a). This allows the controller $K(z)$ to be written as

$$K=\frac{X+DQ}{Y-NQ}$$

where $Q\in\mathbb{R}\mathbf{H}_\infty$. The polynomial Q is the Youla parameter and X and Y are coprime polynomials satisfying $NX+DY=1$. The closed loop transfer function $T(z)$ can be written as

$$T(z)=V-UQ$$

where $V=NX$ and $U=-ND$. The problem then is to find the stable transfer function Q which minimizes the peak of the impulse response of $T(z)$

$$\mu_*=\min_Q\|t_i\|_\infty.$$

Defining $F\triangleq UQ$ then F can be any arbitrary stable rational function provided that F contains the same zeros inside the unit disc as U, i.e.

$$\begin{aligned}F(a)&=0\\F(0)&=0\\F'(0)&=0\\&\vdots\\F^{(m)}(0)&=0\end{aligned}$$

The impulse response $\{f_i\}$ of $F(z)$ can be represented by the sequence f and the constraint on $F(z)$ can be formulated as

$$
\begin{aligned}
\langle f,a_r\rangle &= 0, \quad a_r = (1,a,a^2,a^3,\ldots) \\
\langle f,e_1\rangle &= 0, \quad e_1 = (1,0,0,0,\ldots) \\
\langle f,e_2\rangle &= 0, \quad e_2 = (0,1,0,0,\ldots) \\
&\vdots \\
\langle f,e_m\rangle &= 0, \quad e_m = (0,0,\ldots,0,1,0,\ldots)
\end{aligned}
\tag{5.2}
$$

where $\langle x,y\rangle \triangleq \sum_{i=0}^{\infty} x_i y_i$.

Define the norm $\|x_i\|_1 \triangleq \sum_{i=0}^{\infty} |x_i|$ and let the set

$$BS \triangleq \{x \in \text{span}(e_1,\ldots,e_m,a_r),\ \|x\|_1 \le 1\}.$$

Using the duality theorem [Luenberger69] the problem becomes

$$\mu_* = \max_{r \in BS} \langle r,v\rangle. \tag{5.3}$$

The sequence $r \in BS$ has the structure

$$r = \alpha_1 e_1 + \alpha_2 e_2 + \cdots + \alpha_m e_m + \alpha_{m+1} a_r$$

where α_i are real numbers to be determined, i.e.

$$
\begin{aligned}
r_0 &= \alpha_1 + \alpha_{m+1} \\
r_1 &= \alpha_2 + \alpha_{m+1} a \\
r_i &= \alpha_{i+1} + \alpha_{m+1} a^i, \quad 0 \le i < m \\
r_j &= \alpha_{m+1} a^j, \qquad j \ge m
\end{aligned}
$$

and

$$\langle r,v\rangle = \alpha_1 v_0 + \alpha_2 v_1 + \cdots + \alpha_m v_{m-1} + \alpha_{m+1} V(a).$$

Equation (5.3) is a linear programming problem with a finite number of variables and a constraint involving the sum of an infinite number of terms.

Now since N has m zeros at the origin and $V=NX$ then

$$V(z)=v_m z^m+v_{m+1}z^{m+1}+\cdots$$

because $v_0=v_1=\cdots=v_{m-1}=0$. Since $D(a)Y(a)=0$ then $V(a)=N(a)X(a)=1$. The LP problem is now

$$\mu_*=\max_{\alpha_i}\alpha_{m+1}$$

subject to the constraint $\|r\|_1\le 1$ which can be rewritten as

$$|\alpha_1+\alpha_{m+1}|+|\alpha_2+\alpha_{m+1}a|+\cdots+|\alpha_m+\alpha_{m+1}a^m|+\alpha_{m+1}\sum_{i=m+1}^{\infty}|a^i|\le 1.$$

By inspection the maximum value for α_{m+1} can be achieved when

$$\begin{aligned}\alpha_1 &= -\alpha_{m+1}\\ \alpha_2 &= -\alpha_{m+1}a\\ &\vdots\\ \alpha_m &= -\alpha_{m+1}a^{m-1}\end{aligned}$$

and

$$\alpha_{m+1}\sum_{i=m}^{\infty}|a^i|=1$$

The resulting μ_* is

$$\mu_* = \frac{1}{\sum_{i=m}^{\infty} |a^i|} = \frac{1-|a|}{|a|^m}.$$

Since $t=v-f$ and f is constrained by the equations (5.2), then

$$\langle v-t, e_1\rangle = 0, \ldots, \langle v-t, e_m\rangle = 0, \langle v-t, a_r\rangle = 0$$

i.e.

$$v_0 - t_0 = 0,\ v_1 - t_1 = 0,\ \ldots,\ v_{m-1} - t_{m-1} = 0,\ \sum_{i=0}^{\infty} (v_i - t_i) a^i = 0.$$

It was noted earlier that $v_0 = v_1 = \cdots = v_{m-1} = 0$ which implies that $t_0 = t_1 = \cdots = t_{m-1} = 0$. The alignment condition (see [Dahleh88] theorem 4) implies that $|t_i| = \mu_*$ whenever the optimal $r_i^* \neq 0$. The condition also implies that $T(a)=V(a)$ which is satisfied if

$$t_i^* = \begin{cases} 0 & 0 \le i < m-1 \\ \mu_* & m \le i \end{cases}$$

The optimal closed loop response is a step after a delay of m samples with magnitude μ_* (Fig. 5.1a). The controller can be derived by deconvolving the closed loop transfer function

$$K = G^{-1} \frac{T}{1-T}.$$

This concludes the proof for the optimal case.

If the impulse response of T is restricted to be of nth order (i.e. the system is deadbeat) then the denominator of T must equal one and the numerator is nth order. In this case, assuming n is greater than the order of V, then UQ must be a polynomial of order n.

For a deadbeat response any denominator of Q must cancel completely with zeros in U. Allowing Q to cancel all the zeros of U outside the unit disc results in $F = z^{m}(z-a)Q_n$ where Q_n is any polynomial of order n-m-1. This result can be used to formulate an LP problem directly [Moore88] but we continue the derivation as for case a). Restricting the order of the sequence $\{t_i\}$ to n means restricting the order of $\{f_i\}$, and consequently $\{r_i\}$, to order n. The LP cost in (5.3) is unchanged but the constraint $\|r\|_1 \le 1$ contains only n terms. The values for α_i are unchanged except that $\alpha_{m+1} = \sum_{i=m}^{n} |a^{i}| = 1$. Therefore the restricted order optimal solution μ_n is

$$\mu_n = \frac{1}{\sum_{i=m}^{n} |a^{i}|} = \frac{1-|a|}{|a|^m - |a|^{n+1}}.$$

This solution for the truncated series represents the optimal response for a given fixed order deadbeat controller. The order of the controller is n_d+n-m-1 where n_d is the order of $D(z)$. For the restricted order case the response t^n is

$$t_i^n = \begin{cases} 0 & 0 \le i < m-1 \\ \mu_n & m \le i \le n \\ 0 & i > n \end{cases}$$

The response is a pulse with magnitude μ_n which starts at i=m and has a width of n samples (Fig. 5.1b).

Note that the performance does not depend on any of the stable poles or zeros outside the unit disc of the plant. These are cancelled by the controller. The proofs are supplied above. The controller can be synthesized by deconvolving it from the closed loop transfer function. Figure 5.3 contains plots of μ_* against a for different values of m. It shows clearly that the optimal peak response increases as the time constant of the unstable pole decreases. For COMPASS–D this implies that the optimal performance is worse for plasmas with higher elongations. It also shows that the optimal cost increases with m. The plot of μ_n against n (Fig. 5.2) shows that allowing the order of the response to increase improves the performance of the controller. In summary,

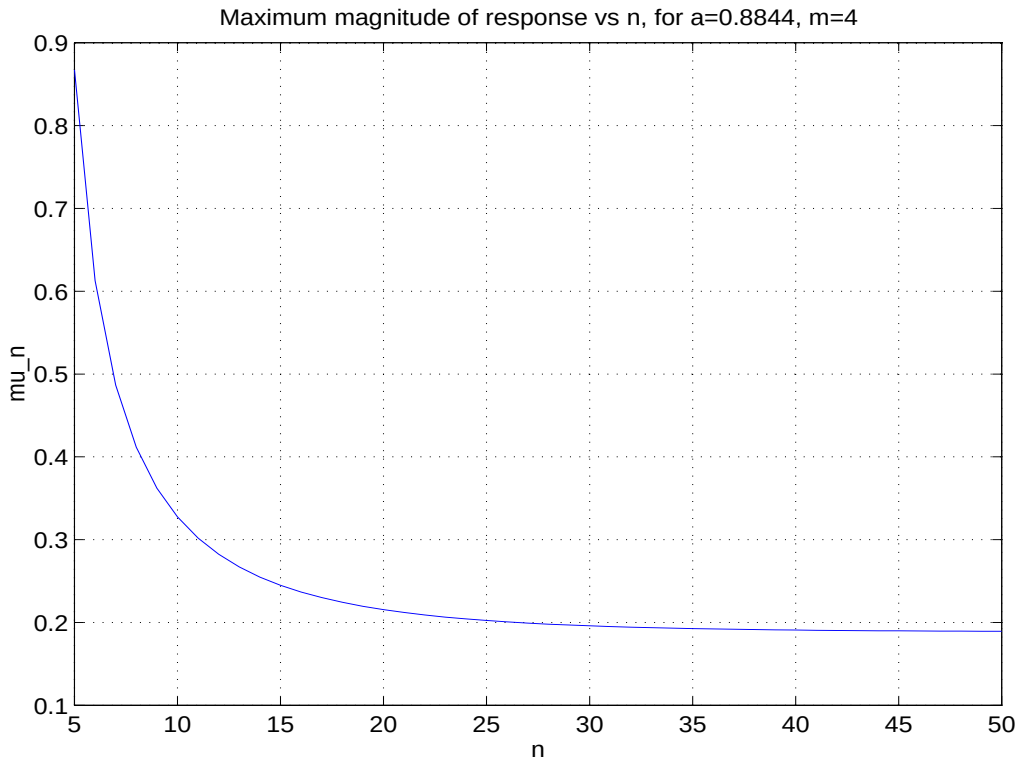


Figure 5.2 Suboptimal peak against order.

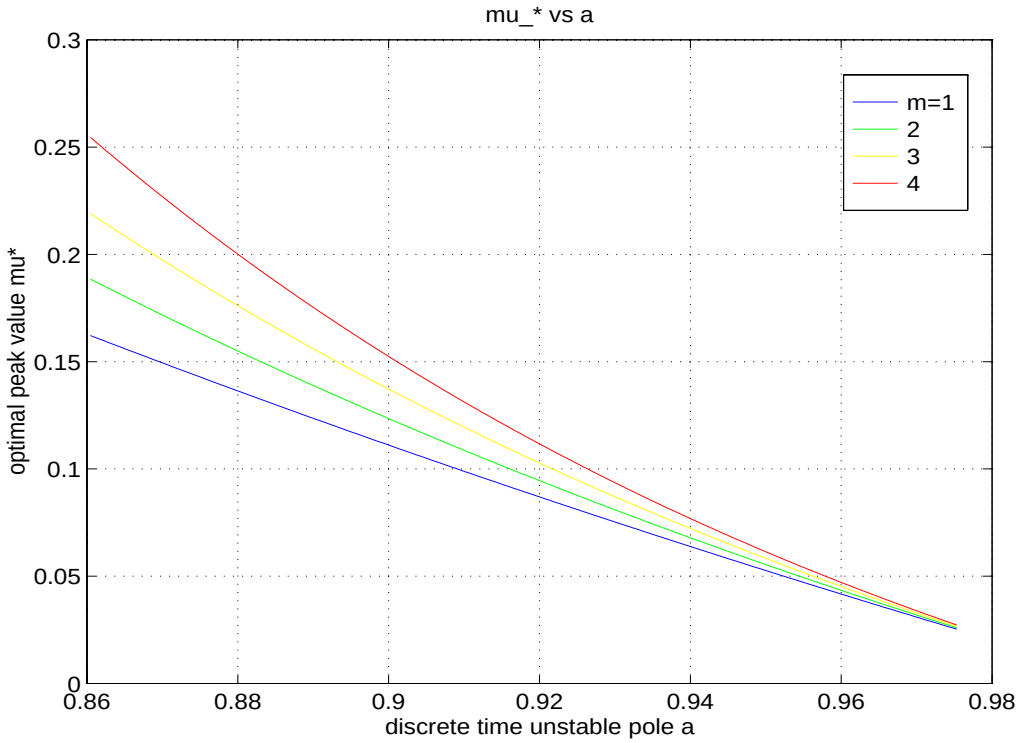


Figure 5.3 Optimal peak response.

there is a trade off between the time to settle, the open loop growth rate of the plant, and the maximum magnitude of the impulse response of the system.

Given a continuous time plant with a pole at p, the discrete time equivalent pole a depends primarily on the sampling frequency. Using Tustin's approximation on the plant $G(s)/(s-p)$ gives the discrete time model

$$G_d(z) \approx \left. \frac{G(s)}{(s-p)} \right|_{s=\frac{2}{\tau_s}\frac{z^{-1}-1}{z^{-1}+1}}$$

which has a pole at

$$a = \frac{2-p\tau_s}{2+p\tau_s}$$

The sampling period τ_s affects the magnitude of the pole a and therefore the peak impulse response performance for a given continuous time plant.

An impulse in continuous time ($\delta(t)$) is defined as a pulse of width τ and height $1/\tau$ so that the area of the impulse $(\int \delta(t)dt)$ is equal to unity. For a continuous time plant the discrete time results above can be used to show that, for a sampling period and impulse width τ_s, the optimal response is

$$\mu_c = \frac{1}{\tau_s} \frac{1-\frac{2-p\tau_s}{2+p\tau_s}}{\left(\frac{2-p\tau_s}{2+p\tau_s}\right)^m}$$

This simplifies to

$$\mu_c = \frac{2p}{(2+p\tau_s)\left(\frac{2-p\tau_s}{2+p\tau_s}\right)^m}$$

Allowing the sampling period to tend to zero gives

$$\lim_{\tau_s \to 0} \mu_c = p$$

The best performance that can be achieved with an infinite order controller with an infinite sampling frequency equals the continuous time instability growth rate and is independent of *m*.

Improving the impulse response is expected to improve the ELM response. The results from above allow the potential for improvement to be judged. The COMPASS–D P+D controller (using FL and IPR signals) has a predicted peak response of 0.227 to a unit pulse of width 50μs. The impulse response of the $\mathbf{H}_\infty$ controller designed in the previous chapter has a peak of 0.362 and so would be expected to require larger voltages in the presence of ELMs. The theoretical optimal performance is 0.189, which indicates that the P+D system performance is reasonably good in this respect. If we require the settling time of the impulse response to be limited to e.g. 1ms, then the restricted order optimal cost is 0.212 and the optimal controller order is 21.

Of course, it is not suggested that an actual peak optimal controller is used on COMPASS–D because it would not address the requirements for stability margin or 600Hz noise rejection. Nevertheless, the information provided is valuable as it sets the limits of performance of the system, against which controllers can be evaluated.

5.3 Multiobjective controller

Any practical controller needs a large stability margin and needs to reduce the 600Hz noise as provided by the $\mathbf{H}_\infty$ controller in the previous chapter. A multiobjective problem can be formed where the controller minimizing the peak of the impulse response is sought, subject to an $\mathbf{H}_\infty$ constraint. Both the $\mathbf{H}_\infty$ and the peak impulse response cost are closed loop convex. This means for example that the set of realizable, stable closed loop transfer functions with peak impulse response less than an arbitrary value μ, is convex. A convex set is defined as a set in which if any two

quantities R_1 and R_2 are elements of the set, then the quantity $R=\alpha R_1+(1-\alpha)R_2$ is also an element of the set for any α in the range $0<\alpha<1$.

The peak impulse response can be proved to be closed loop convex by considering two transfer functions R_1 and R_2 with impulse response sequences $\{r_i^1\}$ and $\{r_i^2\}$ respectively. If the transfer function R is defined as $R \triangleq \alpha R_1+(1-\alpha)R_2$ for any arbitrary value of α in the range $0<\alpha<1$, then the impulse response of R is $r_i=\alpha r_i^1+(1-\alpha)r_i^2$. If the sequences $\{r_i^1\}$ and $\{r_i^2\}$ satisfy the conditions

$$\begin{aligned} |r_i^1| &\leq \mu, \ \forall i \geq 0 \\ |r_i^2| &\leq \mu, \ \forall i \geq 0 \end{aligned}$$

then for r_i

$$\begin{aligned} |r_i| &= |\alpha r_i^1+(1-\alpha)r_i^2| \\ &\leq \alpha|r_i^1|+(1-\alpha)|r_i^2| \\ &\leq \alpha\mu+(1-\alpha)\mu \end{aligned}$$

The last inequality implies $|r_i| \leq \mu$ which therefore proves that the peak impulse response is a closed loop convex quantity. A similar result can be obtained to prove that the $\mathbf{H}_\infty$ norm of a transfer function matrix is also closed loop convex.

The convexity of the constraints imply that provided a suitable optimization method is used, convergence to the global optimal transfer function can be guaranteed. This result can conveniently be combined with *Q*–parameterization to search for the optimal peak impulse response whilst satisfying an $\mathbf{H}_\infty$ constraint. The objective function is defined as the peak of the impulse response, as in (5.1), of the transfer function $T(z^{-1})$

$$T(z^{-1})=N(z^{-1})X(z^{-1})+N(z^{-1})D(z^{-1})Q(z^{-1})$$

and the constraint is similar to (4.5)

$$\left\| \begin{matrix} \gamma W_1(z^{-1})T(z^{-1}) \\ W_2(z^{-1})K(z^{-1})S(z^{-1}) \\ W_3(z^{-1})S(z^{-1}) \end{matrix} \right\|_\infty \leq 1 \Leftrightarrow \left\| \begin{matrix} \gamma W_1(NX+NDQ) \\ W_2(DX+DDQ) \\ W_3(DY-DNQ) \end{matrix} \right\|_\infty \leq 1$$

The optimization problem can then be transformed from finding the optimal closed loop to finding the optimal Q. An initial solution for Q is to use $\mathbf{H}_\infty$ theory to find a controller ($K_{H\infty}$) satisfying the constraint. The controller has the realization

$$K_{H_\infty}(z^{-1}) = \frac{X_{H_\infty} + DQ_{H_\infty}}{Y_{H_\infty} - NQ_{H_\infty}}$$

where X_{H_∞} and $Y_{H_\infty} \in \mathbb{R}\mathbf{H}_\infty$ are coprime factors of the plant N/D and $Q_{H\infty}$ is the realization of Q for the controller. The set of Q over which the optimization is conducted can be expressed as

$$Q(z^{-1}) = Q_{H_\infty} + \frac{Q'}{N^- D^-}$$

The polynomials N^- and D^- contain the roots of N and D which lie strictly inside the unit disc. The polynomial Q' of order n_Q contains the optimization parameters (q_i)

$$Q'(z^{-1}) = \sum_{i=0}^{i=n_Q} q_i z^{-i}$$

The closed loop T is now

$$T' = NX_{H_\infty} + ND\left(Q_{H_\infty} + \frac{Q'}{N^- D^-}\right)$$
$$= T_{H_\infty} + N^+ D^+ Q'$$

Here $T_{H\infty}$ is the closed loop transfer function formed from the plant and $K_{H\infty}$ and N^+ and D^+ are the parts of plant numerator and denominator polynomials containing roots which lie on the unit circle or outside the unit disc. Similar expressions can be obtained for the $\mathbf{H}_\infty$ constraint.

The coefficients of Q' can be stacked in a vector $\boldsymbol{q} \in \mathbb{R}^{n_Q+1}$

$$\boldsymbol{q} = [q_0 \; q_1 \; \cdots \; q_{n_Q}]^T$$

and the optimization then expressed in terms of finding the optimal $\boldsymbol{q}$. The problem is still convex.

Suitable numerical algorithms exist for solving convex optimization problems. Kelly's cutting plane algorithm [Boyd91, Chapter 14] is used here to find peak impulse response controllers with $\mathbf{H}_\infty$ constraints (γ=0.12). Figure 5.4 shows upper and lower bounds on the peak impulse response (μ) which can be achieved for a given number of search parameters (n_Q). Increasing the number of search parameters improves the performance of the controller. The effect of Q optimization is clearly seen in the closed loop impulse responses of the unoptimized $\mathbf{H}_\infty$ controller and the optimized controller (Fig. 5.5). The responses are the same after 27 samples but the optimized controller flattens the initial overshoot.

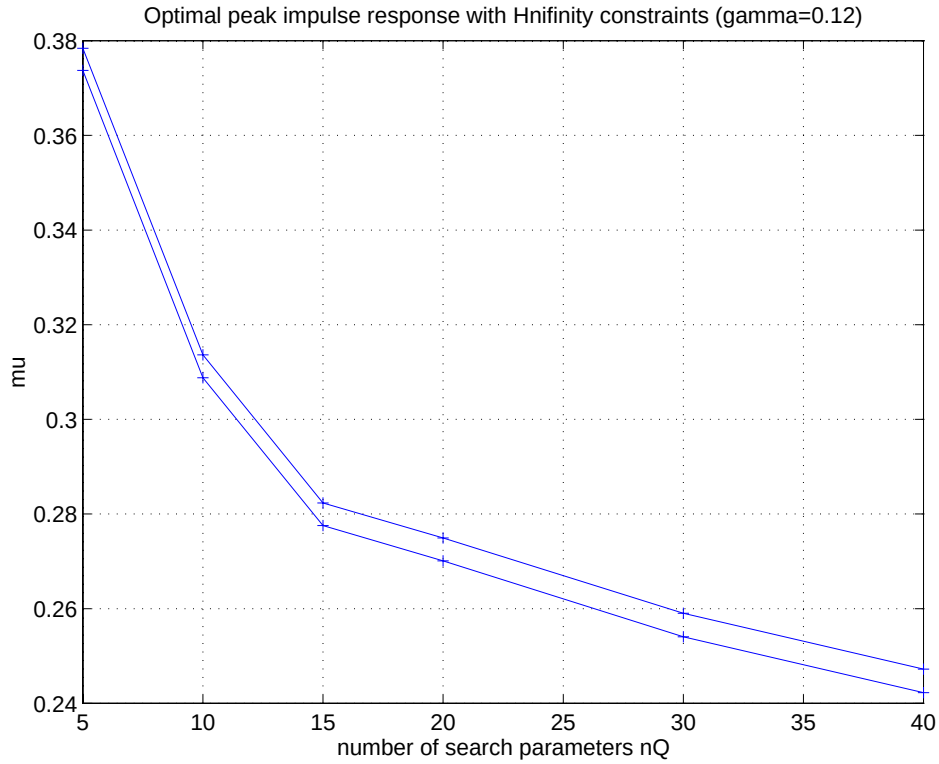


Figure 5.4 Optimal peak impulse response with $\mathbf{H}_\infty$ constraints.

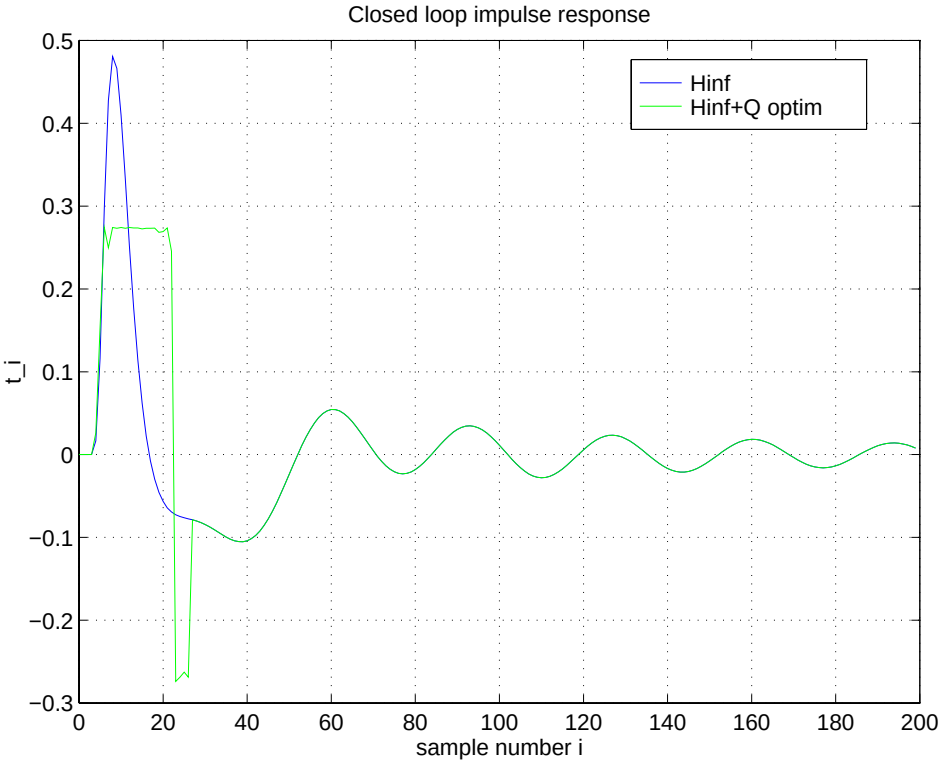


Figure 5.5 Impulse response of $\mathbf{H}_\infty$ controller (γ=0.12) and Q optimized controller (n_Q=20).

5.4 Discussion

Peak impulse response optimal controllers were examined. For plants with one unstable pole and no other unstable poles or zeros, the problem reduces to an analytical solution. The optimal controller is of infinite order but a suboptimal controller of finite order can also be determined. The performance improves as the order increases. The resulting controllers do not address the problems of noise and robust stability and therefore controllers were designed by combining peak impulse and $\mathbf{H}_\infty$ type constraints. A numerical optimization procedure was used to calculate these controllers and the procedure is guaranteed to converge to a global minimum because both the peak impulse and $\mathbf{H}_\infty$ type constraints are closed loop convex. The results show that increasing the number of search parameters can improve the peak impulse response.

The results of this chapter are useful for determining the limits of performance and hence provide a benchmark against which to compare other controllers. The optimal controllers are very high order and therefore impractical and this leads to the conclusions that other strategies aimed at minimizing the impact of large separated ELMs should be considered.

6 Conclusions

The main aims of this thesis have been to model and control the plasma vertical position in the COMPASS–D tokamak. The modelling has involved characterizing noise sources and disturbances and developing models of the plasma vertical position system from experimental data. The main sources of disturbances are 600Hz thyristor power supply noise and impulse–like responses from ELMs. Both sources of noise are also observed on the JET tokamak (presently the largest tokamak in the world) and ELMs are expected to be a feature observed on the proposed ITER (International Thermonuclear Experimental Reactor) tokamak. Their effect on the plasma vertical position in COMPASS–D is very small and is measured in terms of a few mm. However their effect on the power supplies is large and consequently it is important to minimize their effect on the power supply voltages and currents.

The plasma open loop response to actuator currents has been modelled directly from experimental data. System identification has been used to fit coefficients of mathematical models using the plasma input and output experimental data. The experiments were conducted in closed loop and a position reference signal switching at random between two levels was used to excite the plasma position modes. A simple low order model proved capable of adequately fitting the data. The resulting models show the effect of shielding on internal and external measurements of position. The frequency response of the external models have faster roll off and less phase lead than the internal models. The models are also strongly dependent on the shape of the plasma, with increasing instability growth rate with shaping field, and in the frequency domain higher bandwidths and lower phase leads. The effect of toroidal field (and therefore current density profile) is modest on COMPASS–D.

The models were used to predict gain margins and phase crossover frequencies for the system. The predictions were in close agreement with measured values demonstrating

the validity of the system identification approach to modelling the plasma position system. The use of system identified models combined with Nyquist diagrams was found to be an effective method of examining the stability of COMPASS–D, and would be a useful method of assessing stability on other tokamaks such as JET.

Acceptable stability margins are achieved with the P+D controller on COMPASS–D. This is in part due to the use of internal measurements of velocity which provide improved phase lead compared with external measurements. A difficulty faced by ITER is that harsh reactor conditions preclude the use of internal coils, reducing the stability margins. A problem which occurs on COMPASS–D and observed on JET is large 600Hz oscillations in the power supply signals. Placing a notch filter in the loop would introduce phase lag which would cause reduced stability margins. A P+D controller provides limited flexibility and would not be able to compensate for the loss of stability margin due to either using only external measurements or the introduction of a notch filter. However higher order controllers possess more degrees of freedom and allow the closed loop stability of the system to be improved. Two high order controllers were designed to stabilize the plasma position using only external measurements, whilst also attenuating the effect of 600Hz noise on the control amplifier signals. Both controllers were tested on COMPASS–D and proved to be successful, overcoming the limitations of a simple P+D controller and demonstrating the advantages of high order controllers in a real tokamak.

ELMs on COMPASS–D can cause large voltage swings in the control amplifier and large ELMs can lead to saturation of the amplifier and to loss of control. Large ELMs and subsequent loss of position control has also been observed on JET. Minimizing the peak of the impulse response could reduce the possibility of saturation. The problem of minimizing the peak of the impulse response can be solved analytically for COMPASS–D and it can be shown that the optimal performance worsens as the instability growth rate of the open loop plant increases. The optimal controller is not practical but a controller synthesis problem can be formulated to minimize the peak of the impulse response subject to 600Hz noise attenuation and robust stability constraints. This problem can be solved numerically and improvements to the peak performance can be made. The results are useful for providing the limits of performance in the presence of impulse disturbances but the resulting controllers are

impractical for use and future work would consider alternative control strategies to be tested during ELMy H–mode operation of a plasma shot.

The thesis has shown how the plasma position dynamics can be modelled using system identification and that the models can be used to analyze the stability properties of the control loop. The system identification approach has been used on COMPASS–D and is applicable to other tokamaks such as JET. Physical models are used to simulate the ITER control system but it is unclear how accurately the models reflect the true dynamics of the system. Future work would compare the frequency responses of physical models of an existing tokamak with system identified models. Validating the physical models in this way would improve the confidence that the ITER controller designs would work in practice.

The noise and disturbance sources are an important factor in determining the behaviour of the control loop. Different control signal behaviour is observed on COMPASS–D when the plasma operates in different modes such as ELM–free and ELMy H–modes. Future work would consider the physical causes of the behaviour on the vertical position system in terms of sensor noise and plant disturbances. This would allow ITER to be simulated with realistic noise and disturbances and also to allow more realistic controller specifications to be formulated.

High order controllers were tested on COMPASS–D and compared with simple P+D controllers were able to improve the stability and performance of the vertical position control loop. The design of the controllers made use of models of the plasma system and characterization of the disturbances. Modelling both the system dynamics and the disturbances would allow high order controllers to be designed to improve the performance of other tokamaks such as JET and ITER.

7 References

[Akaike74] A. Akaike, "A New Look at the Statistical Model Identification," *IEEE Trans. Automatic Control*, Vol. AC-19, No. 6, pp. 716–723, December 1974

[Al–Husari91] M. M. M. Al–Husari et al., "Vertical Stabilisation of Tokamak Plasmas," *Proc. 30th Conf. Decision and Control, Brighton, England, December 1991*, IEEE, pp. 1165–1170, 1991

[Amin88] R. Amin and J. Edmunds, "Confidence Limits on Identified Frequency Responses of Multivariable Systems," *International Journal of Control*, Vol. 48, No. 1, pp. 117-128, 1988

[Artemenkov72] L.I. Artemenkov et al., "Experiments on Equilibrium in the Uncased TO–1 Tokamak Device by Means of a Feedback System," *Nuclear Fusion Supplement, English Translations of the Russian Papers Presented at the 4th. Intl. Conf. on Plasma Physics and Controlled Nuclear Fusion Research, Madison, USA, 17–23 June 1971*, pp. 27–31, 1972

[Åström90] K.J. Åström and B. Wittenmark, *Computer Controlled Systems*, Prentice–Hall Inc., Englewood Cliffs, N.J., 2nd ed. 1990 (first published 1984)

[Booth86] J.A. Booth et al., "COMPASS Magnetic Field Coils and Structure Systems," *Fusion Technology 1986: Proc. 14th Symp. Fusion Technology, September 8–12, 1986, Avignon, France*, Pergamon Press, Oxford, Vol. 2, pp. 1781–1786, 1986

[Boyd91] S.P. Boyd and C.H. Barratt, *Linear Controller Design*, Prentice Hall, Englewood Cliffs, New Jersey, 1991

[Chiang92] R.Y. Chiang and M.G. Safonov, *Robust Control Toolbox Users Guide*, The Mathworks Inc., Cochituate Place, 24 Prime Park Way, Natick, Mass. 01760, August 1992

[Clarke87] D.W. Clarke, C. Mohtadi and P.S. Tuffs, "Generalized Predictive Control, Parts 1 and 2," *Automatica*, Vol. 23, pp. 137–160, 1987

[Clarke94] D. Clarke ed., *Advances in Model–Based Predictive Control*, Oxford University Press, Oxford, 1994

[Cloud86] D.J. Cloud and B. Kouvaritakis, "Statistical Bounds on Multivariable Frequency Response: An Extension of the Generalised Nyquist Criterion," *IEE Proceedings Part–D*, Vol. 133, No. 3, pp. 97–110, May 1986

[Dahleh88] M.A. Dahleh and J.B. Pearson, "Minimization of a Regulated Response to a Fixed Input," *IEEE Trans. Automatic Control*, Vol. 33, No. 10, pp. 924–930, October 1988

[Doyle92] J.C. Doyle, B.A. Francis and A.R. Tannenbaum, *Feedback Control Theory*, Macmillan, New York, 1992

[Freeman85] T.G. Freeman, "Selecting the Best Linear Transfer Function Model," *Automatica*, Vol. 21, No. 4, pp. 361–370, July 1995

[Gossner95] J.R. Gossner, B. Kouvaritakis and J.A. Rossiter, "Cautious Stable Predictive Control: A Guaranteed Stable Predictive Algorithm with Low Input Activity and Good Robustness," *Proc. 3rd IEEE Mediterranean Symp. on New Directions in Control and Automation, Limasol, Cyprus, 11–13 July, 1995*, Vol. 2, pp. 243–250, 1995

[Gran79] R. Gran, M. Rossi and M. Firestone, "A Survey of the TFTR Control Design," *Proc. 8th Symp. Engineering Problems of*

Fusion Research, Sheraton–Palace Hotel, San Francisco, California, November 13–16, 1979, Vol. IV, pp. 1854–1862, IEEE, New York, 1979

[Green95] M. Green, D.J.N. Limebeer, *Linear Robust Control*, Prentice Hall, Englewood Cliffs, New Jersey, 1995

[Hugill74] J. Hugill and A. Gibson, "Servo–Control of Plasma Position in Cleo–Tokamak," *Nuclear Fusion*, Vol. 14, No. 5, pp. 611–619, 1974

[Hayward89] R.J. Hayward et al., "COMPASS Machine Design and Construction," *Fusion Technology 1988: Proc. 15th Symp. Fusion Technology, Utrecht, The Netherlands, 19–23 September 1988*, Vol. 1, pp. 361–365, Elsevier, 1989

[Humphreys92] D.A. Humphreys and R. Yoshino, "JT–60 Upgrade Vertical Stability Experiments and Analysis," Report JAERI–M 92–069, Japan Atomic Energy Research Institute, Department of Fusion Plasma Research, Naka Fusion Research Establishment, Japan Atomic Energy Research Institute, Naka–machi, Naka–gun, Ibaraki–ken, May 1992

[Jardin82] S.C. Jardin and D.A. Larrabee, "Feedback Stabilization of Rigid Axisymmetric Modes in Tokamaks," *Nuclear Fusion*, Vol. 22, No. 8, pp. 1095–1098, 1982

[JET95] "JET Joint Undertaking: Progress Report 1994," Report EUR 16474-EN-C, JET Joint Undertaking, Abingdon, UK, April 1995

[Kessel90] C.E. Kessel, M.A. Firestone and R.W. Conn, "Linear Optimal Control of Tokamak Fusion Devices," *Fusion Technology*, Vol. 17, pp. 391–411, May 1990

[Knight92] P.J. Knight, M. Cox and T.C. Hender, "A Filament Code for Tokamak Axisymmetric Stability," *Computer Physics Communications*, pp. 99–109, 1992

[Knight95] P.J. Knight, "COMPASS–D SND Plasmas: Forces and Growth Rates," Internal Note QA Ref: F/MI/PJK/PACE/038, UKAEA Fusion, Culham, Abingdon, Oxfordshire OX14 3DB, UK, 25 September 1995

[Kouvaritakis92a] B. Kouvaritakis and J.A. Rossiter, "Use of Bicausal Weighting Sequences in Least Squares Identification of Open–loop Unstable Dynamic Systems," *IEE Proceedings Part–D*, Vol. 139, No. 3, pp. 328–336, May 1992

[Kouvaritakis92b] B. Kouvaritakis, J.A. Rossiter and A.O.T. Chang, "Stable Generalized Predictive Control: An Algorithm with Guaranteed Stability," *IEE Proceedings Part–D*, Vol. 139, No. 4, 1992

[Lazarus90] E.A. Lazarus, J.B. Lister and G.H. Neilson, "Control of the Vertical Instability in Tokamaks," *Nuclear Fusion*, Vol. 30, pp. 111–, 1990

[Lazarus91] E.A. Lazarus et al., "Higher Beta at Higher Elongation in the DIII–D Tokamak," *Physics of Fluids B*, Vol. 3, No. 8, pp. 2220–2229, August 1991

[Lingertat95] J. Lingertat et al., "The effect of ELMs on the Plasma Edge of JET," Report JET–P(95)31, JET Posters presented at the 22nd EPS Conference on Controlled Fusion and Plasma Physics (3–7 July 1995, Bournemouth, UK.) Volume 2, JET Joint Undertaking, Abingdon, Oxfordshire, OX14 3EA, UK., Poster No. R080, pp. 343–350, August 1995

[Lister90] J.B. Lister et al., "Experimental Sudy of the Vertical Stability of High Decay Index Plasmas in the DIII–D Tokamak," *Nuclear Fusion*, Vol. 30, No. 11, pp. 2349–2366, 1990

[Ljung87] L. Ljung, *System Identification*, PTR Prentice Hall, Englewood Cliffs, New Jersey, 1987

[Luenberger69] D.G. Luenberger, *Optimization by Vector Space Methods*, John Wiley & Sons, New York, 1969

[Mardia79] K.V. Mardia, J.T. Kent and J.M. Bibby, *Multivariate Analysis*, Academic Press, London, 1979

[Moore88] K.L. Moore and S.P. Bhattacharyya, "A Technique for Choosing Zero Locations for Minimal Overshoot," *IEEE Trans. Automatic Control*, Vol. 35, No. 5, pp. 577-580, May 1988

[Mori87] M. Mori et al., "Stability Limit of Feedback Control of Vertical Plasma Position in the JFT–2M Tokamak," *Nuclear Fusion*, Vol. 27, No. 5, pp. 725–734

[Moriyama85] S. Moriyama et al., "Analysis of Optimal Feedback Control of Vertical Plasma Position in a Tokamak System," *Japanese Journal of Applied Physics*, Vol. 24, No. 7, pp. 849–855, July 1985

[Morris95] A.W. Morris et al., "Disruptions, Vertical Instabilities and Halo Currents in COMPASS–D," *Proceedings of the 22nd European Physical Society Conf. on Controlled Fusion and Plasma Physics, Bournemouth, 3rd–7th July 1995*, Vol. 19C, Part III, pp. 49–52, 1995

[Nagayama84] Y. Nagayama et al., "Feedback Control of Vertical Plasma Position in Non–Circular Tokamak TNT–A," *Nuclear Fusion*, Vol. 24, No. 10, pp. 1243–1249, 1984

[Noll89] P. Noll et al., "Forces on the JET Vacuum Vessel During Disruptions and Consequent Operation Limits," *Fusion Technology*, Vol. 15, pp. 259–266, March 1989

[Ogata79] A. Ogata and H. Ninomiya, "Use of Modern Control Theory in Plasma Control at Neutral Beam Injection," *Proc. 8th Symp. Engineering Problems of Fusion Research, Sheraton–Palace Hotel, San Francisco, California, November 13–16, 1979*, Vol. IV, pp. 1879–1883, IEEE, New York, 1979

[Oppenheim89] A.V Oppenheim and R.W. Schafer, *Discrete–Time Signal Processing*, Prentice–Hall Inc., Englewood Cliffs, New Jersey, 1989

[Pomphrey89] N. Pomphrey, S.C. Jardin and D.J. Ward, "Feedback Stabilization of the Axisymmetric Instability of a Deformable Tokamak Plasma," *Nuclear Fusion*, Vol. 29, No. 3, pp. 465–473, 1989

[Portone94] A. Portone, "Modelling and Control of Tokamak Plasmas in Fusion Devices," PhD Thesis, University of London, Imperial College of Science Technology and Medicine, January 1994

[Ramo84] S. Ramo, J.R. Whinnery and T. Van Duzer, *Fields and Waves in Communication Electronics*, John Wiley & Sons, New York, 2nd ed. 1984 (first published 1965)

[Rossiter96] J.A. Rossiter, J.R. Gossner and B. Kouvaritakis, "Infinite Horizon Stable Predictive Control", to appear in *IEEE Trans. Automatic Control*, 1996

[Rubin93] N. Rubin, "Robust Identification of a Tokamak Model," copy of OHP transparancies presented at IEE Colloquium on Controller Design and Applications Using H–infinity, London, 27 October 1993, synopsis available in Digest No: 1993/194 from The Institution of Electrical Engineers, Savoy Place, London WC2R 0BL, UK, October 1993

[Söderström89] T. Söderström and P. Stoica, *System Identification*, Prentice Hall, New York, 1989

[Todd93] T.N. Todd and the COMPASS Team, "MHD Control and ECCD in Compass–D," *Plasma Physics and Controlled Fusion*, Vol. 35, Suppl. (12)B, pp. B231–B240, December 1993

[Tinios93] G. Tinios et al., "Model Reduction for Axisymmetric Tokamak Control," *Fusion Technology*, Vol. 24, pp. 355–365, December 1993

[Valovič91] M. Valovič, “Reply to the fax,” Internal Memorandum QA Ref: F/PD/RD/C/MagDiag/MV/93/5, UKAEA Fusion, Culham, Abingdon, Oxfordshire OX14 3DB, UK, 17 September 1991

[Valovič94] M. Valovič, “Measurement of Penetration Time for Radial Magnetic Field Through Vacuum Vessel on COMPASS–D,” Internal Memorandum QA Ref: F/PH/CMagDiag/MV(94)1, UKAEA Fusion, Culham, Abingdon, Oxfordshire OX14 3DB, UK, 17 March 1994

[Vyas95] P. Vyas, A.W. Morris and D. Mustafa, “Analysis of Experimental Performance and Robust Stability on the COMPASS–D Tokamak,” *Fusion Technology 1994: Proc. 18th Symp. Fusion Technology, August 22–26, 1994, Karlsruhe, Germany*, Elsevier Science B.V., Amsterdam, Vol. 1, pp. 703–706, 1995

[Ward92] D.J. Ward and S.C. Jardin, “Effects of the Plasma Deformability on the Feedback Stabilization of Axisymmetric Modes in Tokamak Plasmas,” *Nuclear Fusion*, Vol. 32, No. 6, pp. 973–994, 1992

[Ward93] D.J. Ward, A. Bondeson and F. Hofmann, “Pressure and Inductance Effects on the Vertical Stability of Shaped Tokamaks,” *Nuclear Fusion*, Vol. 33, No. 5, pp. 821–828, 1993

[Ward94] D.J. Ward, F. Hofmann, “Active Feedback Stabilization of Axisymmetric Modes in Highly Elongated Tokamak Plasmas,” *Nuclear Fusion*, Vol. 34, No. 3, pp. 401–415, 1994

[Wellstead91] P.E. Wellstead and M.B. Zarrop, *Self–Tuning Systems*, John Wiley & Sons, Chichester, 1991

[Wesson87] J. Wesson, *Tokamaks*, Clarendon Press, Oxford, 1987

[Wootton90] A.J. Wootton and L. Wang, “Tokamak Position Control,” *IEEE Trans. Plasma Science*, Vol. 18, No. 6, pp. 1008–1020, December 1990

[Yoshioka82] K. Yoshioka, M. Abe and T. Kobayashi, “Feedback Controller Synthesis for Tokamak Plasma Position Control,” *Japanese Journal of Applied Physics*, Vol. 21, No. 10, pp. 1501–1505, October 1982

[Zheng93] G.L. Zheng, P.E. Wellstead and M.L. Browne, “Self–Tuning Control Studies of the Plasma Vertical Position Problem,” *Fusion Technology*, Vol. 23, No. 4, pp. 369–383, July 1993